Smart Surfaces: Design, Structuring and Characterization

Master's Thesis in Nanoscience
by
Simen Hjellvik Askeland

Supervisors:

Prof. Dr. Bodil Holst

Dr. Naureen Akhtar

Department of Chemistry
University of Bergen

June 2016

Abstract

Nanotechnology has allowed scientists to look closer at what causes the many extraordinary phenomena we see in nature such as geckos walking on walls and the self-cleaning properties of the lotus flower. These phenomena are partially explained by the enhanced surface area obtained by structures at the micro- and nanoscale on the material surface. Smart surfaces are structured surfaces that by altering their surface area and chemical composition obtain new and widely applicable properties. In this work anti-fouling surfaces, i.e. surfaces that are not contaminated by oil while submerged in water, with possible future applications in low temperature environments, have been developed. As a substrate, sapphire was chosen as a particularly durable material, one of the hardest materials in the world. Before the nanostructuring work began, the properties of a set of commercially available, unstructured sapphire surfaces were characterized. These results were published in The Journal of Physical Chemistry C in 2015, co-authored by the author of this thesis. Inspired by the oil-repellent properties of fish in water, sapphire surfaces, which when unstructured show promising anti-fouling properties, were structured to enhance the tendency of trapping water in the surface features. The initial patterning was conducted using photolithography, allowing for fast and energy-efficient large-scale production. The structures were made in a size range 5-10 μm, with a spacing varying from $2 - 15$ μm inspired by previous results in the literature. Following the lithographic procedure, highly durable sapphire features were created by 1) the solid-state conversion of aluminium or 2) selective wet-etching of sapphire. The solid-state aluminium conversion was first reported in 2005, but to our knowledge this is the first time it has been applied to micron-scale structures. After the samples were produced, a systematic study of how the surface geometry influences the wetting properties of a material was conducted so that one in the future may choose the surface geometry suitable for the desired applications. These wetting properties were characterized using contact angle measurements.

After a thorough optimization procedure of the photolithographic procedure it was concluded that the in-house setup had some challenges regarding the contact between mask and sample making it difficult to create surface features < 5μm and that further optimization is required here. The systematic study of how the surface geometry influences the wetting properties revealed that a transition from the Cassie-Baxter wetting state, i.e. water droplets remaining on top of surface features, to the Wenzel wetting state, i.e. surface features completely wetted by the water droplet, happens when the spacing between 5 μm wide and 1.5 μm tall surface features is close to 10 μm.

Acknowledgments

I often claim to be a lucky man. Being supervised by the very talented Professor Dr. Bodil Holst and Dr. Naureen Akhtar once again confirms this. I am forever grateful for the opportunity to take part in this exciting project. I wish to thank Bodil for her continuous guidance, support and constructive feedback throughout the last couple of years, making me feel like a part of the Nanophysics "family" at the University of Bergen. I also wish to thank Naureen for her assistance during the experimental work, but also while writing, being available for questions and always encouraging me to keep on going. Their help has been invaluable for the work presented in this thesis.

I also wish to thank the other members of the Nanophysics group, with special thanks to Dr. Martin Møller Greve and Ranveig Flatabø, as they have always been available for questions regarding the laboratory equipment and experimental procedures. They have all made me feel more like a co-worker than a student.

Additionally I wish to thank Professor Dr. Petra Rudolf for allowing me to visit and borrow her lab facilities in the Zernike Institute for Advanced Materials at the Rijksuniversitet Groningen, Netherlands, and Ali Syari'ati for taking his time to show me how the AFM worked. I am also very grateful for the discussions on SU-8 and for the guidance in the nanolab at the Department of Biomedicine provided by Dr. Ivan Rios Mondragon.

A special thanks is due to the always positive Håkon Eidsvåg for the many discussions on topics relevant for the thesis and (most) that were not; both my writing endurance and concentration have been challenged thanks to him. I am also grateful for my friends Sverre, Oddbjørn and Gjermund Grødem reading through my thesis and always being available for a game of Dota 2. I am forever thankful to Ellen Birgitte Folgerø for her loving and supporting nature.

Contents

Abstract **iii**

Acknowledgments **v**

1 Introduction **1**
1.1 Motivation . . . 1
1.1.1 Economic Interests . . . 2
1.1.2 Environment . . . 2
1.1.3 Safety . . . 3
1.2 Status Quo . . . 3
1.2.1 Inspiration From Nature . . . 4
1.2.2 Requirements for Smart Surfaces . . . 5
1.3 Thesis Objectives . . . 6
1.4 Thesis Outline . . . 6

2 Theory **9**
2.1 Wetting . . . 9
2.1.1 Surface Tension and Contact Angle . . . 9
2.1.2 Wetting Models . . . 11
2.1.3 Contact Angle Hysteresis . . . 15
2.1.4 Oil in Water . . . 16
2.2 Relating Wetting and Icephobicity . . . 19

3 Equipment and Facilities **21**
3.1 The Nanostructures Laboratory . . . 21
3.1.1 Photolithography . . . 22
3.1.2 Electron-Beam Evaporator: Temescal FC-2000 . . . 24
3.1.3 Electron-Beam Lithography: Raith e-Line . . . 25
3.1.4 Reactive Ion-Etching: Plasmatherm 790+ . . . 26
3.1.5 Other Equipment . . . 29
3.2 Unit for Nano-Systems in Biomedicine . . . 31
3.2.1 Photolithography: MJB4 Süss MicroTec . . . 31
3.3 Zernike Institute in Groningen, Netherlands . . . 31

4 Sample Preparation **33**
4.1 Designing Surface Structures . . . 33
4.1.1 Mask layout . . . 33
4.1.2 Design Parameters . . . 35
4.2 Structuring Using Photolithography . . . 36

4.2.1 Samples . . . 36
4.2.2 Sample Cleaning . . . 37
4.2.3 Spin-Coating . . . 38
4.2.4 Tempering . . . 39
4.2.5 Exposure . . . 40
4.2.6 Development . . . 40
4.3 Solid-State Conversion of Al to Al_2O_3 . . . 41
4.4 Wells in Sapphire by Selective Etching . . . 41
4.5 Characterization . . . 42

5 Results and Discussion **45**
5.1 Unstructured Sapphire Windows . . . 45
5.2 Surface Structuring . . . 47
5.2.1 AR-P 3540 Optimization . . . 47
5.2.2 Sapphire Structuring . . . 55
5.2.3 SU-8 Optimization . . . 62
5.3 Contact Angle Measurements . . . 68
5.3.1 Structured Sapphire . . . 68
5.3.2 SU-8 Structures of Varying Geometry . . . 70

6 Conclusions and Future Work **75**

A Optimized Parameters for Microstructuring **77**
A.1 AR-P 3540 . . . 77
A.2 SU-8 2002 . . . 78

B Apparent Layering From Interference Effects **81**

List of Figures

2.1 Schematic of Liquid-Gas Interface . . . 10
2.2 Contact Angle Schematic - Smooth Surface . . . 11
2.3 Contact Angle Schematic - Rough Surface . . . 12
2.4 Contact Angle - Wenzel Model . . . 12
2.5 Contact Angle - Cassie-Baxter Model . . . 13
2.6 Two Models of Hydrophobicity . . . 14
2.7 Contact Angle - Hemi-Wicking . . . 15
2.8 Contact Angle Hysteresis . . . 16
2.9 Summary of Water and Oil Wetting . . . 18

3.1 Photolithography Setup . . . 24
3.2 Temescal FC-2000 . . . 25
3.3 Raith e-Line . . . 26
3.4 Plasmatherm 790+ . . . 28
3.5 Etching Profiles . . . 28
3.6 Contact Angle Setup . . . 30
3.7 Schematic of UiB NanoLab . . . 32

4.1 Mask Layout . . . 34
4.2 Mask Matrix Details . . . 35
4.3 Possible Problems During Spin-Coating . . . 39
4.4 Schematic of Sample Preparation Procedure . . . 43

5.1 Contact Angles for As-Received and RCA-Cleaned Sapphire Windows 46
5.2 AFM Images of RCA-Cleaned Sapphire Windows . . . 46
5.3 Fresnel Zone Plate . . . 48
5.4 Reference sample . . . 50
5.5 Changing Exposure and Developing Time . . . 51
5.6 New Resist, 25 µm Pitch . . . 54
5.7 New Resist, 15 µm Pitch . . . 55
5.8 New Resist, 7 µm Pitch . . . 55
5.9 Annealed Aluminium with Cavities . . . 57
5.10 Sapphire Pillar After Annealing . . . 59
5.11 Schematic Showing Sapphire Rim Structures . . . 59
5.12 First Test of Wet-Etched Sapphire . . . 61
5.13 Wet-Etched Sapphire . . . 61
5.14 SU-8: Overexposed . . . 63
5.15 SU-8: Structures with 25 µm Pitch . . . 65
5.16 SU-8: Structures with 15 µm Pitch . . . 66
5.17 SU-8: Structures with 7 µm Pitch . . . 67

5.18 Contact Angle Measurements: Structured Sapphire 69
5.19 Contact Angle Measurements: Squares 72
5.20 Contact Angle Measurements: Circles 73
5.21 Contact Angle Measurements: Hexagons 74

B.1 Edge Profile of Developed Sample 82

List of Tables

3.1 ISO 14644-1 Cleanroom Requirements 22

4.1 Mask Matrix Parameters 34
4.2 Sapphire (0001) Windows Used 37

5.1 Starting Parameters, AR-P 3540 47
5.2 Starting Parameters for First Successful AR-P 3540 48
5.3 Samples Used to Investigate Effect of Exposure and Developing Time 49
5.4 Contact Angle: Water in Air and Oil in Air for Structured Sapphire . 69
5.5 Contact Angle of Water in Air for Structured SU-8 71
5.6 Theoretical Contact Angle of Water in Air for Structured SU-8 Assuming Wenzel Wetting 71
5.7 Theoretical Contact Angle of Water in Air for Structured SU-8 Assuming Cassie-Baxter Wetting 72

Chapter 1

Introduction

The development of nanotechnology and -science has shown us that the bulk properties of a material can be drastically changed once its size is reduced to the micro-/nanoscale. Gold is for example known to be chemically inert, however nanoparticles of gold have been shown to be chemically active.[1] The seemingly uncommon properties of a material on the nanoscale can be attributed to quantum mechanical effects, but also to the increased relative surface area as compared to bulk. Controlling these new properties is what nanotechnology and -science aims to do. By doing so one can customize a materials properties to the desired applications, allowing for a "smart" material.

Smart surfaces are in this work regarded as a generic term for surfaces which by restructuring them will have their properties altered. They can for example be hydrophobic (water-repellent), icephobic (ice-repellent) or oleophobic (oil-repellent). By altering their design one could obtain surfaces that attract water (hydrophilic), are oleophilic, or even omniphobic, i.e. surfaces that display contact angles greater than 150° and low contact angle hysteresis (more on this in Section 2.1.3) with both polar and non-polar liquids.[2]

In this work the focus will be on underwater oleophobic surfaces, i.e. surfaces that repel oil when submerged in water, and structuring of optically transparent windows with future applications in harsh environments, i.e. $T < 5°C$. Such windows should therefore be icephobic.

1.1 Motivation

With their wide range of functionality smart surfaces also have a wide range of applications. The challenges arise as altering one property could influence the other properties of the surface. Should one manage to obtain a hydrophobic surface, this could render the surface oleophilic. It has been shown that making a surface superhydrophobic, i.e. contact angle $> 150°$ and contact angle hysteresis $< 10°$, requires surface structuring.[2] By doing so one increases the surface area of the substrate, allowing for a higher ice adhesion.[3] Being a relatively intricate process, what motivation is there to develop smart surfaces? Is there a need for ice-free surfaces, or surfaces that prevent oil from adhering under water?

1.1.1 Economic Interests

The lotus flower (Nelumbo nucifera) has been revered as a divine symbol for more than 5000 years. To Hindus and Buddhists the lotus flower symbolises beauty, purity and divinity.[4] This can be attributed to the lotus flowers ability to remain clean while growing from muddy waters. This ability to remain clean is caused by the superhydrophobic character obtained from hierarchical micro- and nanostructures on the petals. The water will immediately roll off the surface, bringing any contaminants with it.[5] Implementing such properties on surfaces, e.g. windows and walls, would allow for self-cleaning properties.

It is believed that approximately 30% of the worlds undiscovered gas and 13% of the world's undiscovered oil may be found in the Arctic.[6] This has resulted in a need for materials that can withstand such a harsh environment and hinder build-up of ice and oil on exposed structures and equipment. Otherwise there might be expensive stops in production, reduced equipment lifetime and reliability, eventually resulting in economic loss, or even worse; the loss of human life. This is particularly relevant in times where the oil price is low and companies need to save money where they can.

Any sensing technology used while submerged in water, e.g. for submarines and subsea drilling, should maintain its optical properties while requiring minimal maintenance. An anti-fouling sensor, i.e. a sensor that is not contaminated by for example organic material, would reduce the downtime of such a sensor, reducing the cost of using underwater sensors. Underwater sensors have the potential of replacing already existing expensive measurements such as seismic imaging.[7]

When developing renewable energy one might need anti-fouling sensors for future underwater energy harvesters such as wave farms. As for the renewable energy harvest on land, ice has been shown to be a challenge for renewable energy technology: Ice accretion on wind turbine blades decreases power production, and at harsh sites the annual power loss is usually in the range of 20-50 %. It can be detrimental to wind turbine performance, durability, and the safety of those in the vicinity of operating iced turbines.[8,9] For solar cells there exists no proper way of removing ice and snow on the surface which would reduce their efficiency.[10] Efficiency is already a problem for solar cells, the renewable energy source with the lowest fraction of optimal activity within one day (typically 0.16 for photovoltaic solar cells).[11]

The transmission of electrical power is also heavily influenced by ice and snow. In 2008 several winter storms affected large portions of southern and central China, whereas several transmission lines and power network towers deformed or collapsed due to excess amount of ice, causing a direct economic loss of about 25 billion USD (estimated using the exchange rate per October 2015).[12,13] Frost and ice accumulation has also been reported to decrease the efficiency of refrigerators and heat exchangers by about 50-75%.[14,15]

1.1.2 Environment

Anti-fouling paints are used to coat the hull of boats to prevent contaminants such as algae from attaching, resulting in higher drag and necessarily more fuel consumption and lower maximum speed. One of the most effective anti-fouling paints, developed in the 1960s, contains organotin tributylin (TBT), which has been shown to have a negative impact on sea life. Therefore the International Maritime Orga-

nization (IMO) adapted an Assembly resolution banning all harmful organotins in anti-fouling paints by 1 January 2008.[16] A hull should in other words be anti-fouling without posing a risk to the environment.

A material with hydrophobic and oleophobic characteristics could simplify the separation of oil and water in oil spills.[17] Hydrophilic membranes with superoleophobic properties would work well for this purpose, but not necessarily for sensor applications, as one would want the sensor to be waterproof.

Commercial smart surfaces could eliminate the negative environmental impact of chemicals doing the same job, e.g. self-cleaning windows could replace detergents previously used for cleaning the windows. The U.S. Geological Survey showed that one of the most frequent organic wastewater contaminants is 4-nonylphenol, a non-ionic detergent metabolite with relatively long degradation rate.[18] Nonylphenol is classified as an endocrine distrupter capable of interfering with the hormonal system of numerous organisms.[19]

Icephobic smart surfaces could also contribute positively to the environment. Nowadays airplanes some times have to go by the deicing station in order to prevent ice from forming on the wings during flight. This is done by a chemical method where organic liquids with crystallization temperatures much lower than that of water is sprayed on the body and wings of the airplane. Short duration and possible environmental problems make this method undesirable.[20]

1.1.3 Safety

Any hindering of a sensors operation pose a risk for whoever's safety depend on it. Should a gas sensor seize to operate it could as a worst case scenario result in loss of human life. Therefore it is important to prevent the optical window in a sensor from being contaminated. Currently this is done by heat, which reduces the sensor lifetime, or by manually wiping the surface clean.

In addition to being hazardous for whoever walks on it, ice, or the prevention of ice, might be dangerous for human beings in other ways.[21] Ice has been reported to be the cause of many aircraft accidents where lives have been lost, e.g. the American Eagle Flight 4184 which crashed on October 31, 1994 and all 64 passengers and 4 crew members were killed.[22–24] Attempting to remove ice on boats in cold/harsh environments should be an unnecessary risk to take for those on board. Moving on ice is exceptionally hard on a boat, possibly life-threatening for those on board.

1.2 Status Quo

There are already commercially available coatings or fabrics on the market, allowing for hydrophobic properties, such as sprays to make textiles and leather water repellent. The problem that these coatings have is that they must be reapplied within some time. Additionally, according to Lafuma and Quéré (2003), it is not possible to make a surface superhydrophobic by surface chemistry alone, i.e. coating the material.[25] This is because such flat hydrophobic surfaces exhibits contact angles in the range 100-120°, while the requirement for superhydrophobicity are contact angles $> 150°$, which is only obtained when air is trapped underneath the water droplet in a rough surface (more on hydrophobicity and contact angles in Chapter 2).

There are several strategies for removing ice on the surface. Electrothermal heating of the surface is the most obvious method, but this requires costly equipment and consumes energy. Additionally the radiation might interfere with other communication signals.[20] An alternative is to use shockwaves or manually scraping it away, but even though these methods are relatively cheap, they require more manpower and is less effective for large areas/stretches.[26] Timely removal of water prior to icing is also an alternative, which would involve making the surface hydrophobic. But if the water freezes too fast, one could use anti-icing coatings. The commercially available anti-icing coatings have been tested and show a broad range of ice adhesion strengths: 230-1400 kPa as compared to 1576 kPa of bare aluminium.[20] An ice adhesion of 55 ± 15 kPa can be blown off with a wind speed of 12 m/s, which according to Beauforts wind scale is a grade 6, corresponding to a strong breeze.[27] An improvement to the commercially available anti-icing coatings is therefore necessary for them to be classified as ice-repellent. Meuler et al. (2010) reported that no known material will be able to further reduce ice adhesion strengths, due to the relation between ice adhesion and wetting detailed in Section 2.2, meaning that surface structuring will be necessary.[28]

As mentioned above there exists commercially available anti-fouling coatings. These are impractical with regards to how often they must be reapplied and their durability. Possible solution would then have to be durable, but also cost-effective.

1.2.1 Inspiration From Nature

Most smart surfaces developed in research have some inspiration from nature. Through evolution nature has already optimized many processes to better survive harsh environments. With the many tools and equipments developed in the past 30 years scientists are now able to study nature in such detail that one can explain the many phenomena of interest.

Surfaces which show great hydrophobic character are referred to as superhydrophobic. These often mimic lotus leaves (Nelumbo nucifera) and water strider legs (Gerris remigis), and consist of hierarchical micro- and nanoscale structures with a lubricating layer.[5,29] When surfaces are superhydrophobic water will roll of by a slight tilt of the surface. Water droplets hitting superhydrophobic surfaces will retract completely and elastically. This is exploited in the wings of the Morpho butterfly (Morpho didius), and the leaves of the nasturtium plant (Tropaeolum majus L.), where by introducing some ridges in the surface one increases the retraction speed and thus make the water droplets go off faster.[30] The problem with superhydrophobic surfaces when considering anti-icing applications is the possibility for condensation inside these structures at low temperatures, allowing for pinning of the ice to the surface. The resulting ice adhesion is therefore ~ 4 times higher than that of the flat surface.[27]

The basidiomycete yeasts discharge their spores as they are enveloped in a liquid and merge with neighbouring liquid droplets. The released surface energy at coalescence provides kinetic energy and momentum for the drop and spore to "jump" away.[31] Knowing this, Zhang et al. (2013) designed surfaces that enhance coalescence between condensing water droplets, reducing the problem of increased ice adhesion for structured surfaces.[32]

Inspired by the Nepenthes pitcher plants, Aizenberg et al. (2011) developed a

slippery liquid-infused porous surface (SLIPS).[33] The difference from lotus-inspired structures is that this uses the nanostructures to lock in place the infused organic lubricating liquid. This prevents frost/ice from penetrating the structures and thus results in low ice adhesion. Though SLIPS have several interesting properties, their limitation was discovered by Rykaczewski et al. (2013) who noted that the lubricant was drained by capillary attraction and froze together with the water droplet.[34] Several freeze/thaw cycles would therefore gradually deplete the lubricant. Aizenberg et al. (2013) reported that this could be improved by changing the structuring of the sample.[20,35]

Alternatively one could use water as a lubricating liquid, instead of an organic liquid. As the hexagonal structure of ice breaks down at the ice surface (even at temperatures below 0°C), the formed liquidlike layer can act as a lubricant to ice being formed on top of the surface.[36] On this basis Chen et al. developed a surface which works as a sponge with a self-lubricating liquid water layer (SLWL) and obtained very low ice adhesion strengths ($\sim$ 60 kPa).[27]

Living systems in arctic environments such as fish and insects have anti-freeze proteins (AFPs) so that they can survive the low temperatures.[37] Esser-Kahn et al. (2010) attached these AFPs to polymer chains in order to cast them into thin films and thus slow down ice growth by 55 minutes.[37] This method shows potential to be further developed.

Fish scale is of interest when studying underwater oleophobicity, as fish are known to be well protected by contaminations from oil.[38] Jung and Bushan (2009) replicated shark skin, as a model for a low drag surface, with small individual tooth-like scales ribbed with longitudinal groves. The groves reduce water turbulence, and the water surrounding the structures play a role in protecting from algae and other marine organisms.[39] The water trapped in these small structures can repel the oil droplets, allowing for a high degree of oleophobicity.

1.2.2 Requirements for Smart Surfaces

What is required of a smart surface naturally depends on the planned application. Should the target be windows used in sensors, the surfaces must satisfy the required optical properties, in addition to the desired smart properties. The optical transparency is on the other hand not required for wind turbines and airplanes. In addition to the application-specific requirements, there are some aspects which are required for any surface to be practically applicable, some of which Jianyong Lv et al. (2014) also mentions:[20]

The surfaces must be stable and mechanically robust. This means that the performance is not influenced by external forces or processes such as several freeze/thaw cycles or abrasion. This is particularly challenging for micro- and nanostructures, but even more important. Should nanorods break off, one is left with high aspect-ratio nanopillars and nanotubes which is reported to pose health risks similar to asbestos.[40] The health risks and environmental effects associated with smart surfaces, both related to structures and coatings, are often neglected in this field of research.

Another requirement is the necessity of low-cost and large-scale fabrication in order for this to become commercially desirable. Few, if any, of the previously mentioned methods meet these criteria. Large-scale fabrication and low cost becomes

increasingly challenging as the complexity of the solution increases.

Smart surfaces should also be environmentally friendly. Any coatings or structuring should not be harmful in any way to those exposed during production, operation and termination.

1.3 Thesis Objectives

The objective of this project is to prepare a first set of model surfaces with the potential to be used for anti-fouling applications and which can be exploited for low temperature environments ($T < 5°C$). Bio-inspired strategies have been employed which involve structuring the surface using photolithography (PL). PL was used to create micron-scale surface structures. To obtain optically transparent and durable surfaces, sapphire substrates are used. Sapphire is one of the hardest materials in the world.

Lithography is a multistep process in which the surface is initially coated with a material sensitive to photons/electrons. This material, the photoresist, when exposed to photons/electrons through a mask, transfers the mask pattern to the surface. Undesired parts of the resist is then removed through chemical dissolution, which allows for structuring of the substrate surface through etching or metal deposition. For creating high resolution surface structures, each step needs to be optimized. This was particularly an issue for this thesis work, since this is the first time sapphire has been used as a substrate for the nano-/microstructuring at the UiB Nanostructures laboratory. Hence, the establishment of the preparation techniques in this laboratory can be seen as a thesis objective in itself. In particular, for the patterning a metal conversion method was introduced, which was first reported in the literature in 2005. To the best of our knowledge this is the first time this method has been used on the micron scale. Prepared samples have been characterized using scanning electron microscopy (SEM), atomic force microscopy (AFM) and contact angle measurements under controlled humidity and temperature conditions.

Evidently this thesis is of an experimental nature, with the focus being on which parameters influence the structuring of surfaces, and how to optimize them.

1.4 Thesis Outline

- Chapter 2 presents the theoretical background necessary to understand how water and oil behaves on a surface, and how this can be related to icing.
- Chapter 3 describes the facilities, equipment and chemicals used.
- Chapter 4 details the experimental procedure from designing mask to characterizing the results.
- Chapter 5 lists and discusses the results obtained through experiments.
- Chapter 6 summarizes the work conducted with regards to the results obtained and provides some recommendations and ideas for future work related to the topic.
- Appendix A details the recipe for optimized microstructuring.

- Appendix B details the explanation of an interference effect observed in the results.

Chapter 2

Theory

When designing smart surfaces for uses in anti-fouling and icephobic applications one first has to establish some knowledge on how a liquid behaves on a surface. Why are water droplets rolling off some surface, while other surfaces have the opposite properties, even for the same material? In the following chapter a presentation of wetting theory will be presented with concepts such as surface tension and contact angle. Additionally the relation between wetting and ice will be discussed.

2.1 Wetting

Wetting describes how a liquid is in contact with a solid surface, if it spreads across a large area relative to its volume, or if there is close to no contact at all. How liquids wet a surface depends on the forces acting between the liquid and solid, but also on the medium in which the liquid is situated, e.g. air. Wettability is often measured by evaluating the contact angle, θ.

2.1.1 Surface Tension and Contact Angle

Liquids are held together by long-ranged, attractive intermolecular forces, i.e. forces between molecules. These usually consist of dipole interactions, hydrogen bonds and the Van der Waals force, all of which are electrostatic interactions between a positive and a negative charge. In the absence of gravity the natural shape of a liquid droplet in air is a sphere. This is because a molecule submerged in the liquid will experience forces that are equal in all directions, while a molecule on the droplet surface has a net pull towards the center of the droplet, resulting in a spherical shape (see Figure 2.1), as this is the state with the lowest surface area.

A liquid's ability to withstand changes in its surface area is defined as the surface tension, γ. For liquids with strong intermolecular forces the surface tension is naturally higher, which explains why water with its strong hydrogen bonds have a higher surface tension compared to that of most other liquids. To increase the surface area work must be done. The surface tension is therefore defined as:[41]

$$\gamma = \lim_{\Delta A \to \infty} \frac{\Delta W}{\Delta A} = \frac{dW}{dA} \tag{2.1}$$

And it is measured in force per unit length, N/m, or energy per unit area, J/m^2. When using the latter unit one usually refers to surface tension as surface energy.

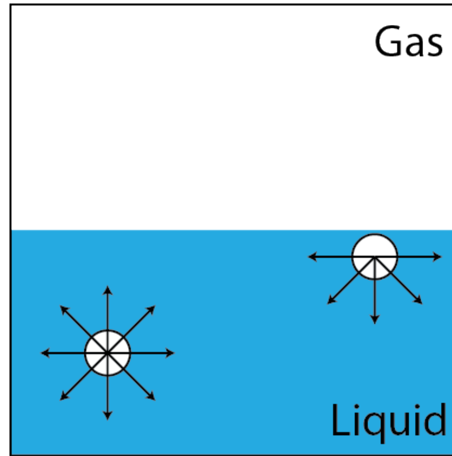

Figure 2.1: Schematic showing the forces on atoms/molecules of a liquid inside the bulk and at the surface. The surface atoms have a net force inwards.

Figure 2.2 shows how a liquid droplet wets a surface while surrounded by some gas, for example atmospheric air. There will be three competing forces limiting the number of atoms at the surface of each medium; one force which limits the area of contact between solid and liquid, $\mathbf{F}_{sl}$, one limiting the interface between solid and gas, $\mathbf{F}_{sg}$, and one between liquid and gas, $\mathbf{F}_{lg}$. Usually $\mathbf{F}_{sg} \ll \mathbf{F}_{sl}$.[41] Additionally there is the adhesive force, $\mathbf{F}_A$.

In order to move a droplet along the x-axis a distance dx, a work, dW, is required:

$$dW = \gamma dA = F dx \tag{2.2}$$

Moving the droplet along each of the three interfaces gives rise to the following equations:[42]

$$\begin{aligned} dW_{sl} &= \gamma_{sl}\, dA = \gamma_{sl} L dx = F_{sl} dx &(2.3a)\\ dW_{sg} &= \gamma_{sg}\, dA = \gamma_{sg} L dx = F_{sg} dx &(2.3b)\\ dW_{lg} &= \gamma_{lg}\, dA = \gamma_{lg} \cos\theta L dx = F_{lg} \cos\theta dx &(2.3c) \end{aligned}$$

Here $dA = Ldx$, with L being the circumference of the droplet which is considered constant for a small displacement, dx. As $\mathbf{F}_{sg}$ does work in the negative x-direction, it also has a negative contribution to the total work done, dW:

$$dW = dW_{sl} + dW_{sg} + dW_{lg} = \gamma_{sl} L dx - \gamma_{sg} L dx + \gamma_{lg} \cos\theta L dx \tag{2.4}$$

At equilibrium the droplet will not be moving, meaning that there will be no change in kinetic energy. From the work-energy principle ($W = \Delta E_k$) it is evident that $dW = 0$, which results in the following:

$$\cos\theta = \frac{\gamma_{sg} - \gamma_{sl}}{\gamma_{lg}} \tag{2.5}$$

This relation is commonly known as the Young equation. This equation assumes the contact line of the liquid partially wetting the smooth solid is a straight line and that the surface is chemically homogeneous.[43] If the liquid and gas medium is interchanged, i.e. there is a gas bubble in a liquid, then Equation (2.5) becomes

$$\cos\theta = \frac{\gamma_{sl} - \gamma_{sg}}{\gamma_{lg}} \tag{2.6}$$

which is the same as changing θ in Equation 2.5 with $180° - \theta$. In other words, the contact angle of a gas bubble in liquid will be $180° - \theta$ that of a liquid droplet in a gas.[44]

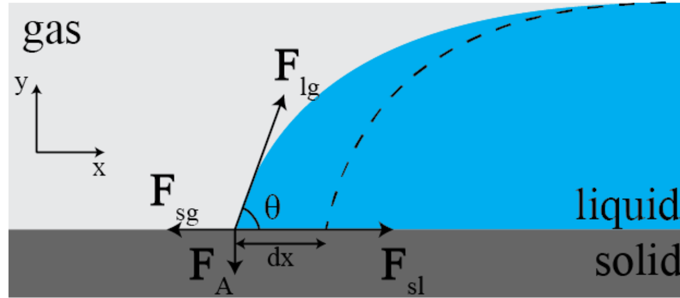

Figure 2.2: Schematic of a three-phase system consisting of a liquid, a gas and a solid which is displaced a distance, dx, along the x-axis. The point of intersection is called the three-phase point. The contact angle is indicated as θ. Redrawn from Helseth (2014).[42]

The wetting of a surface is measured by the contact angle. A liquid with contact angle below 90° is often termed a wetting liquid. With $\theta < 90°$ wetting is favorable, and the liquid spreads over a relatively large area of the surface. When $\theta = 0°$ one has obtained complete wetting, in which case the liquid will spread like a film on the surface. If the liquid is water, a wetting surface is often termed hydrophilic. For contact angles greater than 90° non-wetting liquids are obtained. Wetting is considered unfavorable, resulting in minimized contact between the liquid and the solid surface by forming a more spherical shape on the surface. When the liquid is water a non-wetting surface is considered hydrophobic. Hydrophobicity is the physical property of molecules to be seemingly repelled by water, though the reality is a lack of attraction, i.e. a reduction of the forces between the water and the surface. When $\theta > 150°$ and the contact angle hysteresis is less than 10° (more on this in Section 2.1.3) the surface is defined as superhydrophobic.

2.1.2 Wetting Models

In reality surfaces are not perfectly smooth, as is assumed in Equation (2.5), but instead they look more as shown in Figure 2.3. Again assuming equilibrium, Equation (2.4) is then rewritten as:[42]

$$dW = \gamma_{sl}Lds - \gamma_{sg}Lds + \gamma_{lg}\cos\theta^* Ldx = 0 \tag{2.7}$$

where θ^* is the apparent contact angle, i.e. the wetting angle of the projected smooth surface (which is what one would observe at the macroscopic scale). Equation (2.7) gives

$$\cos\theta^* = \frac{\gamma_{sg} - \gamma_{sl}}{\gamma_{lg}} \cdot \left(\frac{ds}{dx}\right) = \cos\theta \cdot \left(\frac{ds}{dx}\right) \tag{2.8}$$

From Figure 2.3 the following is obtained:

$$\frac{ds}{dx} = \frac{\sqrt{dx^2 + dy^2}}{dx} = \sqrt{1 + \left(\frac{dy}{dx}\right)^2} > 1 \tag{2.9}$$

As $ds/dx > 1$, it is evident, from Equation (2.8), that if $\theta < 90°$ then $\theta^* < \theta$. This means that a hydrophilic material will be more hydrophilic when the surface is rough as compared to smooth. Similarly when $\theta > 90°$ then $\theta^* > \theta$, meaning that a smooth hydrophobic surface will become more hydrophobic when it is rough.

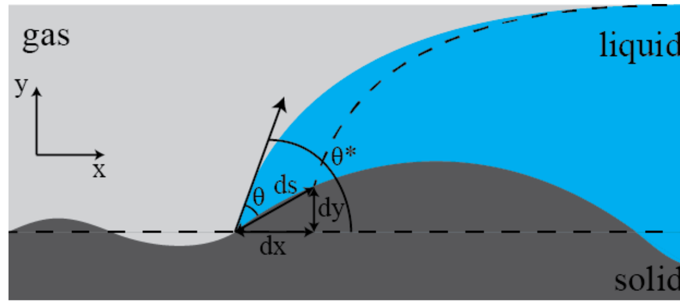

Figure 2.3: Schematic of a three-phase system consisting of a liquid, a gas and a solid which is contracted a distance, ds, along the solid surface. The contact angle between the surface and the water molecule in the three-phase point is indicated as θ, while θ^* is called the apparent contact angle. Redrawn from Helseth (2014).[42]

In literature ds/dx is referred to as the roughness factor, R_f.[39,44,45] The roughness factor is the fraction by which the real solid-liquid contact area is greater than the projected area, i.e. that of a smooth surface. Equation (2.8), most often with R_f instead of ds/dx, is known as the Wenzel equation.

The Wenzel model assumes, as indicated in Figure 2.4 that the droplet follows the topography in the solid-liquid interface. But this is not always the case, which is why an other model has been developed.

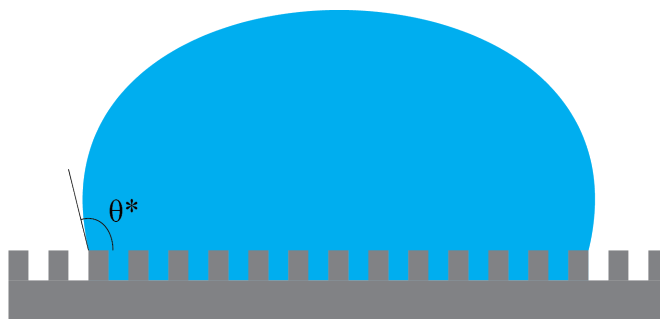

Figure 2.4: Schematic of a liquid droplet resting on a periodically rough surface with complete wetting of the solid-liquid interface, as assumed by the Wenzel model.

The Cassie-Baxter model describes the wettability of a surface composed of two different materials of proportions f_1 and f_2, where $f_2 = 1 - f_1$, and of Young contact angles θ_1 and θ_2. For a two-component system the apparent contact angle is found by:[46,47]

$$\cos\theta^* = f_1 \cos\theta_1 + f_2 \cos\theta_2 \tag{2.10}$$

For a chemically homogeneous surface, but with topographical features, there is a possibility of air being trapped in between these features and the droplet. A water droplet resting on top of these features would then experience the surface as a composite of solid and air. Then $\theta_1 = \theta$ and $\theta_2 = \pi$ ("contact angle" of water droplet in air). f_1 would then be the fraction of solid surface in contact with water, f_{sl}. And similarly f_2 is the fraction of air in contact with the water so that $f_{lg} = 1 - f_{sl}$. Equation (2.10) may then be rewritten to the following:

$$\cos\theta^* = f_{sl}\cos\theta - 1 + f_{sl} \tag{2.11}$$

Herminghaus (2000) argued that this equation should include some which takes into account the surface roughness, but this is primarily relevant for hierarchically structured surfaces, i.e. surfaces with more than one scale of roughness (typically a finer length scale texture on an underlying coarser length scale texture), which is not the case in this work. It will therefore not be included in the equation reported here.[48] A schematic of the Cassie-Baxter wetting state is given in Figure 2.5.

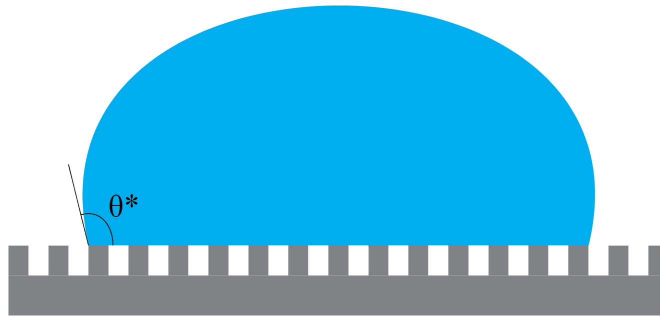

Figure 2.5: Schematic of a liquid droplet resting on a periodically rough surface with air pockets in the solid-liquid interface, as assumed in the Cassie-Baxter model.

Jung and Bushan (2009) gives an example of how both Equation (2.5) and Equation (2.11) can be used in practice:[39] A water droplet is placed on a surface with cylindrical pillars of diameter D, height H and pitch P. For the Wenzel state R_f will be larger than one, as there is extra contact area along the sides of the pillars. These sides have area πDH per P^2. For the Cassie-Baxter state f_{sl} is $\pi(D/2)^2$ per P^2. The following expressions for the apparent contact angles are obtained:

$$\text{Wenzel: } \cos\theta^* = \left(1 + \frac{\pi DH}{P^2}\right)\cos\theta \tag{2.12a}$$

$$\text{Cassie-Baxter: } \cos\theta^* = \frac{\pi D^2}{4P^2}(\cos\theta + 1) - 1 \tag{2.12b}$$

Both the Wenzel state and the Cassie-Baxter state are states of equilibrium, which means that they are both thermodynamically favorable. The Wenzel equation (Equation (2.8)) and the Cassie-Baxter equation (Equation (2.11)) should be satisfied as the contact angle, θ, increases, e.g. by changing the type of liquid on the surface. One should in other words, by equating the two, obtain some critical contact angle, θ_c, where there is a transition from the Cassie-Baxter to the Wenzel state.[25] This is the case when:

$$\cos\theta_c = \frac{(f_{sl} - 1)}{(R_f - f_{sl})} \tag{2.13}$$

This equation is valid for surfaces that are hydrophobic, i.e. $\theta > 90°$, since $\cos\theta_c < 0$ ($R_f > 1$ and $f_{sl} < 1$). In the hydrophilic state, i.e. $\theta < 90°$, the solid-liquid contact is favoured over the solid-gas ($\gamma_{sl} < \gamma_{sg}$), meaning that the solid-liquid interface is likely to follow the roughness of the surface, resulting in the Wenzel wetting state.[49] From Equation (2.13) it follows that surfaces with $\cos\theta_c < \cos\theta < 0$ are in the Wenzel state, while surfaces with $-1 < \cos\theta < \theta_c$ are in the Cassie-Baxter state. This is illustrated in Figure 2.6. As there is an energy barrier between the two wetting states one may also obtain a metastable Cassie-Baxter state, indicated by the dotted line in the figure.[25] Moving over this energy barrier could be done by an external perturbation, e.g. by pushing the drop, but only from the Cassie-Baxter state to the Wenzel state.[25,47] Forcing a water droplet from the Wenzel state to the Cassie-Baxter state has not been reported yet.

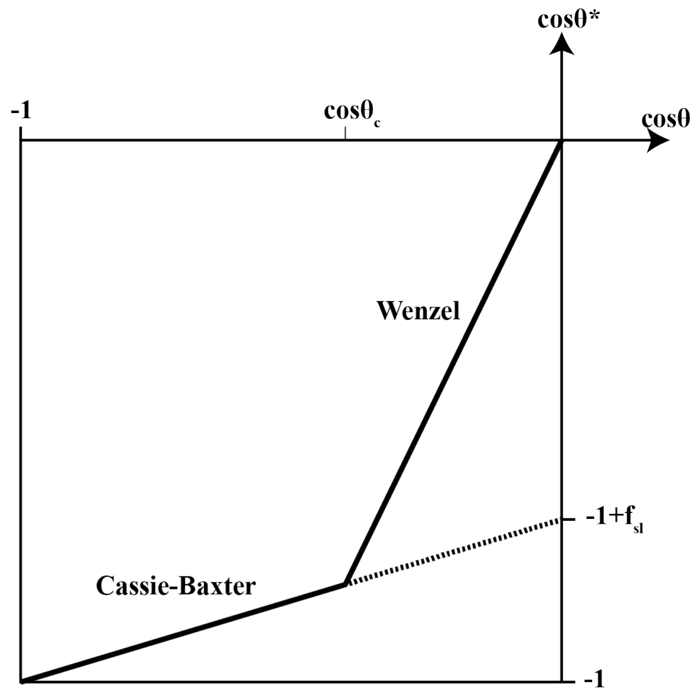

Figure 2.6: Plot indicating how surface features dominate whether a water droplet is in the Wenzel or the Cassie-Baxter wetting state. The dotted line represents the metastable Cassie-Baxter state. Redrawn from Lafuma and Quéré (2003).[25]

Similar to the Cassie-Baxter and Wenzel transition for hydrophobic surfaces, there is a transition for hydrophilic surfaces. From Equation (2.8) we know that $R_f > 1$, while $-1 \leq \cos\theta \geq 1$. This means that at some critical contact angle, θ_h, the Wenzel equation is no longer valid (due to $\cos\theta^* > 1$). At this situation one obtains what is called hemi-wicking (see Figure 2.7), with some of the liquid propagating into the texture of the solid, without wetting the top of the textures.[49] Bico et al. (2002) show that this transition happens when[49]

$$\cos\theta_h = \frac{1 - f_{sl}}{R_f - f_{sl}} \tag{2.14}$$

As $R_f > 1$ and $f_{sl} < 1$ it is clear that the equation always defines hemi-wicking between 0° and 90°. Hemi-wicking is similar to the Cassie-Baxter wetting state, but with the gas pockets being replaced by liquid pockets. The apparent contact angle, θ^*, of a water droplet in the hemi-wicking state can therefore be found by assuming $f_1 = f_{sl}$, $f_2 = 1 - f_1 = 1 - f_{sl}$, $\theta_1 = \theta$, as for the CB-state, and $\theta_2 = 0$ ("contact angle" of water droplet in water) in Equation (2.10):

$$\cos\theta^* = f_{sl}\cos\theta + 1 - f_{sl} \tag{2.15}$$

Figure 2.7: Schematic of a liquid droplet resting on a periodically rough surface with some of its volume propagating into the texture of the solid, a phenomenon called hemi-wicking.

2.1.3 Contact Angle Hysteresis

For most practical investigations of contact angle it is not possible to directly investigate whether the structure is in the Wenzel or Cassie-Baxter state. But as a result of their properties, i.e. the Cassie-Baxter wetting a lower solid surface area than the Wenzel state, there are considerable differences in the adhesion of the two states. As a consequence, a droplet might have a hydrophobic contact angle ($\theta^* > 90°$), but still have a relatively high adhesion to the surface. This adhesion is often measured as contact angle hysteresis. Contact angle hysteresis is measured as the difference between the advancing and the receding contact angle, θ_a and θ_r respectively:

$$H = \theta_a - \theta_r \tag{2.16}$$

The advancing contact angle is the maximum apparent contact angle for a droplet with increasing volume while its solid-liquid interfacial contact area remains constant (see Figure 2.8). As an opposite the receding contact angle is the same as the advancing, but with the volume being decreased. The contact angle hysteresis is in most cases greater than zero, as one even for a molecularly smooth surface will have a difference between θ_a and θ_r.[44] The apparent contact angle, θ^*, is found somewhere between θ_a and θ_r. In literature the contact angle hysteresis is often considered as the difference between the maximum contact angle, θ_{max}, and the minimum contact angle, θ_{min}, of a droplet rolling or sliding down a tilted surface. But as Krasovitski and Marmur (2004) points out, θ_{max} and θ_{min} do not in general simultaneously equal θ_a and θ_r, respectively.[50]

The advancing and receding contact angles are often termed dynamic contact angles, as they appear for a droplet of varying volume. The apparent contact angle, θ^* and θ are on the other hand static contact angles, as the droplet is in equilibrium

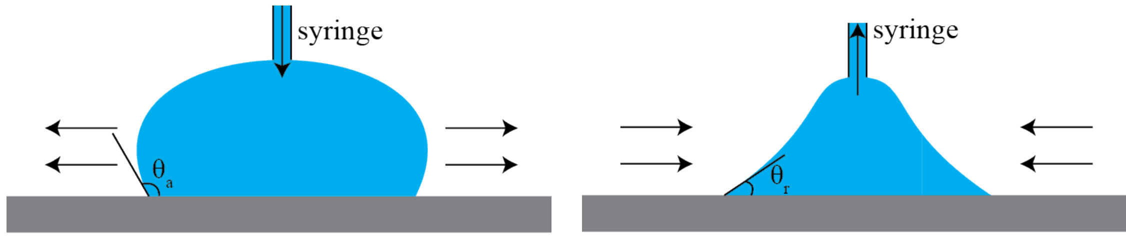

(a) Schematic of droplet with constant increasing volume while the solid-liquid interfacial area remains constant. The resulting apparent contact angle, θ_a, is called the advancing contact angle.

(b) Schematic of droplet with constant decreasing volume while the solid-liquid interfacial area remains constant. The resulting apparent contact angle, θ_r, is called the receding contact angle.

Figure 2.8: Schematic showing the difference between advancing and receding contact angle, θ_a and θ_r respectively.

with a constant volume. One could argue that these are not necessarily static problems, as one always have some degree of evaporation or other external influences.[51] It is in other words difficult to avoid dynamic effects, and it could be of relevance to include all parameters when reporting contact angles, such as time after the droplet is placed on the surface, volume of the droplet, humidity and temperature.

2.1.4 Oil in Water

The results given in Section 2.1.2 with regards to wetting of a liquid is naturally valid for other liquids than water. When studying the anti-fouling properties of a surface it could be necessary to understand how oil in air wets the surface and how this, together with the water in air wetting properties, may be related to the wetting of oil as the substrate is submerged in water.

Jung and Bushan (2009) related the wetting of water and oil in air to oil's wetting in water by combining the Young's equation for the three substances, as given in Equation (2.17):[39]

$$\cos\theta_W = \frac{\gamma_{SA} - \gamma_{SW}}{\gamma_{WA}} \tag{2.17a}$$

$$\cos\theta_O = \frac{\gamma_{SA} - \gamma_{SO}}{\gamma_{OA}} \tag{2.17b}$$

$$\cos\theta_{OW} = \frac{\gamma_{SW} - \gamma_{SO}}{\gamma_{OW}} \tag{2.17c}$$

The subscripts represent water, oil, solid and air. By solving Equation (2.17a) for γ_{SW} and Equation (2.17b) for γ_{SO}, they may be inserted into Equation (2.17c) and give the following:

$$\cos\theta_{OW} = \frac{\gamma_{OA}\cos\theta_O - \gamma_{WA}\cos\theta_W}{\gamma_{OW}} \tag{2.18}$$

But as was the case for Equation (2.5), the above equations do not include surface roughness. When using the apparent contact angle, θ^* instead of θ, Equation (2.17a), (2.17b) and Equation (2.18) will be:

$$\cos\theta_W^* = R_f\cos\theta_W = R_f\frac{\gamma_{SA}-\gamma_{SW}}{\gamma_{WA}} \tag{2.19a}$$

$$\cos\theta_O^* = R_f\cos\theta_O = R_f\frac{\gamma_{SA}-\gamma_{SO}}{\gamma_{OA}} \tag{2.19b}$$

$$\cos\theta_{OW}^* = = R_f\cos\theta_{OW} = \frac{\gamma_{OA}\cos\theta_O^* - \gamma_{WA}\cos\theta_W^*}{\gamma_{OW}} \tag{2.19c}$$

where the roughness-dependence of Equation (2.19c) is incorporated in θ_O^* and θ_W^*. Equation (2.19) will be valid for an oil droplet completely wetting the solid surface, i.e. a droplet in the Wenzel state. It is very similar to that which Jung and Bushan suggested, with the only difference being that one is working with apparent contact angles instead of the Young contact angles, i.e. those of smooth surfaces.

A summary of how the above equations can be interpreted by the wetting properties of a solid surface is given in Figure 2.9. For a surface which is hydrophobic in air, i.e. $\theta_W^* > 90°$, and oleophilic in air, i.e. $\theta_O^* < 90°$, the surface will be oleophilic in water. This originates from $\theta_W^* > 90°$ making $\cos\theta_W^* < 0$ and $\theta_O^* < 90°$ making $\cos\theta_O^* > 0$. As a result $\gamma_{OA}\cos\theta_O^* - \gamma_{WA}\cos\theta_W^* > 0$, and thus $\cos\theta_{OW}^* > 0$. Also, to obtain an underwater olephobic surface, one has two options; Either make sure that $\gamma_{OA}\cos\theta_O^* < \gamma_{WA}\cos\theta_W^*$ for a surface being hydrophilic in air ($\gamma_{SA} > \gamma_{SW}$), or make sure that $\gamma_{SA} < \gamma_{SW}$, $\gamma_{SA} < \gamma_{SO}$ for a surface that is both hydrophobic and oleophobic in air.

For oil droplets wetting a surface submerged in water, one may consider the Cassie-Baxter wetting of the oil droplet in water, i.e. when the structures are trapping water instead of air. Using Equation (2.10), and assuming $f_1 = f_{sl}$, i.e. the fraction surface of solid surface in contact with oil, $\theta_1 = \theta_{OW}$, i.e. the contact angle of water in water for a flat surface, $f_2 = 1 - f_1 = 1 - f_{sl}$, and $\theta_2 = \pi$ (the "contact angle" of oil droplet in water), we get:

$$\cos\theta_{OW}^* = f_{sl}\cos\theta_{OW} - 1 + f_{sl} \tag{2.20}$$

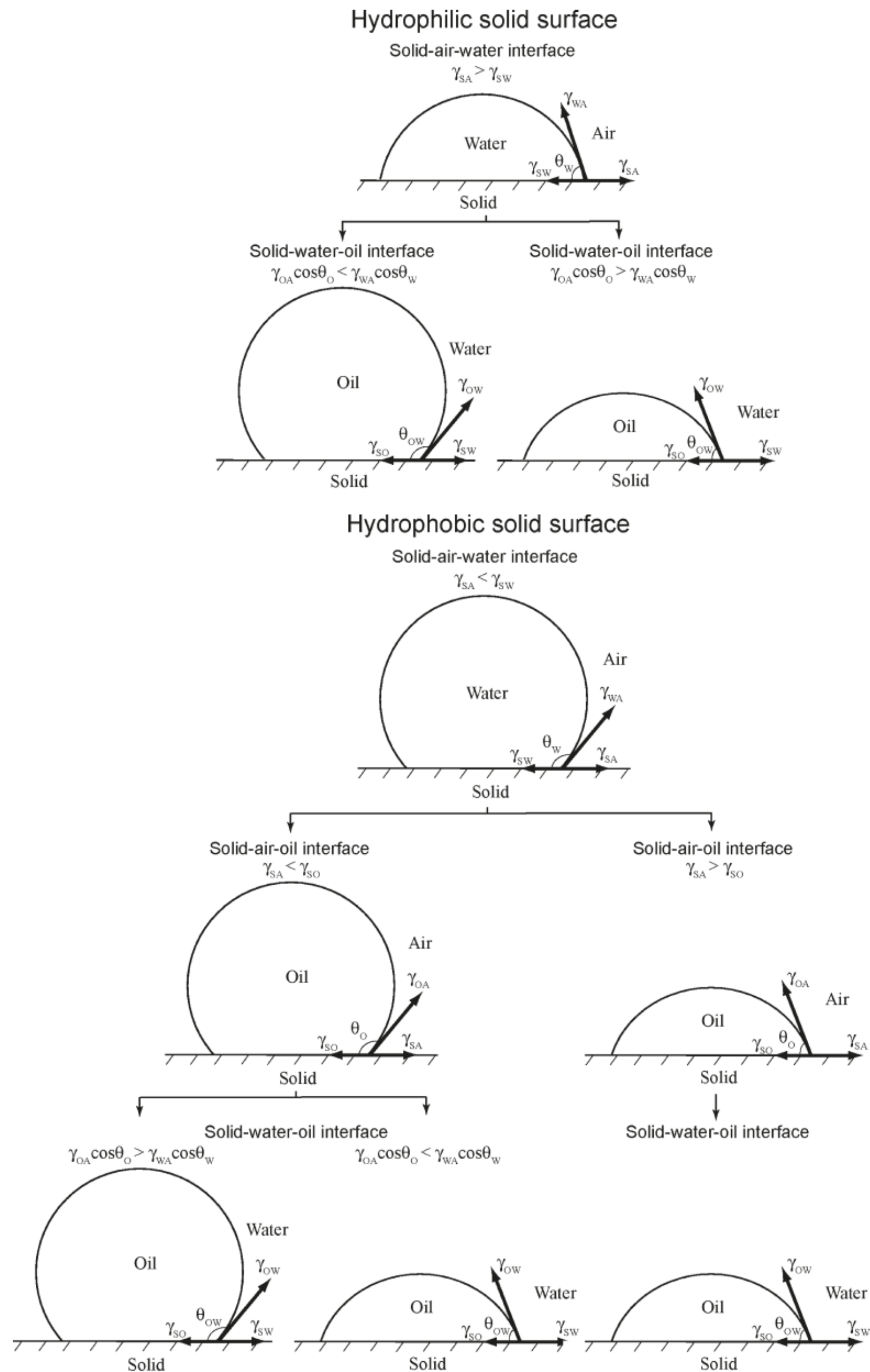

Figure 2.9: Schematic relating the water and oil wetting properties in air of a surface to the oil in water wetting properties. Figure from Jung and Bushan (2009).[39]

2.2 Relating Wetting and Icephobicity

Should the surfaces created be used in harsh environments, one should know how the wetting properties of the surface relates to the ice adhesion. As was mentioned in the introduction, making a surface hydrophobic does not mean that it will be icephobic. Hydrophobic surfaces could naturally reduce the contact time of a water droplet, making it fall off before it freezes. But at temperatures below the dew point water might condensate in between the structures, and not necessarily attach on top of the structures, preventing the Cassie-Baxter wetting. If the surface area fraction of the solid surface is equal to, or smaller than 0.068, a superhydrophobic surface may keep its properties below dew point.[20] For freezing water droplets in the Wenzel state, the surface area will be greater than that of a flat surface, allowing for a higher ice adhesion than for a flat surface.[3]

Lv et al. (2014) suggest that one should develop a unified definition for this ice adhesion, and come up with the following suggestion:

$$\text{Adhesion strength} = \frac{F}{A} \tag{2.21}$$

where F is the shear force for detaching the ice from a solid surface, and A is the apparent contact area (cross sectional area) between the ice and the substrate.[20] In 2010 Meuler et al. showed that there is a linear relation between the average shear strength of ice adhesion, τ_{ice}, and the interaction parameter $[1 + \cos\theta_r]$, where θ_r is the receding contact angle, given as:[28]

$$\tau_{ice} = (340 \pm 40 \text{ kPa})(1 + \cos\theta_r) \tag{2.22}$$

This can again be related to the work of adhesion, W_{adh}, defined as:[28,53,54]

$$W_{adh} = \gamma_{lg}(1 + \cos\theta_r) \tag{2.23}$$

By Equation (2.22) one can conclude that by obtaining a highest possible receding contact angle one will obtain a low ice adhesion. It has to be noted that this validity was proven for smooth surfaces with various coatings. But what Meuler et al. points out is that no known smooth material has receding contact angles much higher than what they obtained. Further reductions in ice adhesions is therefore believed to require surface structuring on the micro- and nanoscale.[28]

Chapter 3

Equipment and Facilities

This chapter describes the equipment and facilities used in the thesis to structure and characterize smart surfaces. The work is primarily conducted in the Nanostructures Laboratory at the Department of Physics and Technology and the Unit for Nanosystems in Biomedicine located at the Department of Biomedicine, both departments being part of the University of Bergen.

The samples are usually produced using photolithographic techniques combined with chemical etching or electron beam metal evaporation followed by thermal oxidation, and investigated using an optical- or electron microscope. Wetting properties are characterized using a contact angle setup, with structural parameters found using an atomic force microscope.

3.1 The Nanostructures Laboratory

The University of Bergen (UiB) built it's Nanostructures Laboratory (NanoLab) in 2011 with funding from Trond Mohn and the Research Council of Norway. The lab is located at the Department of Physics and Technology (IFT, from the Norwegian abbreviation).

The lab is equipped with modern thin-film processing and lithography equipment. Using the electron-beam lithography tool (Raith e-Line) one may pattern resist thin-films with structures in the order of 10 nanometers. The patterns may then be transferred to other thin-films using the electron-beam evaporator (Temescal FC-2000) or a spin-coater. Transferring is done using the reactive ion-etcher (Plasmatherm 790+) or the wet bench, where one may perform wet-etch or lift-off processes. There is also an UV-exposure setup available for crude patterning.[55] A sketch of the lab is shown in Figure 3.7 at the end of this chapter.

The lab has several rooms of various cleanliness depending on their use. The two most important rooms are the ISO-5 and the ISO-7 rooms. These rooms are classified by ISO 14644-1 standard developed by the International Organization for Standardization (ISO) (See Table 3.1).[56] The other rooms in the lab are either semi-clean- or non-cleanrooms. The e-Line is located in the ISO-7 together with a mini sputter coater. In the ISO-5 one finds the Plasmatherm 790+, a wet bench, the UV-exposure setup in addition to a hot plate, an oven and a thin-film analyser. The Temescal is located in a semi-clean room between the ISO-5 and the ISO-7 (see Figure 3.7). All samples are transported between the cleanrooms in custom sample holders which keep them clean.

Table 3.1: Cleanroom requirements by the ISO 14644-1 standard.[56] ISO 9 corresponds to room air.

ISO Class	Maximum particles/m^3					
	$\geq$ 0.1 µm	$\geq$ 0.2 µm	$\geq$ 0.3 µm	$\geq$ 0.5 µm	$\geq$ 1 µm	$\geq$ 5 µm
ISO 1	10	2				
ISO 2	100	24	10	4		
ISO 3	1 000	237	102	35	8	
ISO 4	10 000	2 370	1 020	352	83	
ISO 5	100 000	23 700	10 200	3 520	832	29
ISO 6	1 000 000	237 000	102 000	35 200	8 320	293
ISO 7				352 000	83 200	2 930
ISO 8				3 520 000	832 000	29 300
ISO 9				35 200 000	8 320 000	293 000

3.1.1 Photolithography

Most of the experimental work conducted in this thesis revolves around the use of photolithography. Photolithography (PL) is a process where a material, the resist, is selectively exposed to light, most often in the range of ultraviolet or visible light. When exposed, the resist will change its chemical or physical properties, so that it will be soluble or insoluble in a solution, the developer. For a positive resist the developer will be soluble in the developer when exposed to light, and for a negative resist it will become insoluble. In order to structure surfaces this resist is homogenously deposited on a sample/substrate, often referred to as a wafer.

As one can expose large areas at the same time using light, PL allows for large scale and fast production of structures. This, in addition to being easy to use and cheap, is why it is the main method used for structuring surfaces in this thesis.

Photolithography is in other words a technique of great use for surface structuring. It is therefore a necessity in a nanolab such as the one located at IFT, UiB. This is why a simple setup was made in-house by Thomas Reisinger and Rachid Maad. It consists of a container, a sample holder and a lid mounted with LEDs (Figure 3.1). This setup is a contact lithography setup, which means that the mask is in direct contact with the sample.

In order to create both pillars and wells, i.e. ”inverted” pillars, both a positive and a negative photoresist have been used with the same mask. These resists are the positive photoresist AR-P 3540 produced by AllResist GmbH, and the negative photoresist SU-8 2002 produced by MicroChem Corp. They are both delivered as liquids, and therefore have to be spin-coated onto the substrate in order to achieve homogenous deposition. Details on the sample preparation procedure is given in Chapter 4.

AR-P 3540

AR-P 3540 has optimum working conditions when exposed to light of the following wavelengths; 365 nm, 405 nm or 436 nm.[57] Therefore our setup has diodes that emit light at wavelengths of 405 nm ± 2.5 nm. Positive resists, such as AR-P 3540, are made from a combination of film forming agents, e.g. cresol novolac resins, and

light-sensitive components, e.g. diazonaphthoquinone (DNQ), dissolved in solvents such as methoxypropyl acetate. The DNQ works as an inhibitor for the dissolution of the polymer resin. When exposed to light, the DNQ will undergo a reaction where it is converted into a ketene. The ketene will react with water to form an alkali soluble indene carboxylic acid.[58] Seeing that the developer used, AR 300-35 is an aqueous solution of pH-value 13, the area of the AR-P photoresist which has been exposed to light will be dissolved when immersed in AR 300-35. To stop the reaction the sample is rinsed with, or immersed in, deionized water.

SU-8 2002

SU-8 is a photoresist first developed by IBM and has grown to become a popular photoresist for photolithography and is now additionally available for electron-beam lithography.[59,60] The main components of the SU-8 are Bisphenol A Novolak epoxy oligomer (EPON® SU-8 resin, Shell Chemical) and up to 10 wt% triarylsulfonium hexafluoroantimonate salt (CYRACURE® UVI, Union Carbide) photoacid generator. The SU-8 2002 resist is dissolved in cyclopentanone which has good coating and adhesion properties.[59] Upon exposure, protonated oxonium ions are generated as the photoacid generator decomposes to form hexafluoroantimonic acid that protonates the epoxides on the oligomer. These protonated oxonium ions reacts with neutral epoxides in a series of cross-linking reactions upon heating.[59] The Novolak epoxy monomers contains eight highly reactive epoxides which allows for a high degree of cross-linkage as the polymer is heated. This cross-linkage is what gives the resist its negative type characteristics upon exposure. The unexposed resist is dissolved when the substrate is immersed in, or rinsed with, propyleneglycol monomethylether acetate (PGMEA). This reaction is stopped using isopropanol.[60]

As SU-8 is most commonly exposed with conventional UV (350-400 nm) radiation and 365 nm is the recommended wavelength, the setup available in-house is not compatible as it consist of LEDs which emit light at wavelengths 405 nm $\pm$ 2.5 nm.[61] There is a nanolab located at the Department of Biomedicine, UiB, where they have a mask aligner, MJB4 from Süss MicroTec AG, which has a wavelength range of 350-450 nanometers, making it compatible with SU-8. This instrument was used for the SU-8 work presented here. The sample preparation will be detailed in Chapter 4. The nanolab at the Department of Biomedicine is not in a cleanroom environment, which is crucial for micro- and nanostructuring, but there were no other options available.

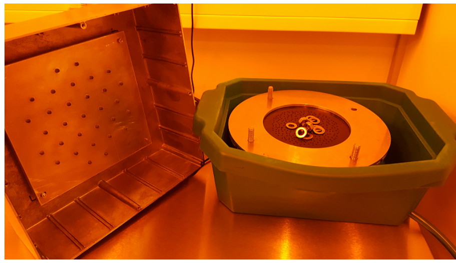

(a) Photo of photolithography setup built in-house at the UiB NanoLab.

(b) Schematic of photolithography setup built in-house at the UiB NanoLab. Exposed resist is indicated with an orange color. Redrawn from Bolstad (2012).[62]

Figure 3.1: Picture and schematic of the setup built in-house at the UiB NanoLab for photolithography. The orange tint of the photo is due to the short wavelengths being filtered out of the ISO-5 lighting as they might interact with the photoresists stored there.

3.1.2 Electron-Beam Evaporator: Temescal FC-2000

One of the most important instruments in the UiB NanoLab is the electron-beam evaporator: Temescal FC-2000 (see Figure 3.2). It is produced by the Temescal Division of Ferrotec. The Temescal FC-2000 (from now on referred to as "Temescal") is used for the deposition of metal and oxide thin films. At the time of writing the following six materials are available for deposition: gold (Au), aluminium (Al), nickel (Ni), silicon dioxide (SiO_2), chromium (Cr), and zinc oxide (ZnO). These materials are evaporated when an electron-beam is focused on one of the source materials located in a crucible, while the other five are covered. The crucible is placed in a vacuum system to reduce the electron-beam's and the material vapor's interactions with other particles. For efficient loading and unloading of samples a load-locked system is used, i.e. the samples are loaded via a chamber of smaller volume (referred to as the upper chamber) separated from the main chamber, for efficient pumping and ventilation.

The deposition evaporation process consists of first loading the sample into the upper chamber. For this project the substrate is usually loaded horizontally to avoid deposition on the structures' side walls, but there are options for loading the sample with an angle. After the chamber is closed it is most common to select and edit a recipe. The recipes are highly customizable with options such as choosing sample rotation speed, deposition rate and final thickness, but consist of three primary steps: *pump down*, *deposition*, *vent*.[63] One may add several *deposition* steps for multi-layer evaporation before venting.

The *pump down* step consists of three "sub-steps": *start-up*, where all interlock conditions (improperly sealed valves etc.) are checked, *rough pump down*, where the rough pump quickly lowers the pressure to approximately $8 \cdot 10^{-2}$ Torr, and *final pump down*, where the cryopump generates a pressure of approximately $3 \cdot 10^{-6}$ Torr.

The *deposition* step consists of four sub-steps: *ready for deposition*, where the deposition parameters are downloaded from the Temescal Control System (TCS) to the deposition controller. *Rise and soak*, where the electron beam power supply is increased gradually in two steps for a stable heating of the target source. When the target source is warm enough a shutter opens, allowing for evaporation throughout the chamber in the step called *deposition*. The deposition thickness is monitored by a crystal oscillating at 6 MHz frequency which experience a frequency shift correlated

to the deposition rate. The deposition rate varies with the power of the electron beam, and the thickness will be calculated using the deposition time and rate. The final sub-step of the *deposition* is the *ramp down*, where the voltage is ramped down steadily to 0 volts.

After *deposition* one has to *vent* the system. The isolation valve between the evaporation chamber and the cryopump is then closed, followed by the valve separating the upper chamber from the main chamber.[63] A vent valve is opened for the upper chamber which lets through nitrogen (N_2) gas. Once atmospheric pressure is obtained, one is able to manually open the door and remove the samples. After the sample has been removed it is common practice to pump the system to vacuum unless further processing is planned in the near future.

Figure 3.2: Picture of the Temescal FC-2000 situated in the semi-clean room at the UiB Nanostructures Laboratory. Picture from Bolstad (2012).[62]

3.1.3 Electron-Beam Lithography: Raith e-Line

UiB's NanoLab is built around the electron-beam (e-beam) lithography tool (Figure 3.3). Together with the mini sputter coater it is the only instrument located in the ISO-7 room. The temperature in this room is controlled and stabilized to prevent drift of the electron beam while patterning. The most commonly used resist is Poly(methyl methacrylate) (PMMA), a positive resist, removable by a chemical developer (AR 600-56) when exposed to electrons.

The e-Line is in practice an electron microscope with the possibility of generating a pre-determined beam path, which in turn can be used to pattern resists sensitive to electrons. This means that it is fully functional as a scanning electron microscope (SEM) as well. For this thesis the e-Line has primarily been used as a SEM for high resolution imaging. And as for every SEM, it consists of a beam column, which generates and focuses the electron-beam. The column voltage can be varied between 100 V and 30 kV. The electron beam is generated from a thermal field emission filament; a strong electric field is applied to a heated metal. The extracted electrons are then focused by a set of electrostatic lenses as they control the beam

path through a cylindrical vacuum chamber (column). There are primarily two ways of moving across a sample using this setup, either using deflecting coils which move the electron-beam, or by a laser interferometer controller which controls the sample stage movement. The coils can deflect the beam within an area of 100 µm x 100 µm, known as a writefield, which means that investigating or writing on the sample at larger distances requires stage movement. One may choose between six apertures when chosing the beam width, ranging from 7.5 µm to 120 µm.

The electrons hitting the sample will either be reflected or interact with the sample and generate secondary electrons. In the e-Line only secondary electrons are detected, either by the located close to the incoming electron beam usually referred to as an in-lens detector, or the secondary electron detector (SE2) located at an angle relative to the sample. In order to reduce interactions between the electrons and gas molecules the system is pumped to ultra-high vacuum. Therefore the system has a load-lock system, as for the Temescal, to allow for efficient loading and unloading of samples.

The e-Line is controlled using a personal computer situated outside the ISO-7. The software on this computer, "e-Line", allow for design of patterns used for lithography in addition to importing certain file formats and thus allowing for more advanced patterns. The computer is also used to control the vacuums and monitor the e-beam stability.

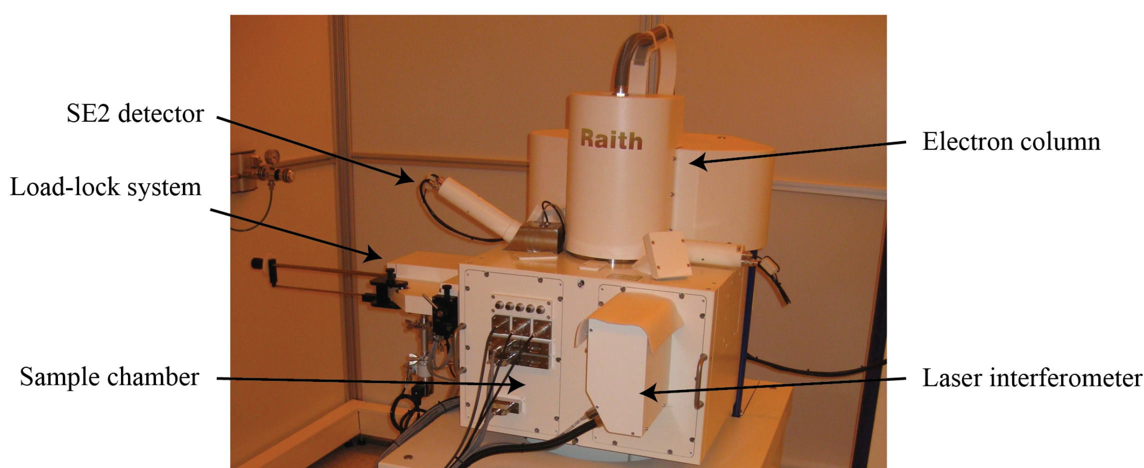

Figure 3.3: The UiB NanoLab Raith e-Line which functions as an electron microscope and a electron-beam lithography system. Samples are loaded via a loadlock for quick and easy loading and un-loading.

3.1.4 Reactive Ion-Etching: Plasmatherm 790+

For nano- and micro-fabrication etching is an important technique when structuring surfaces that are not sensitive to lithographic techniques. There are two types of etching; wet-etch and dry-etch. Both techniques require a mask which is not sensitive to the etchant, i.e. material used for etching, which leaves the rest of the substrate un-etched. Wet-etching uses a liquid-phase etchant, in which the substrate is submerged, that dissolves the target material. Dry-etching sends reactive ions (plasma) onto the substrate which removes the target material.

Wet-etching does not require any other instrument than what is needed to perform it in a safe matter, and is therefore an easily available technique. Dry-etching on the other hand requires instruments which generate plasma in vacuum chambers and can therefore be a costly procedure, but will in many cases produce more desirable results. The Plasmatherm 790+ reactive ion-etcher (RIE) is placed in the ISO-5 cleanroom of the UiB NanoLab (see Figure 3.4) and is used to selectively etch organic, metal, semi-conductor or oxide thin-films. Its main purpose is to transfer resist patterns into other materials using reactive ions, and it is in other words a dry-etching instrument. The available gases are CF_4, CHF_3, argon, helium and oxygen.

The instrument consist of a sample holder placed in a vacuum chamber which after loading sample is filled with the desired gas through a control valve. The plasma is produced by applying a strong electromagnetic field at radio frequencies which ionizes the gas. The electromagnetic field will cause the free electrons to move towards the surface which in turn generates a negative charge at the sample holder. This negative charge will exert a coloumbic force on the positive ions (plasma), drawing them towards the sample in a vertical direction. The target material is then removed either by chemical reactions with the plasma or by sputtering, i.e. momentum exchange between the energetic plasma and the atoms in the material ejecting them from the surface. The by-product from the chemical reactions are usually volatile gases which are removable by pumping the system, unlike wet-etching where the dangerous by-product can be harder to remove.[64]

RIE optimization should not be underestimated with regards to complexity. The most influential parameters affecting the etching results are: gas composition, gas flow rate, RF power, chamber pressure and substrate temperature. Other parameters are sample holder material, geometry of sample chamber, frequency of electromagnetic field, chamber wall material and pumping speed.[65]

There are two parameters which are relevant to the chosen type of etching, anisotropy/isotropy and selectivity. Anisotropy and isotropy are classifications of etching profile. An isotropic etching has the same etching rate in all directions, and is common in wet-etching, while anisotropic is the opposite, i.e. etching in only one direction. As the ions of RIE hit the sample vertically an anisotropic etching profile is obtained (Figure 3.5). The anisotropic wet-etching profile is what one obtains when etching a crystalline material and the etching rate is dependent on crystal orientation. Selectivity is the ratio of target material etching rate to mask material etching rate. If the mask is reactive to the plasma it is desirable that it is etched as slow as possible, while the target material is etching as fast as possible, allowing for a high selectivity.

Figure 3.4: Plasmatherm 790+ located in the ISO-5 cleanroom at the UiB Nanostructuers Laboratory.

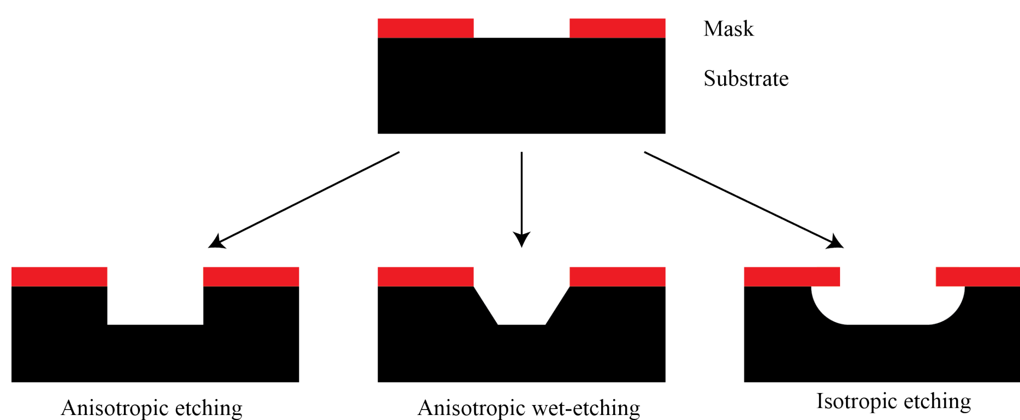

Figure 3.5: Etching a masked substrate usually has three etching profiles; anisotropic dry-etch, anisotropic wet-etch or isotropic wet-etch. Redrawn from M. M. Greve (2013).[65]

3.1.5 Other Equipment

The above mentioned equipment is important for the lab, but most of it is by all practical measures useless without some extra equipment; the hotplate and spin-coater being the most crucial.

Spin-Coating: Chemat KW-4A Spin Coater

Spin-coating is a method widely used in nano- and microtechnology and consist of depositing a liquid homogeneously on a substrate. This is done by rotating the substrate, forcing the liquid to spread by centripetal acceleration. Given sufficient spinning speed and time, excess liquid will go off the substrate when reaching the edge. The deposited film thickness is dependent on several parameters, with spin speed, viscosity and concentration of solution and solvent being the most influential. Other parameters are dispense volume, acceleration, air flow and evaporation rate.[66]

At the UiB NanoLab a Chemat Technology Inc. KW-4A Precision Spin Coater is used when applying layers of resist onto wafers used for electron-beam lithography or photolithography. It has a two-stage spinning, with the first going from 500-2500 RPM at 2-18 seconds, while the other is from 800-8000 RPM at 3-60 seconds. It is connected to a vacuum pump that generates a pressure difference between the bottom of the substrate and surrounding air, holding it in place. The spin stability is $\pm 1\%$ and coating uniformity is given to be 3%.[67]

Hotplate: UniTemp GmbH HP-155

After depositing the resist on the substrate, one has to evaporate the solvent, and in some cases improve the resist-substrate adhesion. This is usually done on a hotplate as this is both fast and convenient. The temperature of the hotplate as well as tempering time (amount of time the substrate is located on the hotplate) depends on deposition thickness, the substrate thermal conductivity and type of resist.[59] The hotplate is also used when post-exposure bake is needed to further enhance the chemical processes that happens in the photoresist during exposure.

At the UiB NanoLab an UniTemp GmbH HP-155 is placed in the ISO-5 clean-room next to the PL-setup and in close proximity to the spin-coater. When tempering resists which release dangerous fumes upon evaporation, it can easily be placed inside the fume hood.

Contact Angle Measurement: Dataphysics OCA 20L

Just across the hall from the UiB NanoLab another lab is located. It is a regular physics laboratory containing an AFM and a X-ray diffraction setup for educational purposes, in addition to what is used in this thesis; the Dataphysics OCA 20L used for contact angle measurements. The OCA 20L consist of a camera, a single-direct dosing system with various syringes, a sample stage and an illuminator (Figure 3.6). The samples can be placed directly on top of the sample stage and water droplets deposited on top (sessile drop method), or using the captive bubble method. The captive bubble method is used for samples where the density of the droplet medium is lower than that of the surrounding medium. The sample is then attached facing down into the immersion medium, and the droplet is deposited from a u-shaped syringe, allowing it to flow up to the sample and stay there. The setup for captive

bubble method is shown in Figure 3.6. The droplet volume and deposition rate is controlled by the single-direct dosing system. A software on the computer, SCA20, record and store image sequences and does video based measurements of the static and dynamic contact angle on various surfaces.

The system is also compatible with a tilt-table, allowing for measurements on roll-off angles. A setup for cooling samples in order to measure freeze time and how a droplet's properties change with temperature has also been built, but not used in this work.

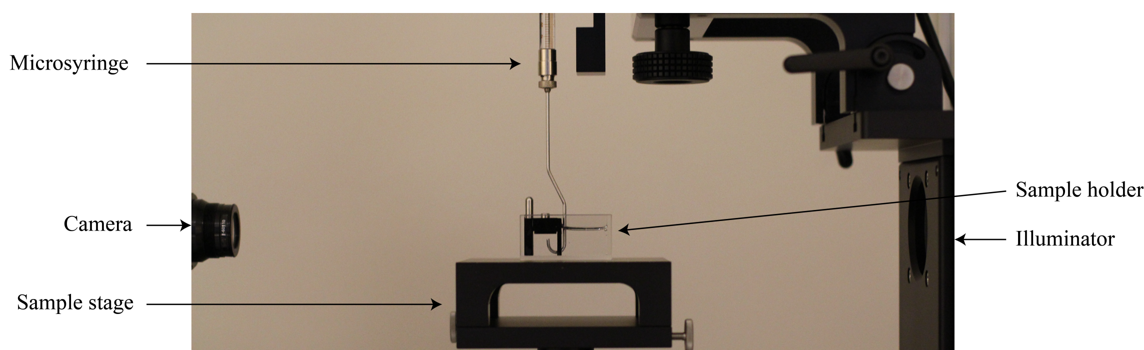

Figure 3.6: Image of the components in the contact angle setup. The camera and the syringe dosing system is connected to the computer next to this setup, allowing for accurate dosing and imaging of droplets on surfaces. The shown setup is for oil-in-water measurements. Here the sample has to be held with the surface facing down, as the oil droplets will float to the water surface when submerged in water.

Thin Film Analyzer: Filmetrics F10-RT

Situated next to the RIE in the ISO-5 one will find the thin film analyzer Filmetrics F10-RT. The machine measures the thickness of thin films by analyzing the reflected and transmitted spectra from a white light source. In this work the F10-RT is used to measure the thickness of the spin-coated resist layers. As the user implements the material properties and some approximate thickness, the machine will use curve fitting to estimate the thickness of the resist. It can also be used to estimate the thickness of other coatings deposited on the material, such as the Si_3N_4-layer on the silicon samples used.

Optical Microscope: Nikon Eclipse LV100ND

After exposing and developing the samples an optical microscope is used to determine if the parameters are close to optimal, before further investigations are conducted in for example an electron microscope. In the semi-clean room of the UiB NanoLab a Nikon Eclipse LV100ND is located for just this purpose. The LV100ND is a manual compact microscope with a mounted camera on top, which together with a control unit allow for digital imaging of the sample. It can image using either episcopic (reflected) or diascopic (transmitted) illumination, and is compatible for brightfield, darkfield, DIC, fluorescence, phase contrast and simple polarizing imaging.

3.2 Unit for Nano-Systems in Biomedicine

The unit for nano-systems in biomedicine, UnB, is located in the Building for Basic Biological Research (BBB) at the Department of Biomedicine. It is part of the Cellular Networks Group, and the Nanoscience Programme at the University of Bergen, and provides the technical support and expertise for the development of micro- and nano-featured systems, as a tool to study biological subjects and human diseases.

Nano-patterned samples, micro-systems or combinations of them can be custom designed and fabricated to address specific scientific questions such as cell-cell communication, cell-matrix communication and cell response to mechanical deformation. All these questions are key questions in tissue engineering and in understanding of human diseases. A focus is on understanding how different cell types can read nanostructures and integrate signals there from.[68] One may use photolithography to mimic cell positioning and confinement. PL is also of relevance when conducting tissue engineering research. An essential piece of the UnB is therefore the manual mask aligner "MJB4" produced by Süss MicroTec, a photolithography system that aligns the sample with mask to ensure uniform exposure.

There are two hotplates at the UnB, both of which are used for the post-exposure bake of the SU-8 lithography procedure, named Präzitherm and produced by Harry Gestigkeit GmbH.

UnB is not a cleanroom, yet it has been used for some of the work reported in this thesis. This is, as was detailed in Section 3.1.1, because there is no setup available at the NanoLab located at the Department of Physics and Technology for SU-8 exposure.

3.2.1 Photolithography: MJB4 Süss MicroTec

MJB4 is an inexpensive photolithography solution equipped with reliable, high precision alignment and printing capability in the submicron range. It offers four different printing modes; soft-, hard-, vacuum- and soft vacuum contact mode, whereas hard contact has been used for this thesis. In this mode the wafer is brought in direct contact with the mask, while a positive nitrogen pressure is used to press the substrate against the mask.[69] Similar to the e-Line the MJB4 functions as a microscope, in addition to being a system for lithography, naturally using light instead of electrons.

MJB4 has an irradiance of 18.8 mW/cm^2, and with a wavelength range of 350-450 it is compatible with SU-8. Seeing that the Department of Biomedicine already has experience with SU-8 on the MJB4, but with larger structures than what is intended for this thesis, a rough optimization has already been conducted. The challenge is to perfectly adapt it to the small structures used in this work.

3.3 Zernike Institute in Groningen, Netherlands

As a consequence of limitations to the atomic force microscope available at the Department of Physics and Technology, one week of AFM measurements were conducted at the Zernike Institute for Advanced Materials in Groningen. The AFM used in Zernike was a Scientec 5100 equipped with a silicon cantilever with tip radius $<$10 nm and 46 N/m force constant. All images were recorded in contact mode. The

data processing was conducted using Gwyddion, a free and open source software, covered by GNU General Public License.

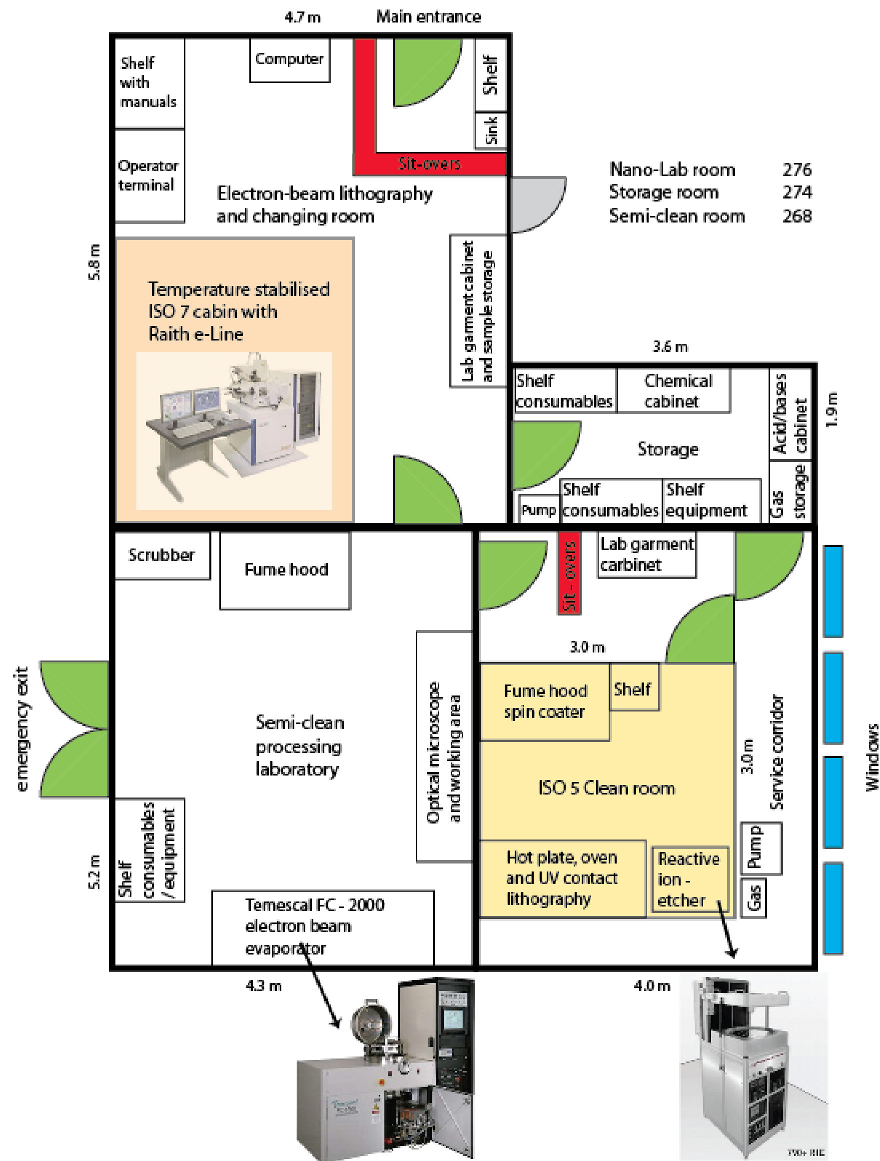

Figure 3.7: Schematic of the UiB NanoLab. Image originally uploaded to the NanoLab's wiki by Melanie Ostermann.

Chapter 4

Sample Preparation

The following chapter describes how the equipment and facilities are used to manufacture optimal surfaces for use as anti-fouling and icephobic optical windows. At first a description of how one may design such a surface will be given, then follows a detailed description of how the samples are handled from being received until complete with structures. At the end a brief description of how one would characterize the resulting sample is given.

4.1 Designing Surface Structures

As mentioned in Chapter 2, wetting and ice-phobic properties are influenced by surface features. How these features are designed will therefore be of relevance to the wetting and necessarily the ice-phobic properties of the substrate.

Should one use electron-beam lithography, the design can be directly implemented in the software, and the beam will follow the given path. But for photolithography it is most common to use a mask, as this will be more efficient and one does not have to worry about focusing the light in one spot. This mask can be made of for example soda lime glass, quartz or a polyester film, depending on the required applications. For this work a soda lime mask with a low reflective chrome finish has been used as it easy to clean, relatively stable, and is compatible with the wavelengths intended for this work. The mask was designed in-house and then ordered from J.D. Photo-Tools in the UK.

4.1.1 Mask layout

A matrix of 10 different patterns was created. They all consisted of squares, circles or hexagons in a two-dimensional array, either simple cubic (SC) or hexagonal close packing (HCP). The patterns were made with both varying pitch, i.e. distance from one point to the equivalent point on the neighboring structure, and with varying size. The overall layout is shown in Figure 4.1. Details on the individual matrix elements are given in Table 4.1 and Figure 4.2. Once the lithographic procedure has been optimized for the size features given here one may conduct more systematic studies of varied pitch and feature diameters.

The mask was designed using Raith's software "e_Line" - a program for designing recipes in electron beam lithography and then sent to J.D. Photo-Tools. The black areas of Figure 4.2 were blanked out, while the background was covered with

chromium. It is in other words a darkfield (negative) mask. This allows for light to pass through the squares, circles or hexagons. The result after exposure and development would therefore be square, circular or hexagonal holes for a positive photoresist, and pillars for a negative photoresist.

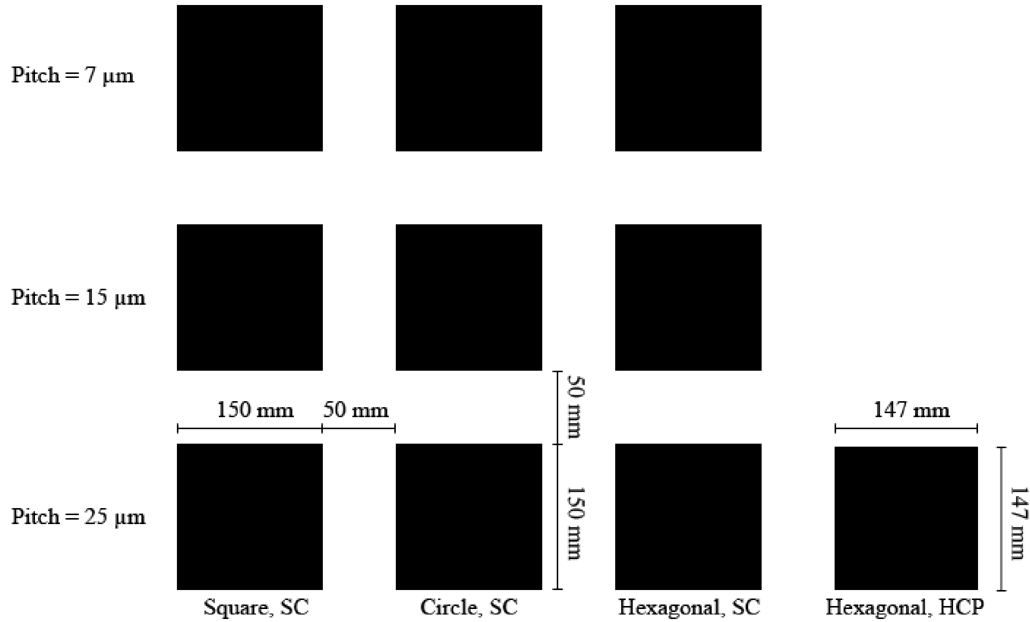

Figure 4.1: Overall layout of mask matrix, with details on each array given in Figure 4.2.

Table 4.1: Description of the dimensions in each array, whereas the lengths "X" and "Y" are indicated in Figure 4.2. The abreviations SC and HCP means simple cubic and hexagonal closed packing, respectively.

Structure	**Pitch (P)** [µm]	**X** [µm]	**Y** [µm]	**Reference**
Square, SC	25	10	N/A	Figure 4.2a
	15	5	N/A	
	7	5	N/A	
Circle, SC	25	10	N/A	Figure 4.2b
	15	5	N/A	
	7	5	N/A	
Hexagonal, SC	25	10	11.55	Figure 4.2c
	15	5	5.77	
	7	5	5.77	
Hexagonal, HCP	25	10	11.55	Figure 4.2d

Literature often uses either square or circular arrays, as is used here, but adding the hexagonal structures should allow for a higher surface area and possibly varied wetting properties. Similarly, the hexagonal closed packing is the optimal two-dimensional packing, allowing for a highest possible surface area per unit area, as compared to the simple cubic packing. To the best of my knowledge hexagonal closed packing of pillars or wells for smart surface purposes has not been reported in

literature. One could increase the surface area by creating more complex structures than squares, circles or hexagons, but doing so is more of an optimization problem and should therefore be investigated at a later stage.

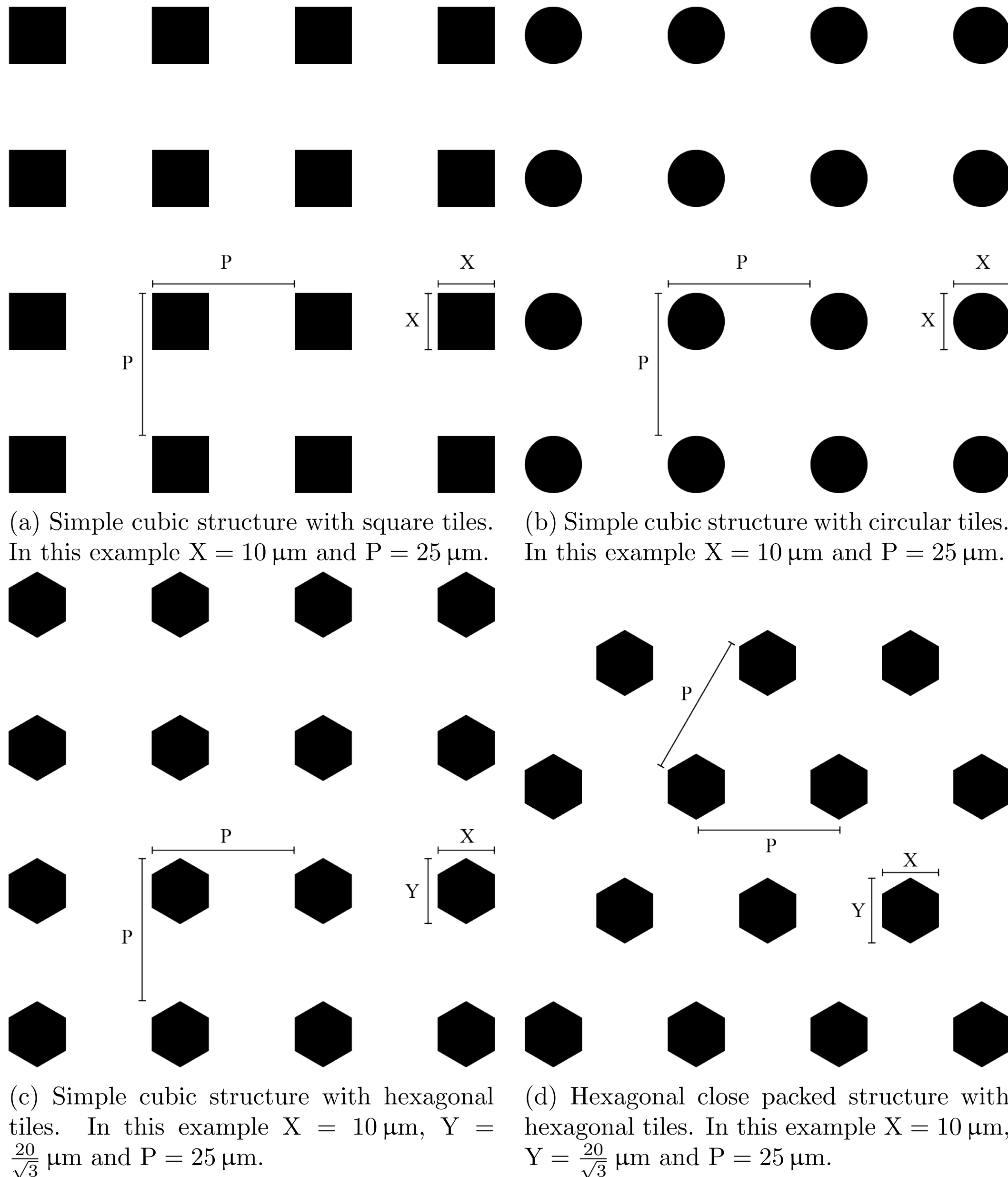

(a) Simple cubic structure with square tiles. In this example X = 10 µm and P = 25 µm.

(b) Simple cubic structure with circular tiles. In this example X = 10 µm and P = 25 µm.

(c) Simple cubic structure with hexagonal tiles. In this example X = 10 µm, Y = $\frac{20}{\sqrt{3}}$ µm and P = 25 µm.

(d) Hexagonal close packed structure with hexagonal tiles. In this example X = 10 µm, Y = $\frac{20}{\sqrt{3}}$ µm and P = 25 µm.

Figure 4.2: Detailed view of each array in the matrix as shown in Figure 4.1.

4.1.2 Design Parameters

The reasoning for choosing various geometries such as circles, hexagons and squares is to investigate whether the structure shape influences the wetting properties by keeping the packing ratio constant, i.e. same pitch value and size, but changing the shape to vary the surface area. The dimensions were chosen according to previous reports.[32,39,48] Similarly the pitch value is changed to investigate how it influences the contact angle and wetting state. In the case of Jung and Bushan (2009) they showed a transition from the Cassie-Baxter to the Wenzel wetting state at approximately 25

μm pitch value.[39] Zhang et al (2013) reported that micropores of 10 μm showed the highest coalescence frequency of microdroplets, reducing the problem of condensing water droplets penetrating the structures and thus possibly maintaining the Cassie-Baxter wetting.[32]

Herminghaus (2000) reported that it should be possible to make a surface hydrophobic, even if it was initially hydrophilic, by structuring the surface. Depending on the results this idea is to be implemented on sapphire, if needed. We can in other words control the wetting state by controlling the surface features.

4.2 Structuring Using Photolithography

Structuring of samples is a complex process, with many variables which can influence the final result. One has to be vary of the room temperature and humidity, but also substrate material, sample cleaning and spin-coating speed, to mention some. Therefore the following subsection will detail the procedure for structuring surfaces, with a summary in Figure 4.4.

4.2.1 Samples

The first step to consider is which material to use. For this work two materials have been used, silicon and sapphire.

Silicon substrates

The silicon wafers were of <100> orientation with a layer of silicon nitride, Si_3N_4, which was 200 or 500 nm thick. The thickness of the nitride layer was not relevant as no processing was done through these layers. The wafers were delivered from Si-Mat - Silicon Materials, and have a diameter of 2 inches or 100 mm. Either type can be cut along the crystal planes to obtain smaller samples, but by doing so it will be harder to obtain homogeneous deposition during spin-coating, which will be detailed in Section 4.2.3. Silicon is a well established material for structuring, making it a reasonable standard material for the preliminary investigations and photolithographic optimization. Silicon wafers are convenient for such a use as they are relatively cheap as compared to sapphire. Additionally silicon samples give a higher contrast in optical microscopy than sapphire.

Sapphire substrates

An obvious limitation for silicon wafers for use as optical windows is that it is not transparent to visible light. Sapphire, Al_2O_3, is therefore a perfect material, seeing that it has a high transmission of light ($> 80\%$) in the range of 0.2 - 5 μm in addition to being very durable.[70] The samples used in this thesis are listed in Table 4.2. They are all of <0001> crystal orientation.

The problem with the sapphire samples is that they are insulating, meaning that a conductive layer has to be deposited on top of the sapphire windows for SEM.

Table 4.2: Specifications of the sapphire (0001) windows used in the experiments. The crystal miscut indicates to which angle the surface angle deviates from the (0001) plane. Rewritten from Akhtar et al. (2015).[71]

	cp	**cp0**	**epi-polished**
Supplier	Freudiger	Freudiger	MTI corporation
Crystal growth method	Verneuil method	Verneuil method	Czochralski method
Diameter (mm)	12.67-12.73 with bevel edge of 45°, 0.2 mm	12.67-12.73 with bevel edge of 45°, 0.2 mm	12.7 ± 0.1
Thickness (mm)	1.55 - 1.60	1.55 - 1.60	1.57 ± 0.05
Crystal miscut	30° random orientation	$0 \pm 0.5°$	$0 \pm 0.3°$
Surface finish	Chemically polished (both sides)	Chemically polished (both sides)	epi-polished (one side)

4.2.2 Sample Cleaning

As will be discussed in Section 5.1, the properties of the samples will be dependent on the finish. Therefore it is important to be consistent on the substrate cleaning. The cleanliness of the procedure is of great importance for micro- and nanostructuring, seeing that contaminants will be relatively large and thus create large defect areas. Defects are often the nucleation sites for freezing. This is also why the samples are kept and transported face down in a curved sample holder, making sure only the edge of the substrate is touching the sample holder.

Three methods of cleaning have been used for this work: RCA multi-step method, piranha cleaning and AMI cleaning.

RCA multi-step method

The RCA multi-step method is used to remove the contaminants obtained in every step of polishing, storage and measurements.[72] The method consists of soaking the samples in a 3:1 solution of sulfuric acid (H_2SO_4) and hydrogen peroxide (H_2O_2) for 20 min at 80°C, then rinsing with ultrapure ion free water (resistivity greater than 18 MΩcm) and drying using nitrogen gas. Afterwards the samples are submerged in a 1:1:5 solution of NH_3, H_2O_2, and water for 20 min at 80°C, rinsed with water and dried. The last step consist of soaking the substrates in a 1:1:5 solution of HCl, H_2O_2, and water for 20 min at 80°C, rinsing and drying.[71] The sulfuric acid, the ammonia and the hydrogen peroxide are bought from BASF, while the hydrochloric acid is from Sigma Aldrich.

Piranha cleaning

A piranha solution is a 3:1 mixture of H_2SO_4 and H_2O_2. During piranha cleaning the samples are kept in the solution for 10 to 40 minutes. Seeing that the solution is highly exothermic, one should take special care as one might generate both high temperatures and corrosive fumes. One should therefore allow the solution to cool

before heating it slowly to the desired temperature. The piranha solution will remove most organic matter and hydroxylate the surfaces, i.e. add OH groups.

AMI cleaning

AMI is short for acetone, methanol and isopropanol (2-propanol). It is a regular cleaning method in cleanrooms which allows for the removal of contaminants. The three chemicals are bought from Merck Millipore. Seeing that these are easily available chemicals they are found in many cleanrooms as a way of easily removing contaminants. During AMI cleaning one will have the chemicals on wash bottles, hold what one will clean using tweezers and then rinse with acetone, followed by methanol and then isopropanol. This is followed by drying under a nitrogen stream. All of the equipment used during processing, e.g. tweezers and beakers, are cleaned using the AMI cleaning method.

4.2.3 Spin-Coating

Once everything has been cleaned one can start the deposition of photoresist. This is commonly done using spin-coating, as it allows for homogeneous structuring. Spin-coating involes depositing a resist on the substrate, and then spinning the substrate at high speed (in this work at 4000-5000 RPM). As a result the centripetal force will spread the liquid to a homogeneous liquid layer.

For this work a Chemat KW-4A Spin Coater was used, as mentioned in Chapter 3. Typically the samples are held in place by a vacuum pump which generates a lower pressure on the back. Seeing that the sample holder is made for 2 inch samples, the smaller samples, i.e. cut silicon or sapphire, has to be held in place using an adhesive. For the silicon samples this adhesive is a gel, delivered by the American company Gel-Pak, which is stuck to a 2" wafer. The sapphire samples are held in place using a small piece of double sided carbon tape which is placed on a 2" wafer.

When the sample is held in place, the photoresist is deposited using a syringe. Since AR-P 3540 has a high viscosity, the whole resist should be covered by the photoresist before initiating the spin. The two-stage spinning is used, whereas the first and slower spin stage is to spread the resist somewhat homogeneous before the final spin is initiated. An inverse power-law generally holds for the thickness dependence on the final spin speed.[73] The evaporation rate of the solvent is also of relevance, as this will influence the viscosity of the resist. After a certain time there will be no influence from increasing the spin time.

Some challenges might arise during spin-coating, causing defects on the sample surface which can be avoided. These are all illustrated in Figure 4.3. Should one obtain air bubbles in the resist this could also be present on the photoresist after spincoating. A possible solution is to leave the resist container open for a time. Air bubbles could also appear if the dispense tip is cut unevenly or has defects. Comets and streaks are obtained as a result of leaving the resist on the substrate for too long before deposition. It could also be that particles are present on the substrate which would prevent the fluid from spreading behind them, again leaving streaks or comets. A swirl pattern is obtain for too high acceleration or spin speeds, and for too short spin times. The center circle is seen when the sample holder is too small. Uncoated areas are obtain for insufficient dispense volume, e.g. the photoresist has

a high viscosity and does not cover the whole sample. Pinholes are obtained from air bubbles, particles in the fluid or particles on the substrate prior to dispense.[74]

As was mentioned earlier, some silicon wafers are cut along the crystal planes to allow for easier handling. The problem of doing so is that the samples end up being rectangular or square, with sharp corners. Spin-coating such samples allows for certain challenges which are not observed for circular samples. The edges of a square or rectangle causes significant turbulence which leads to uneven evaporation of the solvent and anomalies in both thickness and uniformity of the coated film.[75] For a square sample this is observed as a circular good area on the sample with diameter equal to the side length. The remaining area often has a different colour, seeing that a different deposition thickness will result in changes of light refraction. Brewer Science give a possible solution to this in their blog, saying that one may use a recessed spin chuck, i.e. a circular spin chuck with cavities the size of the square sample, as it will eliminate the air disruption.[75] This solution is not applicable here, seeing that the samples are randomly cut. As the silicon samples are used for preliminary investigations, this uneven deposition can be used as an advantage during optimization. When introducing a thickness gradient along the sample one can use the fact that a thicker sample requires longer exposure to observe whether a longer or shorter exposure time is required.

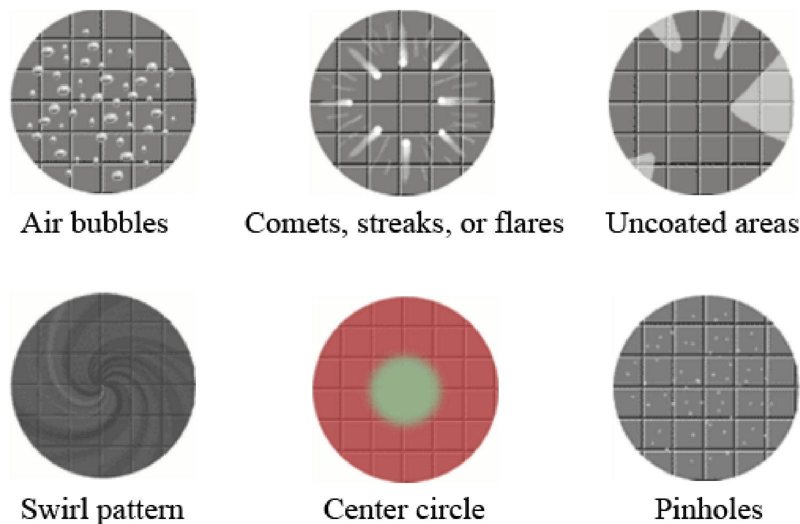

Figure 4.3: A figure illustrating challenges one might experience during spin-coating. Figure is from Brewer Science's web pages.[74]

4.2.4 Tempering

Following the spin-coating, a tempering step is conducted to evaporate the remaining solvent in the resist. For this work tempering is always conducted on a hot-plate, but could also be done using a convection oven though it usually requires a longer time. Seeing that the solvents used in the photoresists should not be inhaled, the hotplate was kept in the fume hood during the tempering procedure.

4.2.5 Exposure

One of the most critical steps during the sample structuring is the exposure step. As was mentioned in the previous chapter, the exposure was conducted using two setups; the in-house setup made by Reisinger and Maad, and the MJB4 at the Department of Biomedicine.

In-house setup

Using the setup made in-house by Reisinger and Maad, this step consist of placing the sample on sample holder indicated in Figure 3.1. Seeing that a soda lime mask have been used, this is placed directly on top of the substrate. Should one use a polyester film, this could be held in place using a pressure difference generated by a vacuum pump (as for the samples during spin-coating). This is unfortunately not possible for a soda lime mask. Therefore a hollow circular metal disk is placed on top of the mask to allow for a harder contact between the mask and the sample (seen in Figure 3.1a).

Alignment is critical to obtain perpendicular radiance and optimal results. Therefore one has to make sure the setup is aligned at all times. For this work alignment is done using a tubular spirit level. To ensure the mask is aligned, especially for small samples such as the sapphire samples, it is balanced using old or uncoated sapphire samples on the edges, making sure the mask does not rest with an angle on the substrate.

When the sample is in hard contact and properly aligned, the AC power plug is connected to the socket in the wall simultaneously as a timer is manually started. When the target dose is achieved, the power plug is manually disconnected from the socket.

MJB4

For SU-8 the exposure was conducted using the MJB4 at the Biomedicine Department. The samples are transported to the Department in the previously mentioned curved sample holders. Once there, the standard operating procedure for the MJB4 is followed. The sample is placed on the sample holder and the mask is mechanically pushed into hard contact with the sample. As the machine is a mask aligner, it will automatically align the sample with the exposure, allowing for perpendicular exposure. The exposure is automatic with an exposure time of ± 0.05 seconds accuracy, controlled by the built-in computer.

After exposure, the SU-8 is placed on two hot-plates at 65°C and 95°C for 1 minute each, for what is called a post-exposure bake (PEB). This is a necessary step for the SU-8, but an optional step for AR-P.

4.2.6 Development

To obtain a pattern from the exposed resist, the development step has to be conducted. This consist of using a chemical in which the exposed resist is soluble (positive type resist) or insoluble (negative type resist). For this work the chemical is some developer produced by the company that delivers the respective photoresist.

As for all other parts of the sample preparation, reproducibility is important. Therefore the samples are either immersed in the developer and held in place or alternatively one "washes" the samples with developer using a wash bottle containing developer. Some problems occurred with the separation of AR 300-35 and H_2O in solution, meaning that a magnetic stirrer had to be used to mix them properly. Manual stirring is random and not reproducible, meaning that all stirring should be conducted using magnets.

The sample is developed for the indicated time and if immersed taken out of the solution. Following development is usually a "stopper", a chemical which neutralizes the developer. The sample is either immersed or rinsed with the stopper. For AR 300-35 the stopper is de-ionized water and for the SU-8 developer the stopper is isopropanol.

After development the photoresist structures should be visible using a microscope. At this point there are two possible pathways: generating pits in sapphire using selective chemical etching or generating sapphire pillars using solid-state conversion of aluminium. Each of the pathways will therefore be detailed in the following subsections.

4.3 Solid-State Conversion of Al to Al_2O_3

The solid-state conversion of aluminium to sapphire (Al_2O_3) was first reported by Park et al. (2005), and in 2013 Jeffrey Biser wrote a thesis on the topic, but both with a focus on LED applications.[76,77] This is to the best of my knowledge the first time this procedure is used for structures at the micron-scale.

The first step of this procedure is to overexpose the resist remaining after selective exposure and development of the positive photoresist AR-P 3540. The exposed resist is then covered by a homogeneous layer of aluminium deposited using the Temescal. The thickness of this aluminium layer will be determinative for the final height of the sapphire pillars. Following deposition a development of the exposed resist will be conducted, also known as a lift-off procedure. This development will remove the remaining resist together with the aluminium deposited on top. The result will be single aluminium hill structures. The developer is in this case agitated manually seeing that the whole solution is placed in a sonicator for some seconds. This allows for assisted removal of the aluminium which in some cases could prove challenging to remove. The metal is likely to be removed as a single layer, making it easy to determine when the procedure is done. It should be noted that the developer used, AR 300-35 does not attack the aluminium, making it a viable choice for lift-off.[58]

The last step is the actual solid-state conversion. The sample is placed in a convection oven with controlled heating rates and temperature, heating it to 450°C for 24 hours, then cooled before annealing at temperatures of about 1000°C. Followed by controlled cooling, the result should be sapphire pillars.

4.4 Wells in Sapphire by Selective Etching

When generating well structures one has to deposit 25 nm SiO_2 on the substrate prior to photoresist deposition. This layer will work as an etch mask for the wet-

etch. After the regular photolithographic procedure has been conducted one is, as previously mentioned, left with wells in the positive photoresist. When placing the sample in the reactive ion etcher (RIE), these wells will be the only places where the SiO_2-layer will be exposed to the plasma. The gas used in the RIE is CHF_3 and it is ionized at 7 mTorr pressure, with 100 W power for 5 minutes. The gas flow used is 15 sccm. The result should then be holes in the SiO_2 layer with the same diameter as the photoresist wells.

Following this step the remaining photoresist is removed using exposure and development. An alternative would be AMI cleaning, as SiO_2 will not dissolve by AMI while the remaining resist will. Then a wet-etch of sapphire will be conducted with a solution of sulfuric acid and phosphoric acid. Which ratio these are mixed will be determinative of the resulting well shape.[78–80] The time and temperature is also varied to obtain the optimized result.

After wet-etch, the remaining SiO_2 layer will be removed using the same RIE procedure, but for 10 minutes, making sure all the silicon dioxide is gone. The result will be cavities in the sapphire, often referred to as etch pits.

4.5 Characterization

The results are at every step of the procedure investigated using optical microscopy as this is both quick and non-invasive.

Because of resolution limitations in the optical microscope, a scanning electron microscope (SEM) is used to accurately determine both the size and shape of the structures. Seeing that sapphire is a dielectric material, i.e. an electrical insulator, the conductivity is very low, with a resistivity between $5 \cdot 10^{18}$ to $2.9 \cdot 10^{19}\,\Omega$cm at 293 K, depending on direction.[70] This means that one has to deposit a metal on the sample prior to SEM imaging. The clips of the e-Line sample holder are not able to hold the relatively thick sapphire samples in place. Carbon tape is therefore used to hold the samples in place.

SEM has an excellent depth of field due to the very narrow electron beam, making it useful when understanding the surface structure of a sample. But when inspecting height profiles of structures other equipment such as AFM and height profilometer is preferred.

To investigate the anti-fouling and icephobic properties one is first interested in the wetting properties of the sample. This is measured by the contact angle (as was detailed in Section 2.1) using the Dataphysics OCA 20L.

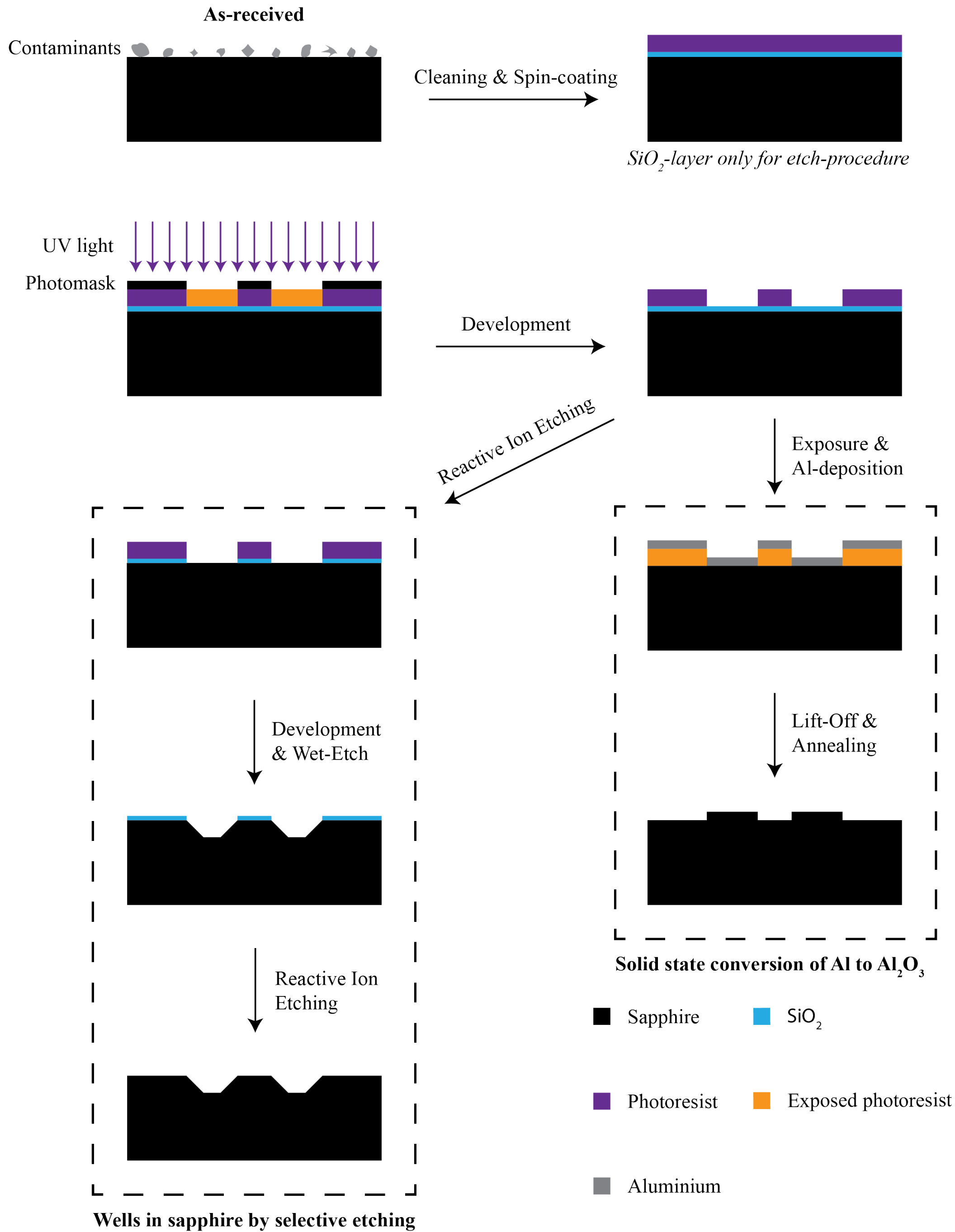

Figure 4.4: Schematic summarizing the sample preparation procedure. The blue SiO_2-layer is not used for the solid state conversion of Al to Al_2O_3, yet indicated in the first figures to show that it must be deposited before spin-coating.

Chapter 5

Results and Discussion

The thesis objective is to establish a set of model surfaces that can be tested as smart surfaces for anti-fouling applications in harsh environments. An example of use could be in sensors on oil platforms situated in an arctic climate, which means that, in addition to being anti-fouling, the surfaces have to be icephobic. As a result the final product should be omniphobic, i.e. repellent to both polar (e.g. water) and non-polar liquids (e.g. oil). As detailed in Chapter 2, the wetting properties of a surface is manipulated by structuring the surface, and by doing so on a sapphire substrate it is believed that one can obtain omniphobic surfaces.

Not only the structuring on the micron scale, but also the properties on the atomic scale, are likely to influence the overall properties of a smart surface. Therefore prior to microstructuring was done a systematic investigation of the surface properties of commercially available sapphire surfaces was conducted. These results are presented in Section 5.1. Then follows the work on the structured surfaces. The optimal microstructuring conditions are given in Appendix A.

5.1 Unstructured Sapphire Windows

Sapphire substrates are usually prepared by cutting the crystal at a small angle to a particular plane followed by polishing. There are various ways of polishing the surface such as ultrafine diamond powder polishing, chemical-mechanical polishing, and electrical-chemical polishing, to mention some. The sapphire surface properties are observed to be influenced by the polishing, surface treatment method, initial cleanliness and crystal miscut from target plane.[71]

A study of the underwater-oil wettability of sapphire (0001) surfaces with different qualities were reported by our research group last year with the author of this thesis as co-author: Akhtar et al. (2015).[71] Three different samples were tested, all of which have been used for structuring in this work. These samples are the cp, cp0 and epi, as was given in Chapter 4 in Table 4.2. Without any cleaning, i.e. keeping the samples "as-received", they were all hydrophilic in air, with apparent contact angles $\sim 80°$. cp0 and epi-polished were highly oleophobic in water, i.e. $\theta^*_{OW} > 130°$, while cp was only slightly oleophobic with $90° < \theta^*_{OW} < 110°$ (see Figure 5.1a).[71]

As is seen in Figure 5.1b, the wetting properties were considerably changed after the RCA cleaning. The windows became superhydrophilic, with water contact angle in air, $\theta^*_W < 30°$. Additionally, cp had an increased contact angle for oil in water. The increased polar affinity, and increased nonpolar (oil) repulsion, is likely to

originate from the oxygen surface atoms in sapphire (Al_2O_3) no longer being covered by a contamination layer. Additionally even though the surfaces are nominally flat, they still contain surface features that influence the wetting properties. As can be seen in Figure 5.2, there were scratches on the cp and cp0 of respectively 2.5 nm and 1.5 nm depth. Once the surface is RCA-cleaned these defects can trap water when submerged in water for oil in water contact angle measurements. This trapped water layer is believed to protect the surface from oil wetting which leads to higher oil contact angle for these surfaces after RCA cleaning.

These results show that sapphire can be used for underwater measurements in an environment with oil fouling, as the surface will repel the oil. The RCA cleaning is only a temporary solution, as the surface may get contaminated after cleaning. The need for a more robust solution is clear. This work inspired us to investigate well structures generated using AR-P 3540 to enhance the hydrophilic character and thus oil repulsion under water. Pillar structures with low solid-liquid contact area, referred to as f_{sl} in Section 2.1.2, will on the other hand allow for hydrophilic surfaces to become hydrophobic by the Cassie-Baxter wetting model. Such structures can be used to repel water in low humidity environments and are therefore made using SU-8 2002. The main focus in this work will be on making structures hydrophilic in air and superoleophobic under water.

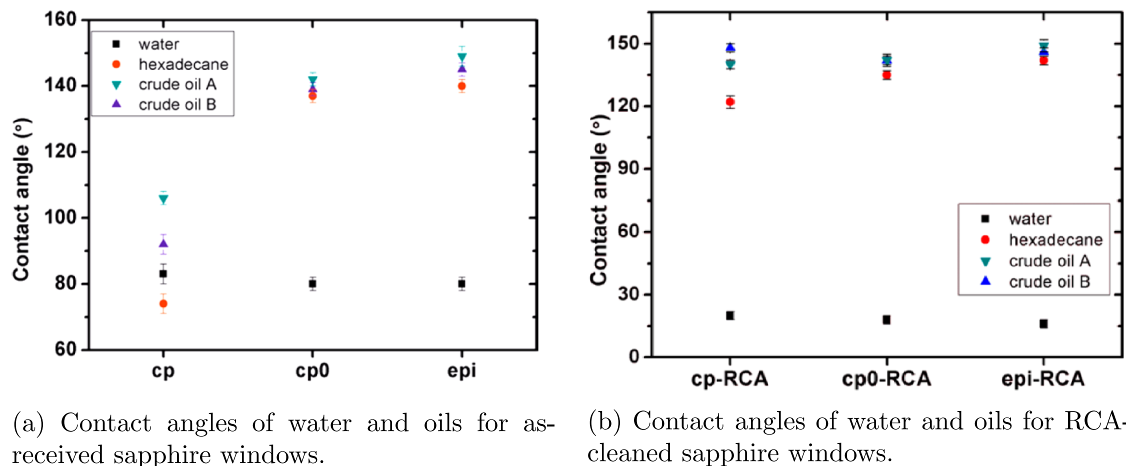

(a) Contact angles of water and oils for as-received sapphire windows.

(b) Contact angles of water and oils for RCA-cleaned sapphire windows.

Figure 5.1: Contact angles of as-received (left) and RCA-cleaned (right) sapphire windows from Akthar et al. (2015).[71]

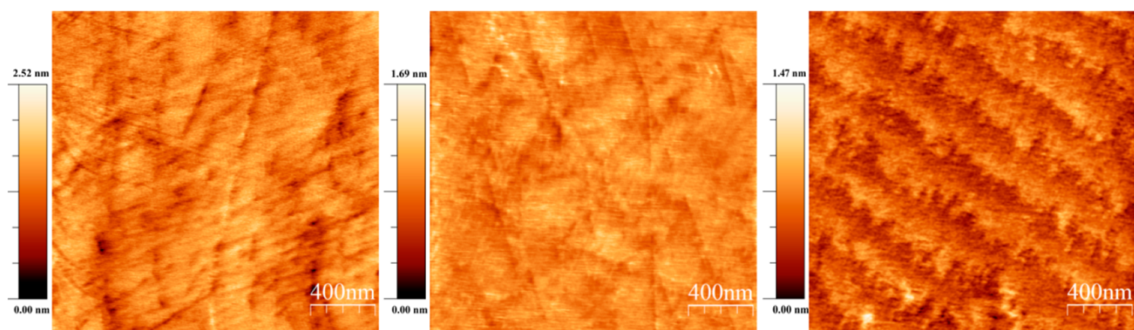

Figure 5.2: AFM images of RCA-cleaned sapphire windows. From left to right; cp, cp0 and epi-polished. Image from Akthar et al. (2015).[71]

5.2 Surface Structuring

Producing a pattern into, or onto, a material is a complex process. As mentioned in the previous chapters one can generate the pattern on a sample surface by deposition, or by removing parts of the sample using for example selective etching. For the photolithographic part of the procedure SU-8, developed by MicroChem, and AR-P 3540, developed by AllResist GmbH, have been used. While SU-8 is a common photoresist for patterning surfaces[59,81–83], AR-P 3540 has seen limited use in the literature, also in the Nanophysics group.[84] Because of this an optimization of the photolithographic procedure on AR-P has been necessary, in addition to a basic optimization for the MJB4 setup with SU-8.

Most of the optimization procedures were conducted on samples of silicon (Si) with a coating of silicon nitride (Si_3N_4) of 200-500 nanometers. The thickness of this layer is not of relevance as no processing was done through this layer, i.e. the procedure was stopped after successful development. Seeing that the final product is to be used as optical windows, the procedure has to be done on sapphire after optimization, as Si + Si_3N_4-samples are not optically transparent. The motivation for using silicon during optimization is that it is easier to work with during the PL-procedure and relatively cheap (as the larger samples can be cut to smaller pieces).

5.2.1 AR-P 3540 Optimization

The Nanophysics group at the Department of Physics and Technology has not worked extensively with the AR-P 3540 photoresist. The Post Doc. Xiadong Guo is the only one who had worked with it, but as his work primarily consisted of larger scale structures (millimeter-scale) he did not need to focus on smaller details at the micron-scale. His parameters, in addition to what is given by AllResist (in the product information), served as starting points when optimizing this procedure for structures on the micron-scale, and is given in Table 5.1.

Table 5.1: Starting parameters for the AR-P optimization procedure, as given by Xiadong Guo and AllResist GmbH.[57] DI H_2O is short for deionized water, i.e. water with chemically removed minerals. Unless otherwise specified all AR-P samples have a slow spin speed of approximately 600 RPM for circa 10 seconds before the 4k RPM spin.

Parameter	**X. Guo**	**AllResist**
Spin speed	4000 RPM	4000 RPM
Spin duration	60 s	60 s
Tempering	90°C for 120 s	100°C for 60 s
Exposure	35 s†	120 mJ/cm^2
Developer	1:1 (AR 300-35:DI H_2O)	1:1 (AR 300-35:DI H_2O)
Developing time	30 s	60 s

† At the home-made setup one has not calculated the energy per area, and exposure time is therefore given instead.

As Guo had worked with the setup used in this thesis, it was considered natural to follow his procedure at first. To test these parameters a mask already available in the Nanophysics group consisting of Fresnel zone plates were used. Fresnel zone

plates are lenses used to focus light or particles using diffraction instead of refraction or reflection.[85] An optical microscopy image of the zone plate is given in Figure 5.3a.

The parameters given by Guo were not successful, and after some tweaking of the recipe, a decent result was obtained using the parameters presented in Table 5.2 (see Figure 5.3b). This proved that the method works for larger structures, allowing for investigations on a smaller scale.

Table 5.2: Parameters used during first successful result for the AR-P optimization procedure. DI H_2O is short for deionized water, i.e. water with chemically removed minerals.

	Parameter used
Spin speed	4000 RPM
Spin duration	60 s
Tempering	100°C for 5 minutes
Exposure	36 s†
Developer	1:1 (AR 300-35:DI H_2O)
Developing time	35 s

† At the home-made setup one has not calculated the energy per area, and exposure time is therefore given instead.

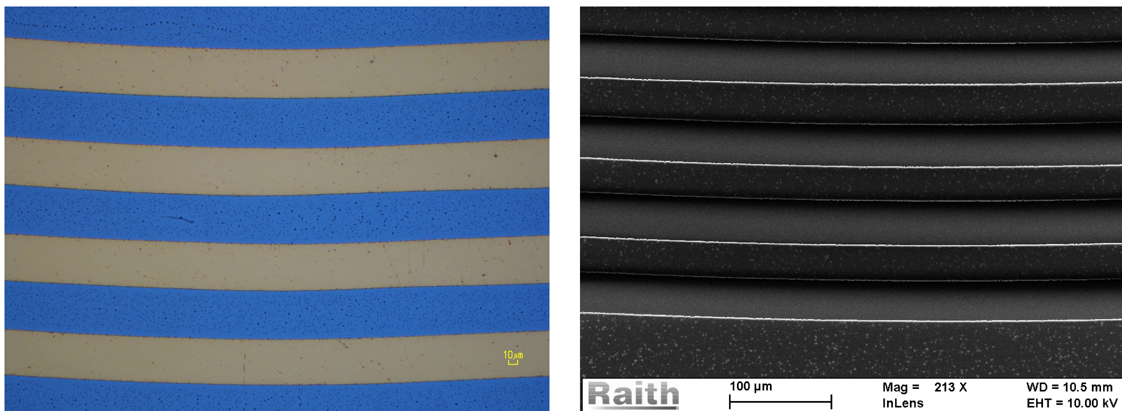

(a) Optical microscopy image of mask available in the Nanophysics group consisting of several radially symmetric rings. The grey is the metal which will reflect the light, while the blue is the background, as the mask will be optically transparent in these areas.

(b) SEM image of resulting pattern after using group's mask on sample deposited with AR-P that has been tempered at 100°C for 5 minutes, exposed for 36 seconds and developed for 35 seconds in an 1:1 AR 300-35/DI H_2O-solution.

Figure 5.3: Optical microscopy picture of the Fresnel zone plate mask (left) and resulting pattern using photolithography (right).

The mask detailed in Section 4.1.1 which was designed in-house, but sent to JD Photo-Tools, was a more challenging mask for photolithographic applications. It consists of smaller structures close to the resolution limit, but also sharp corners (squares and hexagons) unlike the fresnel mask which only consisted of rings. After some trial and error, an exposure time of 35 seconds and a 31 seconds developing time resulted in the best results with this new mask. Several samples were made to investigate the effect of changing exposure time and developing time (see Table

5.3). All samples had the spin and tempering parameters as was reported in Table 5.2, with the exception of using 90°C instead of 100°C. The increased tempering time, as compared to Guo's initial values, seemed to reduce the amount of hole defects which are visible as small white dots in the bottom of Figure 5.3b, though later investigation seemed to indicate that an increased annealing time has little influence on the procedure. Seeing that most samples are 100 mm wafers cut to an area of approximately 2-4 mm^2, only one type of structure fit each sample, e.g. squares with side length of 10 μm and pitch value 25 μm. The sample labelled "Reference" (Table 5.3 and Figure 5.4) had the exposure and developing time which had resulted in the best results at that time.

Table 5.3: Parameters used when investigating the effect of exposure and developing time. All samples were developed in a solution consisting of 1:1 AR 300-35/DI H_2O without agitation. To stop the developing the samples were rinsed with DI H_2O. All samples consisted of squares with side length 10 μm and pitch value 25 μm.

Sample ID	**Exposure time** [s]	**Developing time** [s]
Reference	35	31
D-2	35	29
D+2	35	33
E-2	33	31
E+2	37	31

After creating the samples given in Figures 5.4 and 5.5 it was discovered that the photoresist used had expired. But this does not make the results useless. AllResist claims that the resist may be used for limited purposes after exposure date, which could be possible for the larger structures, but when detailing structures on the micron scale it might be a problem after all. The holes and cracks observed in all previously mentioned samples seem to be a direct result of expired resist, as they are not present using a new resist as can be seen in for example Figure 5.6. Additionally it proved difficult to reproduce these results using the expired resist, which could mean that the reproducibility is rather limited with an expired resist as well. But the fact that the expired resist cannot be used for small scale structures, i.e. structures smaller than 30 micrometers is to be considered a result in itself. By comparison the resist used for electron-beam lithography, PMMA (AR-P 672), does work for an extended period of time after expiration date.

Despite being an expired photoresist, the results are useful when investigating the effects of exposure and developing time. By comparing Figure 5.4 to Figures 5.5c and 5.5d it looks as though increasing the developing time will reduce the thickness of the edge profile within the square, i.e. the transition from photoresist to substrate. This could suggest that the developing time for the reference sample is too short. This increased size of the edge for underdeveloped samples is also visible for the sample labeled D-2. This is because underdeveloped samples still have some of the exposed resist left, which in this case is visible by the increased edge size. For an optimized photoresist the walls will be more vertical than observed here.

Changing the exposure time seems to have a larger effect on the results with the variation of ±2 seconds, as compared to the influence of changing the developing time. The E+2-sample (Figure 5.5g and 5.5h) shows rounded edges and squares

with side lengths larger than the target length of 10 μm, which is expected to be indicative of overexposure. The E-2-sample (Figure 5.5e and 5.5f) shows some quite different effects, which only partly may be explained by underexposure. First of all it is evident that the squares are too small, but there are also notably more holes in this sample as compared to the other figures. As these holes are most dense close at the exposed areas, this could indicate that the developer dissolve the exposed areas partially by several holes and not uniformly. It is hard to say for sure, seeing that the resist is expired and might give other results than that of a fresh resist.

Even though the resist was expired, it is helpful to know what the sample might look like with over-/underexposure and over-/underdevelopment for more efficient optimization procedures in the future. As will be detailed in Section 5.2.3, changing the exposure and developing time for a negative photoresist will be quite different.

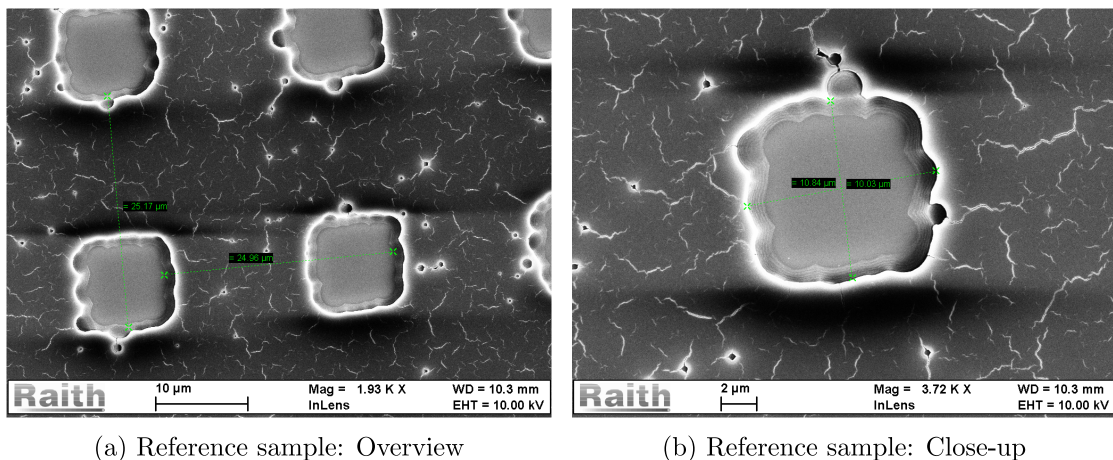

(a) Reference sample: Overview

(b) Reference sample: Close-up

Figure 5.4: Reference: 35 seconds exposure, 31 seconds developing time. Indicated distances measured using Raith's built-in measurement tools.

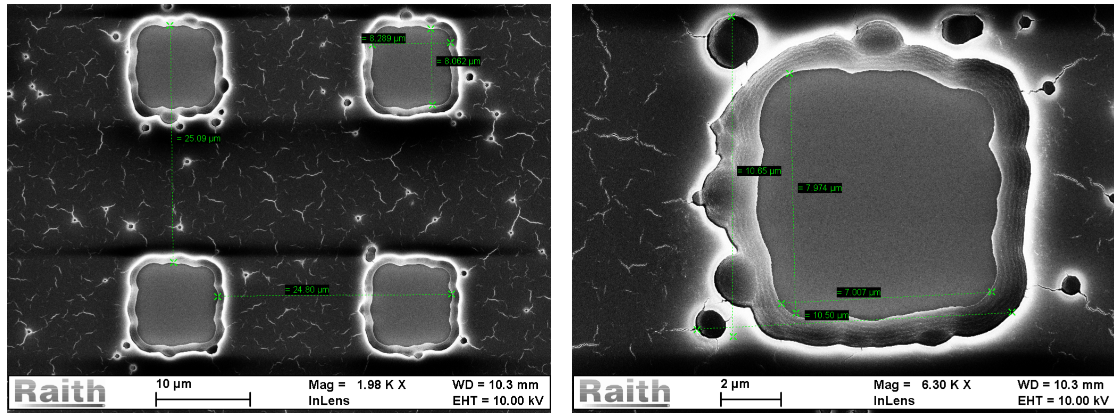

(a) D-2: Overview

(b) D-2: Close-up

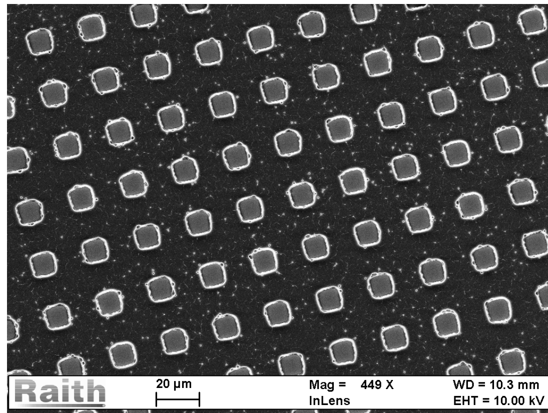

(c) D+2: Overview

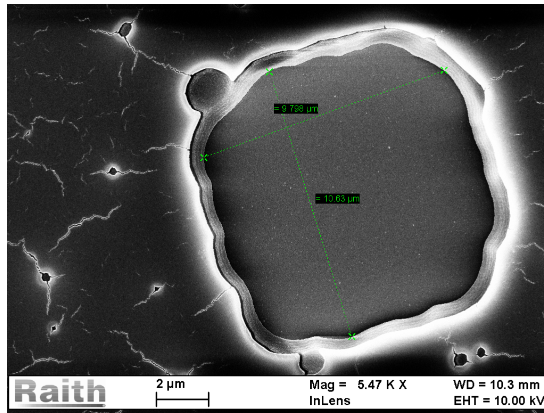

(d) D+2: Close-up

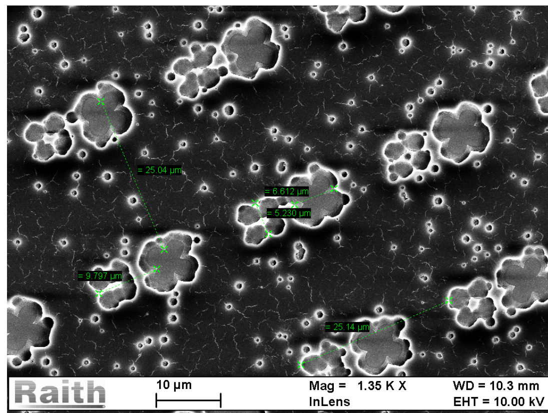

(e) E-2: Overview

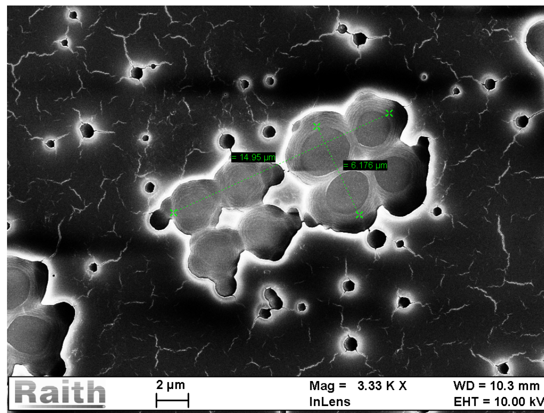

(f) E-2: Close-up

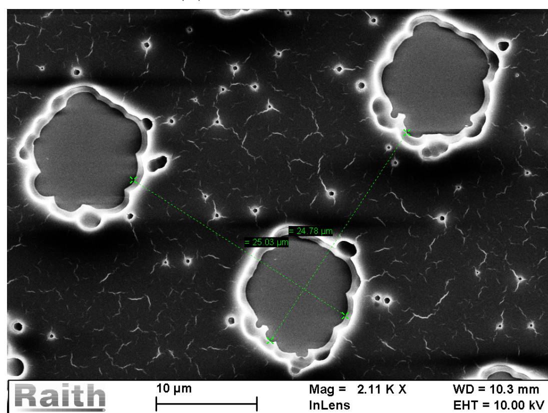

(g) E+2: Overview

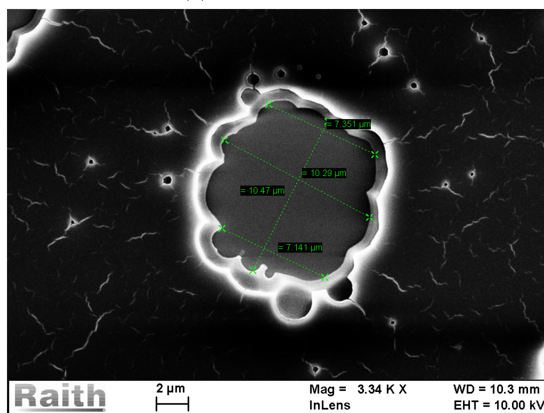

(h) E+2: Close-up

Figure 5.5: Samples with variable exposure- and developing times.

New photoresist

Using the same parameters as for the above mentioned "Reference", the results were not optimal for the fresh resist. When changing the developing time to what is given in AllResist's DataSheet, i.e. 60 seconds, the results were remarkably better. After some trial and error the optimum exposure time for squares and circles of pitch value 25 µm and side lengths 10 µm was found to be 28 seconds (see Figure 5.6).

The white halo observed in Figure 5.6 and the following SEM images is due to increased electron scattering at the edges of the structures.[86] The InLens detector was always used, and it is a secondary electron detector collecting signal from the secondary electrons produced by the beam and the backscattered electrons.[87]

From Figure 5.6 it is evident that the holes and cracks observed in Figures 5.4 and 5.5 are non-existent. It is believed that these defects might be the formation of particles which is caused by the precipitation of the light-sensitive component in the photoresist. These particles are $> 0.2\,\mu m$ which is consistent with the size of the holes. The steadily declining concentration of the light sensitive component will influence both development rates and resist adhesion.[58] One should therefore check the expiration date before conducting further experiments should these defects be observed. Some holes are still present, but they do not seem to be penetrating the photoresist, and could be explained by air bubbles being formed in the photoresist or by small particles being present on the substrate prior to dispense. These small particles could come from cutting the wafers into smaller pieces, but such particles should in theory not be present as the sample has been thoroughly washed.

The rounded corners of the square structure is of some interest, as sharp edges and corners are desired when creating more complex structures such as hexagons. Increasing the complexity would allow for structures that have a larger surface area and thus a higher roughness factor, R_f, than regular squares or circles. But eliminating this rounding of the corners has proven to be difficult, especially using the setup in the UiB NanoLab. This could be due to the LEDs having a directivity radiation of $\sim 15°$, allowing for exposure at areas covered by the mask. It could also be that indene carbonic acid derivative generated by the exposure of AR-P 3540 could have some diffusion in the photoresist, allowing for unexposed areas to be soluble in the developer. These rounded corners is also believed to be more prominent for softer contact between the mask and resist. For the in-house setup it is likely that the mask is in soft contact, as there is no mechanical pressure or vacuum involved. As a result one could obtain a diffraction effect, i.e. slight bending of light as it passes around the edge of the mask opening. This effect, in combination with interference, is likely to have a greater effect on resists deposited with a high thickness or high density masks, i.e. masks where the distance between two mask slits gets close.[88]

As for the squares, the corners of the hexagons also ended up being rounded, making them look like circles. There is not much to do with the rounded corners using this setup, as it is believed that the accuracy of the exposure time is too low. This originates from having to turn on and off the exposure manually by connecting and disconnecting the power plug and the power socket. In addition the exposure time is measured using a manual stopwatch. The exposure time can therefore be estimated to have an error of at least ± 0.5 seconds. Reducing this corner-defect might require the adjustment of exposure time at a higher precision, which is not possible using the current setup.

Using 32 seconds exposure and 60 seconds developing time the result given in

Figure 5.7 was obtained. As the structures are measured to have a diameter of 5.6 μm, the resist has been overexposed. It was attempted to reduce the exposure time by one second, but this resulted in underexposed structures. It is likely that the optimal exposure time was somewhere between 31 and 32 seconds.

The inaccurate exposure time and soft contact of mask had the greatest influence on the smallest structures of diameter 5 μm and pitch 7 μm, as is visible from Figure 5.8. It is evident that the wells are not perfectly circular. It is believed that the soft contact, the inaccurate exposure time and possibly interference effects are the main contributors to these bad results. Light passing through neighbouring mask openings, and light being reflected from the substrate could cause these interference effects with the incoming light. Interference and diffraction is of such a nature that all other parameters must be optimized before one can attempt to limit those effects.

As is seen in Figure 5.8b and 5.6b the side walls are approximately 200-500 nm. The seemingly layered structure of the edge originate from the interference between incident light in the sample and reflected light from the substrate (in this case Si_3N_4). A detailed description of this is given in Appendix B. Seeing that the inside of the exposed substrate is approximately 4.5 μm in diameter it could be argued that the sample is underexposed. But increasing the exposure would result in what one may call "linkage" between the wells, i.e. exposed areas connecting them, an effect which will be observed for the densest structures in Section 5.2.3 as well.

The sample seen in Figure 5.8 was tempered at 100°C for 1 minute after AR-P deposition, exposed for 34.5 seconds and developed for 60 seconds, unlike the regular 90°C for 5 minutes as it gave better results for this pitch value. 100°C for 1 min were the original parameters given by AllResist. Having 90°C for 5 minutes or 100°C for 1 minute did not seem to be critical for the results, though it could have some effect on the hole defects which again are visible in the overview picture (Figure 5.8a). These holes could also originate from air bubbles in the photoresist, as mentioned previously, which appears if the resist is deposited too quickly after opening the container, if the resist is applied too fast with the pipette, or if the sample is insufficiently tempered, allowing for the evaporation of solvent during exposure.[58]

An optional step to increase the etch resistance of AR-P during dry etching, is to perform a post-exposure bake. It is given that the post-exposure bake (PEB) should be conducted on a hotplate for 1 minute at 115°C, but doing so changed the outcome from optimal to bad results, i.e. similar to that given in Figure 5.5f. It was attempted to reduce the PEB time to 10 and 2 seconds, but both yielded drastic changes to the results given the same exposure and developing times. It has to be noted that this step was conducted prior to development in this work, as was the requirement for SU-8. This step could have a smaller effect on the final result if it is conducted after development and prior to etching. This was not further investigated as there was no need for such a PEB-step, as AR-P 3540 was deposited with sufficient thickness for our etching experiments. It was therefore removed from the procedure as it is also listed as an optional step in the AR-P 3540 data sheet.

For AR-P 3540 development, using AR 300-40 and H_2O, experiments indicate that it is not arbitrary which way the sample is placed in the solution during magnetic stirring. If the structured side is facing the rotational flow, i.e. the flow directly hits the structures, experience suggests that most of the resist will be removed, likely due to drag. By turning the sample around so that the back side is facing the flow

direction, the optimal results were obtained.

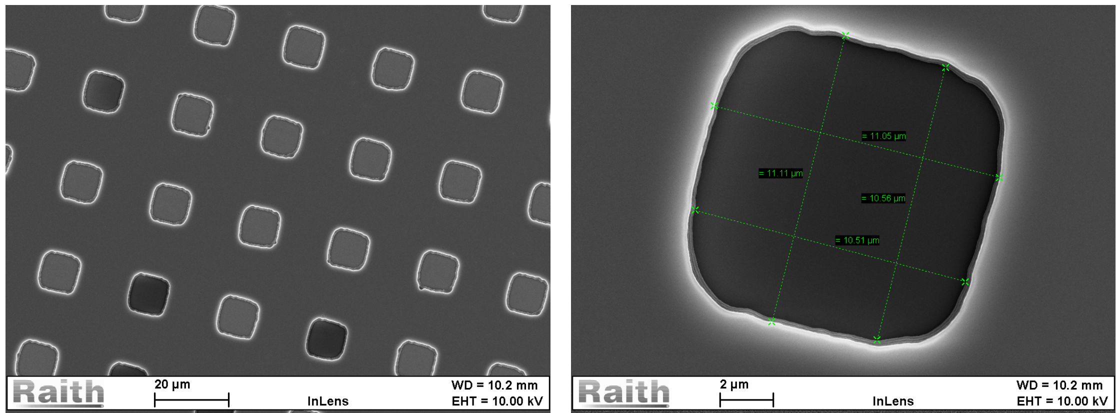

(a) Overview of squares with target pitch value 25 µm.

(b) Close-up of square with target side length 10 µm.

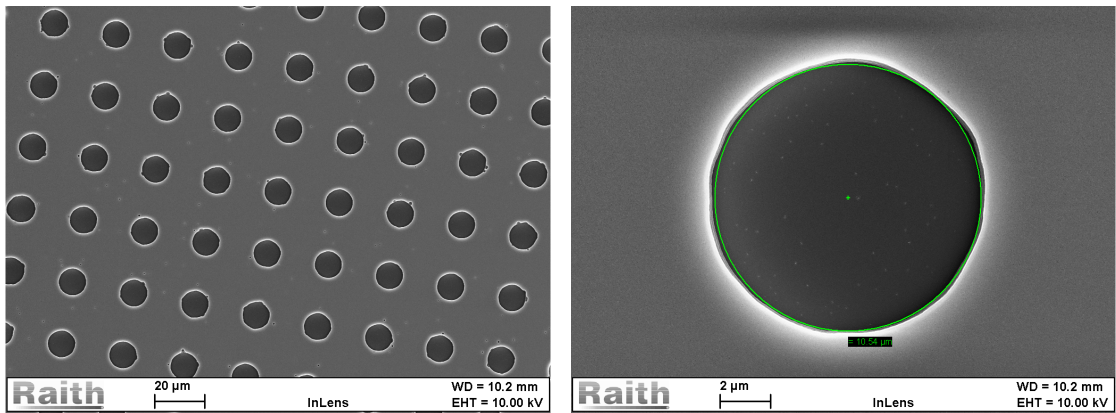

(c) Overview of circles with target pitch value 25 µm.

(d) Close-up of circle with target diameter 10 µm.

Figure 5.6: Pictures of new resist exposed to squares and circles with target diameter 10 µm and pitch value 25 µm.

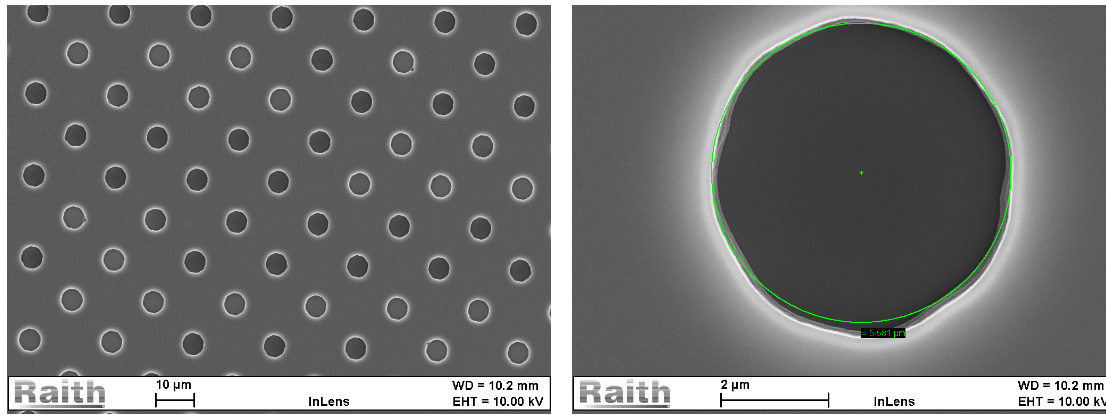

(a) Overview of the periodicity for the circular wells of pitch 15 µm and diameter 5 µm.

(b) Close-up of one circle with target diameter of 5 µm.

Figure 5.7: Overview and close-up of circular wells with pitch 15 µm and diameter 5 µm on SiN.

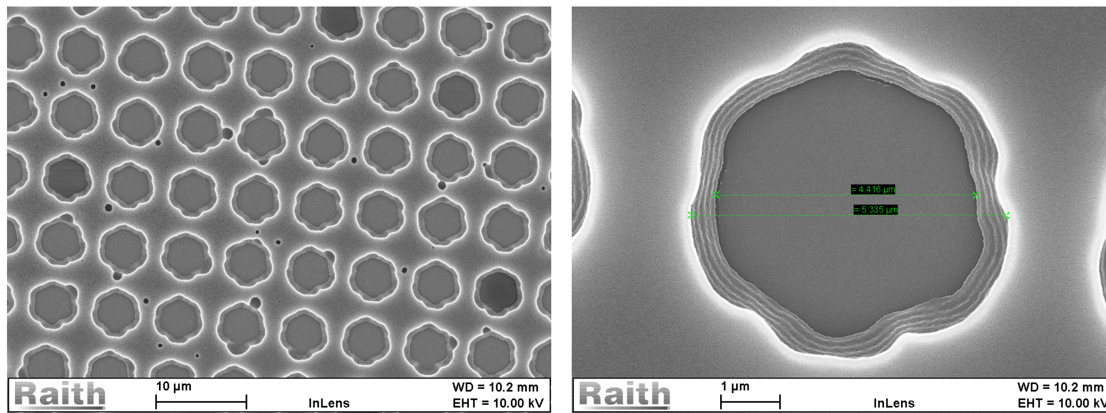

(a) Overview of the periodicity for the circular wells of pitch 7 µm and diameter 5 µm.

(b) Close-up of one circle with target diameter of 5 µm.

Figure 5.8: Overview and close-up of circular wells with pitch 7 µm and diameter 5 µm on SiN.

5.2.2 Sapphire Structuring

Once the structuring has been optimized on Si + Si_3N_4, the procedure is very similar for sapphire, allowing for more advanced structuring of sapphire. A demand for the optical windows is that they are both thermal and mechanically durable. Using sapphire is therefore a brilliant choice of material, being one of the hardest materials in the world, with a Young's Modulus of ∼465 GPa, double that of steel.[70]

In this work two ways of structuring sapphire has been explored; generating hills of sapphire by aluminium deposition and solid-state conversion, and etching patterns into the sapphire using a structured etchant mask. When structuring using sapphire and not some other material one will maintain the optical transparent properties of sapphire, while simultaneously obtaining an increased surface roughness.

Structuring by Solid-State Conversion

The structuring on sapphire is conducted after completing the photolithographic procedure described in Section 4.2 and 5.2. As detailed in Section 4.3 the remaining photoresist is first overexposed for 3 minutes. About 100-200 nanometers of aluminium is then deposited using the Temescal. Following the lift-off procedure one is left with aluminium structures on the surface.

Upon metal deposition one has to be aware of resist- and metal thickness. Should the resist be thinner than deposited metal one will obtain bonding between the metal in contact with the substrate and the metal in contact with the photoresist. This could either block the developer from reaching the exposed resist, hindering the lift-off procedure, or it could mean that as the aluminium on top of the resist is removed, so is the aluminium in contact with the substrate surface. Seeing that the AR-P was deposited at approximately 1.5 μm thickness, and the aluminium was deposited with a thickness up to 200 nanometers, this was not a problem in this work. The deposition was done at a rate of 3 Å/s.

After obtaining aluminium structures on sapphire, the samples are placed in a furnace for 24 hours at 450°C with a heating rate of 2°C/min and a cooling rate of 5°C/min. This step is an oxidation anneal set to minimize hillock formation. Afterwards a high-temperature heat treatment in the range of 800-1350°C for 1 h is conducted to induce growth of the underlying sapphire crystal to consume the oxide layer, as was first reported by Park et al. (2005).[76] Annealed aluminium pillars can be seen in Figures 5.9 and 5.10 - originally 100 nm Al was deposited. For this work the best results were obtained using a high-temperature heat treatment at 1100°C for 1 hour, which is given in Figure 5.10, as this temperature provided the least hillocks within the interval 1000-1200°C.

J. Biser (2013) explain these hillocks, i.e. small hills, observed in Figures 5.9 and 5.10, by stress and divoting/cavitation in the particles. For a particle with low diameter ($\sim$ 100 nm) and equally low height, it is claimed that the particle is effectively stress free, while a particle of larger diameter will experience a larger compressive stress in the film due to the substrate traction. The effect is claimed to be reduced at higher temperatures as a result of phase transitions and diffusive mobility.[77] It is also believe that the pillars could be hollow. Even though no systematic experiment to investigate this has been conducted, cavities seem to be the case as one may observe in Figure 5.9. Rai et al. (2006) report of two oxidation regimes for aluminium; a slow regime where the primary mechanism of oxidation is the diffusion of oxygen through the oxide shell.[89] The fast regime is above the melting point of aluminium where one obtains diffusion from both aluminium and oxygen, a process which may result in hollow structures. The temperatures used here are above the melting point of aluminium (about 660°C), and it is therefore believed that the cavities originate from this fast oxidation regime. A possible solution to this problem would be to adjust the heating and cooling rate during the annealing process for the second heat treatment. When the heating and cooling rates are too high the structures do not have time to reach equilibrium, increasing the hillocking and cavitation. The heating and cooling rates, in addition to the annealing time, should therefore be optimized in the future.

Both Biser and Rai et al. (2006) work with particles smaller than what is reported here, and it is particularly the size of their particle which is the reason for them not to increase the temperature, as it would render them discernible.[89] This

further supports the need for annealing optimization at the particle sizes used here. A problem could be to observe whether the particles are hollow or not, seeing that this will not be observable by either SEM or AFM, unless the caps fall off, as was the case for Figure 5.9. One possible solution could be to investigate the mass-thickness contrast obtained from bright field transmission electron microscopy, seeing that the density would be reduced, and thus the signal increased, if the particles are hollow.

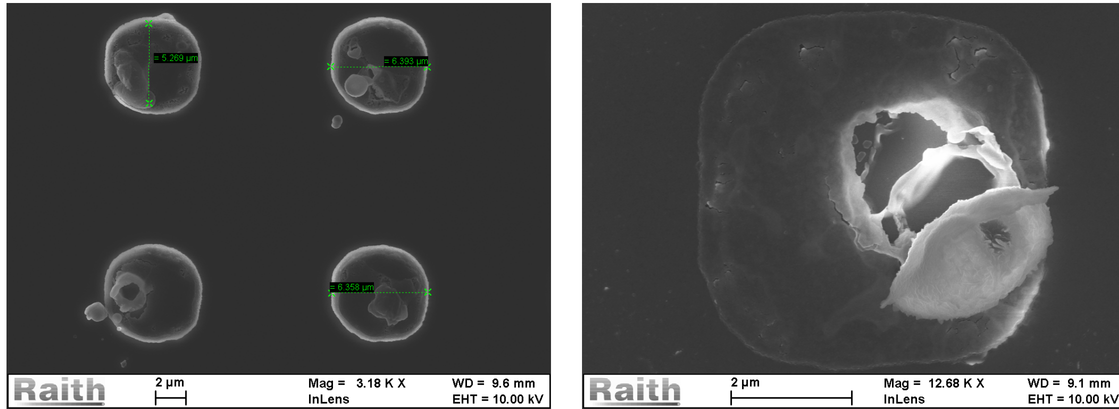

(a) SEM image of converted aluminium structures on sapphire samples after annealing at 1050°C.

(b) SEM image of defect, converted aluminium structure on sapphire samples after annealing at 1000°C.

Figure 5.9: SEM showing two annealed sapphire samples that have been heated to 1050 and 1000°C, respectively. Both samples indicate what looks like cavities in the pillars.

Figure 5.10a shows the SEM image of the sample annealed at 1100°C. The signal of backscattered and secondary electrons are mainly influenced by the topographical changes in the sample. Knowing this one can say that Figure 5.10a indicates a flat center of the sample, with some topographical change along the edge of the structure - the part of increased brightness. But it is not possible to determine the height profile of this topographical change. To investigate this further an AFM-scan of the sample was conducted (Figure 5.10b). It is evident that there is a topographical elevation along the edge of the cylinders, but much greater than the thickness of deposited metal. This topographical elevation along the edge is so large that it is challenging for an AFM to measure properly with a regular tip. Consequently the resulting image has some artefacts, as can be seen in Figure 5.10b. This scan is conducted from right to left, making the artefacts most visible on the left side of the topographical changes.

Looking at Figure 5.10 it is clear that there are some minor topographical changes of approximately 50-100 nm height on the structure. These could be microcrystallites of sapphire, i.e. small sapphire crystals, obtained by annealing the aluminium. Following the line profile given in Figure 5.10c it is evident that the central thickness is approximately 200 nm, which is not consistent with the deposited aluminium thickness (which was 100 nm). This could indicate some cavitation. Additionally one may notice that the outer rim is much higher than the expected height. Unlike Park et al. (2005) this cannot be explained by the angle of deposition, as the Temescal has a perpendicular deposition.[76] This could be explained by the photoresist development generating positive-sloped walls, as was most evident in Figure

Figure 5.4, 5.5 and 5.8. With positive walls one can expect that a perpendicular deposition of aluminium would build up along the wall, and if this build-up is not removed during lift-off one may observe tall rims (see schematic in Figure 5.11). Whether or not the rims have an angle outwards, as indicated in the schematic, is hard to say using AFM and perpendicular SEM imaging, as these methods does not allow for the necessary incident angle to view this. 45° or 90° tilted SEM imaging can be used to investigate this in detail, should it be a continuous problem. A solution to the problem is to use photoresists which generate straight or slight undercut walls.

Work remains to be done with regards to characterization of these pillars after annealing. One have to decide whether the whole pillar has converted to sapphire, or if some aluminium still remains. Park et al. checked this using electron backscatter diffraction (EBSD) and analysis of the Kikuchi lines, and making sure the penetration depth was lower than the height of the pillars. An alternative method could be a SEM combined with a x-ray spectrometer (EDS) which in turn also could be combined with a Raman spectrometer.

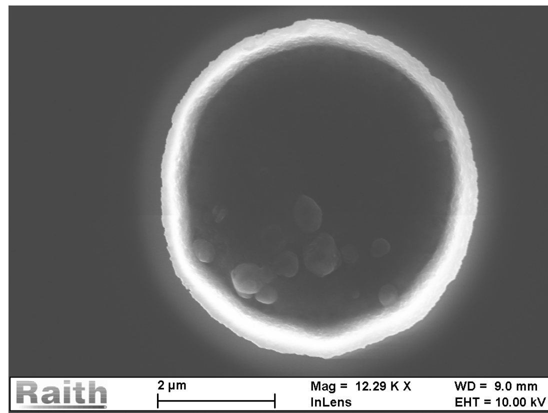

(a) SEM image of sapphire structure (annealed aluminium) on sapphire.

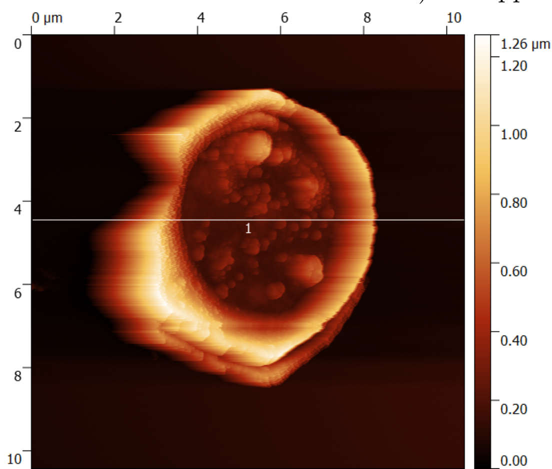

(b) 10 µm x 10 µm scan using AFM of sapphire structure (annealed aluminium). Image obtained using Gwyddion (a free and open source software).

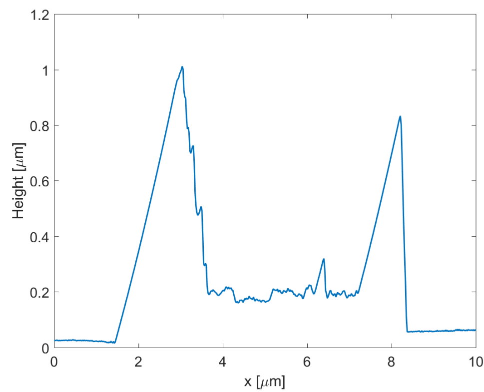

(c) Line-profile of the white line labelled as "1" in (b). Obtained using Gwyddion (a free and open source software).

Figure 5.10: Close-up of what is believed to be sapphire structures after heating aluminium at 1100°C for 1 hour. Obtained using SEM at the UiB NanoLab and AFM at Zernike, Groningen. Note that the two images are not from the same pillar, as it is not possible to find the same pillar without any labeling.

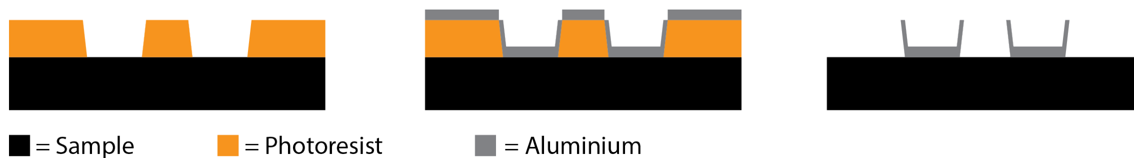

Figure 5.11: Schematic suggesting how the sapphire rim structures are generated, from developed photoresist to final structures.

Structuring in Sapphire by Selective Etching

An alternative to generating sapphire pillars on the substrate is to selectively remove parts of the material by the etching procedure detailed in Chapter 4. First one deposits a protective coating of silicon dioxide on the sample, followed by the AR-P 3540 procedure. At this moment one has obtained well structures which by a RIE procedure will transfer the well structures into the SiO_2. The RIE is conducted by exposing the sample to 15 sccm flow of CHF_3 at 7 mTorr pressure with a 100 W radio frequency power (RF power) for 5 minutes. The AR-P functions as a protective layer for the remaining SiO_2 and is therefore removed after the first RIE by a 3 minutes exposure and 2 minutes development. The AR-P would be dissolved in the wet etch, but to ensure less contamination of the etch, the removal is conducted by development before wet-etching is initiated. The chemical etch (wet-etch) is then conducted, with remaining SiO_2 as a protective layer. This is done in a solution of 3:1 sulfuric acid (96% concentration) to phosphoric acid which is heated at temperatures between 200-280°C. The procedure then has to be optimized for the chosen temperature. A 3:1 ratio of acids provides the highest etching rate of the sapphire (0001) planes at 280°C, approximately 9 μm/h.[78] The crystal wet etching process depends on parameters such as the etchant temperature, time, etchant concentration and H_2SO_4:H_3PO_4-ratio.[79]After etching one is left with cavities in the sapphire having the original well shape, but which penetrates the sample along the crystal planes with highest etch resistance - this is called an etch pit. These pits usually begins at the most active points of the material, such as places where dislocations reach the surface. Thus the defect density can be observed by the density of such pits, and the crystal symmetry can be analysed by the symmetry of the etch pit.[70]

SEM images of a sapphire sample etched at 230±3°C for 15 minutes is provided in Figure 5.12. Notably the temperature is lower than 280°C, which influences the result thereafter with a lower etching rate. This is why several smaller triangles are seen, as it is believed that the obtained result is an early stage of the etch procedure. The small triangles, or etch pits, begins at the dislocations in the material. The etching rate is highest at the (0001)-plane, the C-plane, of the sapphire crystal. As the samples used consist of (0001) surfaces etching will first happen perpendicular to the surface. After some time the more etch-resistant planes will appear. The triangular shape can be attributed to three opposing planes of the $\{1\bar{1}0l\}$ family, e.g. $(01\bar{1}l)$, $(1\bar{1}0l)$ and $(\bar{1}01l)$.[79] The l-value depends on the angle at which these three planes meet, which is also why it is not given before one is able to measure it using for example a profilometer.

Increasing the etching time to 25 minutes with 230±3°C resulted in the structures given in Figure 5.13. In Figure 5.13b the crystal planes are much more prominent than that of Figure 5.12b. The darker center is likely to be the c-plane. Aota et al. (2014) showed that the insoluble product of the reaction between sapphire and sulfuric acid, $Al_2(SO_4)_3 \cdot 3H_2O$ (see Equation 5.1) would limit the width of the structures.[80] This is due to the impurities, here $Al_2(SO_4)_3 \cdot 3H_2O$, attaching to the step edges, i.e. atomic structures in the crystal, which are energetically unstable. This adhesion then inhibits the reaction of step edges with the etchant, which is what drives the etching laterally. One can in other words adjust the width of etch pits by the mixing ratio of H_2SO_4 and H_3PO_4 in the solution. Additionally increasing the temperature would increase the depth of the structures, allowing for a highly modifiable result.[80]

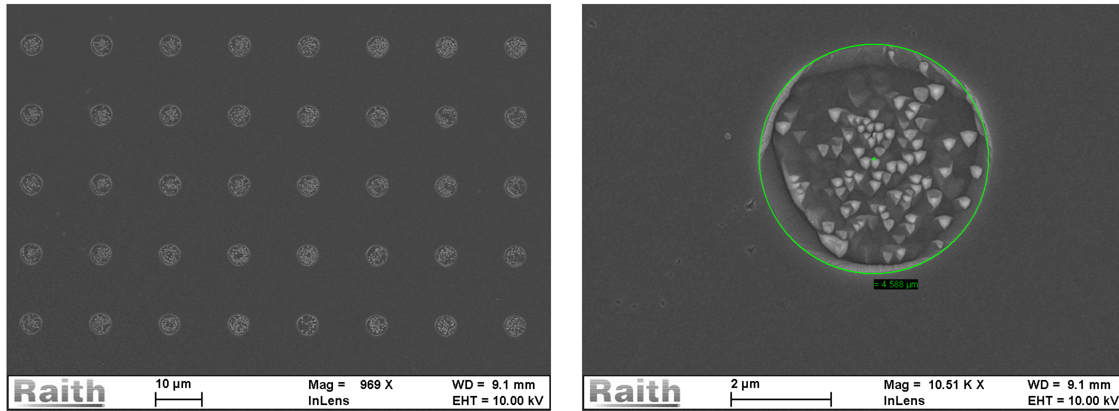

(a) Overview SEM image of etched sapphire sample.

(b) Close-up SEM image of etched sapphire sample

Figure 5.12: Structured sapphire sample which have been in a H_2SO_4 3:1 H_3PO_4 mixture heated to 230±3°C for 15 minutes.

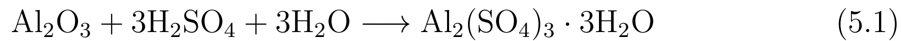

$$Al_2O_3 + 3H_2SO_4 + 3H_2O \longrightarrow Al_2(SO_4)_3 \cdot 3H_2O \tag{5.1}$$

The reaction of phosphoric acid with sapphire is given as follows:

$$Al_2O_3 + 6H_3PO4 \longrightarrow 2Al(H_2PO_4)_3 + 3H_2O \tag{5.2a}$$

$$Al_2O_3 + Al(H_2PO_4)_3 \longrightarrow 3AlPO_4 + 3H_2O \tag{5.2b}$$

where the reaction product $AlPO_4$ is known to be soluble in phosphoric acid.[80]

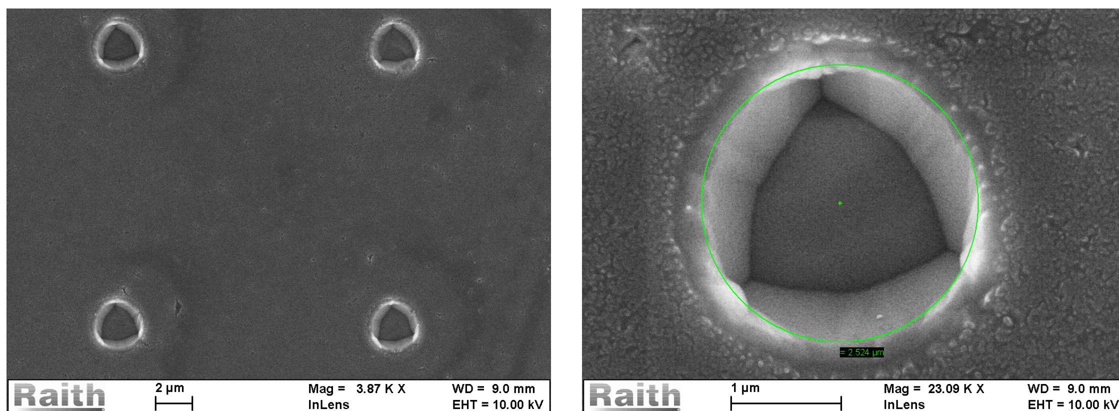

(a) Overview SEM image of etched sapphire sample.

(b) Close-up SEM image of etched sapphire sample

Figure 5.13: Structured sapphire sample which have been in a H_2SO_4 3:1 H_3PO_4 mixture heated at 230°C for 25 minutes. The diameter of the circles is approximately 2.5 µm.

A proper review of the safety regarding this procedure should be conducted. Sulfuric acid has a boiling point of ~ 290°C and phosphoric acid 158°C, according to Sigma-Aldrich's product descriptions. The temperatures used in this wet etch are usually above 200°C which is close to, or above, the boiling point of sulfuric acid and phosphoric acid. Sulfuric and phosphoric acid vapor could therefore be one of the many dangerous aspects to consider during this wet etch.

5.2.3 SU-8 Optimization

SU-8 was used to generate pillars on the surface which in turn will reduce the solid-liquid interface area, f_{sl}, upon Cassie-Baxter wetting, possibly allowing for hydrophobic wetting properties. This can be used in environments of low humidity, allowing for self-removal of water droplets. Here the structuring of SU-8 with varying pitch value and pillar width is presented, opening up for future systematic studies on the influence of pillar size and pitch value on the wetting properties of the sample.

Seeing that SU-8 is a negative photoresist, there are other indications of under- and overexposure for SU-8 as compared to for example AR-P 3540. The structures will be inverted as compared to those obtained from AR-P 3540 using the same photomask. When a negative photoresist is overexposed more polymerization will happen during PEB, which eventually could make the resist end up as a thick layer which is not possible to remove from the substrate. When a negative photoresist is underexposed there will be less polymerization and thus more resist will be soluble in developer, resulting in smaller structures on the substrate - potentially removing all of the deposited photoresist. Using the same mask as for AR-P, SU-8 will result in stand-alone pillars, i.e. pillars that are solely bound to the surface. If the pillars have a low adhesion to the surface, they will also be easier to remove, seeing that the resist-substrate contact area is much lower for than for a positive resist where most of the resist remains after development (assuming the spacing between structures is greater than the size of structures).

As most of the work on SU-8 exposure was conducted at the BBB, the optimization also happened there. Using the built in microscope of the MJB4 mask aligner, optical microscopy images were not taken during optimization. Therefore the only recorded images are using the SEM at the NanoLab after development of samples that looked close to good enough in the optical microscope at BBB. The first samples returned ended up being exposed too long, which allowed for a closer study of overexposure and what it might look like. These are given in Figure 5.14.

Figure 5.14a was exposed for 8 seconds, which turned out to be approximately twice the desired dose. This is evident from the images as well, as one can see that most of the resist is still present on the substrate. The small lines observed are indications of resist which with lower exposure dose would be removed, but which were not as a result of being an overexposed negative resist. When SU-8 is exposed to UV-light a strong acid is generated which functions as a catalyst for the thermally driven cross-linkage happening during post exposure bake (PEB). It is believed that more of this acid is produced during extended periods of exposure, allowing for more cross-linkage, making more of the resist insoluble, also those areas which were not exposed originally. This effect is noticeable for all samples given in Figure 5.14, and which is one of the most notable indications of overexposure.

It is likely that underexposure of a sample would result in insufficient cross-linkage, allowing for most of the resist to be removed, also what was exposed. For an underexposed sample the penetration depth of the generated acid through the resist might be insufficient. Seeing that it is this acid which contributes to the cross-linkage during annealing one might end up with soluble resist at the substrate-resist interface. Consequently all of the deposited resist could be removed during development for underexposed structures, leaving the sample blank. This effect was observed for several experiments during optimization. Blank surfaces after development could in other words be indicative of low exposure times.

Optimization of the developing time was not conducted as good results were obtained using the developing time given in the data sheet; 60 seconds. Similarly the PEB times and temperatures were not modified and kept at what was given in Section 4.2.5, first 60 seconds at 65°C followed by 60 seconds at 95°C.

It should be noted that for samples made of glass (sapphire) the exposure dose was given to be 1.5 times larger than for silicon, as was stated by MicroChem in the data sheet.[61] This is likely to originate from the lack of reflectance for glass as compared to silicon. In Appendix B the influence of reflectance on the lights energy and intensity distribution through the resist is detailed. Without the reflected light wave the energy will necessarily be lower, but one will also reduce the interference effects.

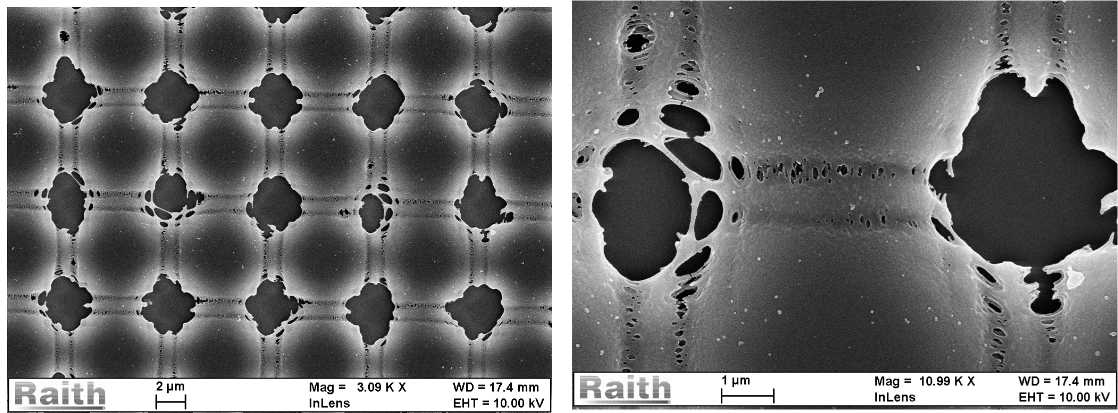

(a) Overview of SU-8 sample exposed for 8 seconds.

(b) Close-up of SU-8 sample exposed for 8 seconds.

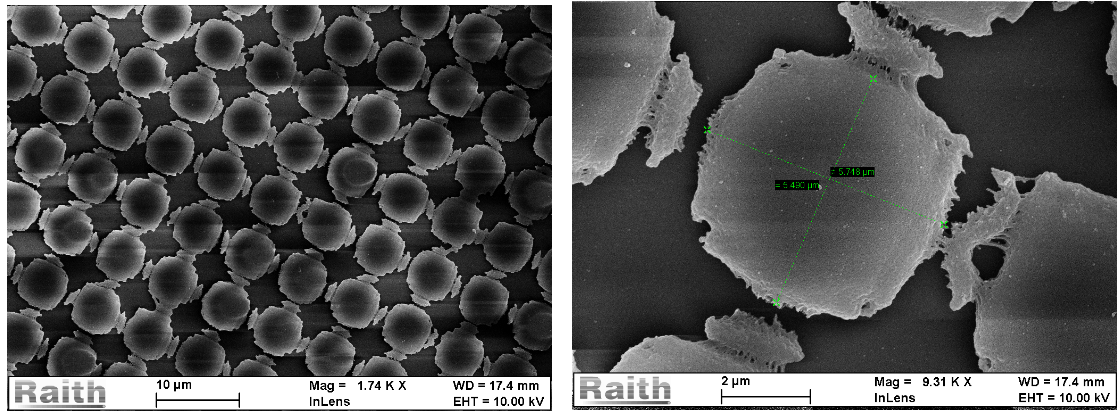

(c) Overview of sample exposed for 5 seconds.

(d) Close-up of sample with target size 5 µm and pitch 7 µm, exposed for 5 seconds.

Figure 5.14: Overview and close-up of overexposed resist with pitch 7 µm structures. It is noticeable that this is less exposed than the previous samples, being closer to the optimal result, yet some effect of overexposure is visible.

Having inhomogeneous resist deposition is not necessarily a problem during photolithographic optimization. Should one be certain that one has thicker resist closer to the edges or corners than in the center of the sample, this can be exploited to get an indication of over- or underexposure. After development of the sample one can inspect both the edges of the structure and the center. Should the center structures be overexposed whilst the edge structures look good, the exposure is set too high, if

the target thickness is found in the center (as the thickness is greater at the edges than the center). Similarly, if the edge structures are slightly underexposed, and the center structures are slightly overexposed, one would be able to find some structures that are close to optimal when looking over the thickness gradient in the sample, i.e. when moving from the center to the edge structures. And by slightly decreasing the exposure one would be at the target dose.

The optimized structures of SU-8 on Si + Si_3N_4 are given in Figures 5.15 through 5.17. When looking closer at the 25 μm pitch structures, i.e. Figure 5.15, it is evident that the squares are overexposed. One should therefore reduce the exposure time by 0.1 seconds, as for the structures given in Figure 5.16. It is evident from the close-up (Figure 5.15d) that the sides are wider than 10 μm, while the corners have not yet reached the point of which would be expected of a 10 μm sided square. This is believed to be caused by the acid generated during exposure which results in what one could call a proximity effect, similar to that of which is observed for electron-beam lithography.

The smaller structures with 15 μm pitch were exposed for 0.1 seconds less than the 25 μm ones, i.e. 3.0 seconds instead of 3.1. This is believed to be the optimal exposure time, as the structural width is < 200 nm from the target size. The most noticeable of the remaining pictures are the degree of impurities on the sample. As all samples were exposed at the BBB, they could partially be explained by the lack of cleanroom facilities there. An other possibility is that these particles are residues from the photolithographic procedure.

For the 7 μm pitch hexagonal structures the separation is too small. Seeing that the height from top to bottom of one structure should be 5.77 μm (from Chapter 4) the resulting vertical separation is 1.23 μm which evidently is too short. In Figure 5.17c it is evident that every hexagon is connected to both neighboring hexagons in the vertical direction, while they are not connected in the horizontal direction. When reducing the exposure time with 0.1-0.2 seconds, this effect is reduced.

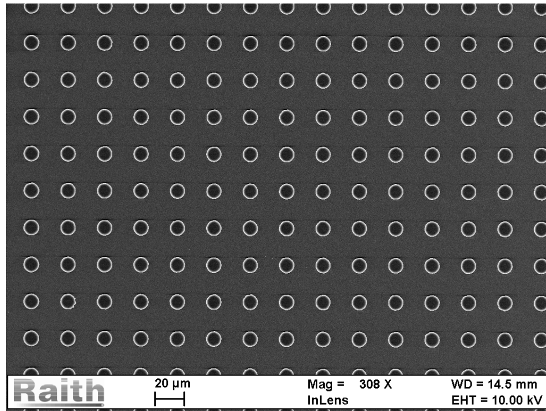

(a) Overview of SU-8 sample with circles of target pitch value 25 µm.

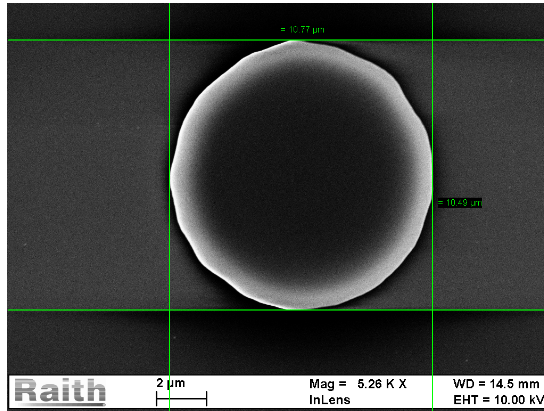

(b) Close-up of SU-8 sample with circles of target pitch value 25 µm and diameter 10 µm.

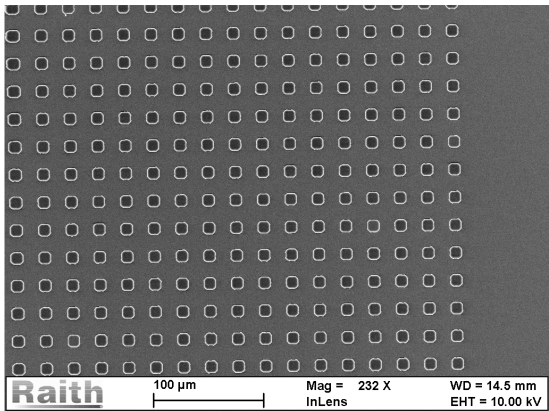

(c) Overview of SU-8 sample with squares of target pitch value 25 µm and side length 10 µm.

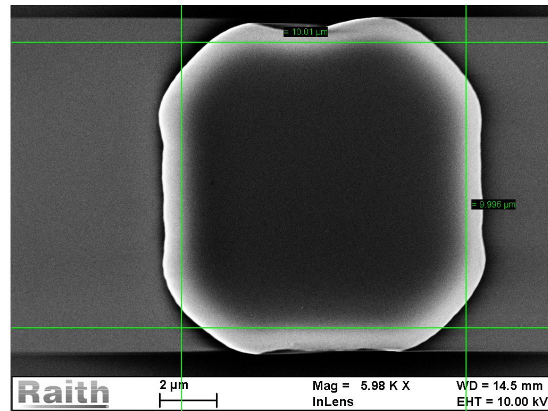

(d) Close-up of SU-8 sample with squares of target pitch value 25 µm and side length 10 µm.

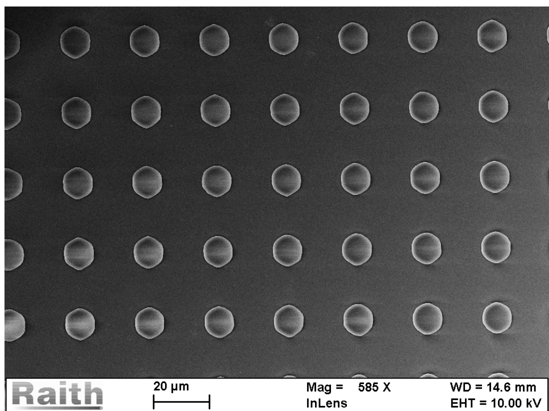

(e) Overview of SU-8 sample with hexagons of target pitch value 25 µm and side length, X = 10 µm.

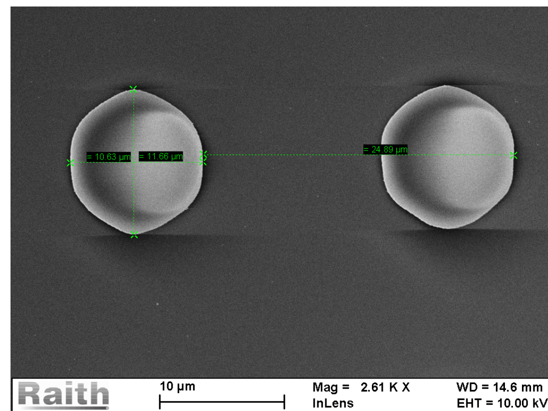

(f) Close-up of SU-8 sample with hexagons of target pitch value 25 µm and side length, X = 10 µm.

Figure 5.15: Overview and close-up of SU-8 exposed with circles, squares and hexagons of target pitch value 25 µm and side length, X = 10 µm. Exposed for 3.1 seconds and developed for a total of 68 seconds.

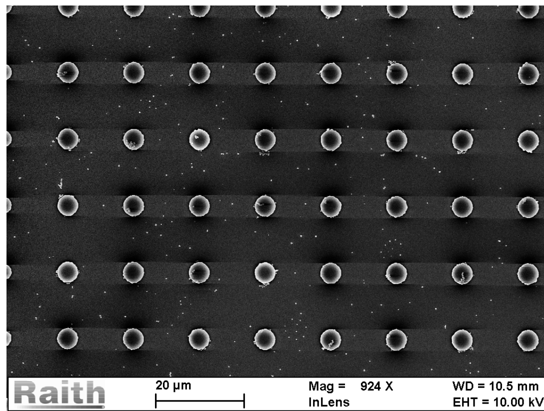

(a) Overview of SU-8 sample with circles of target pitch value 15 µm.

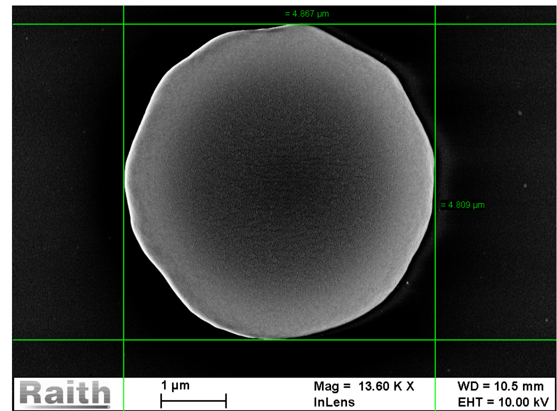

(b) Close-up of SU-8 sample with circles of target pitch value 15 µm and diameter 5 µm.

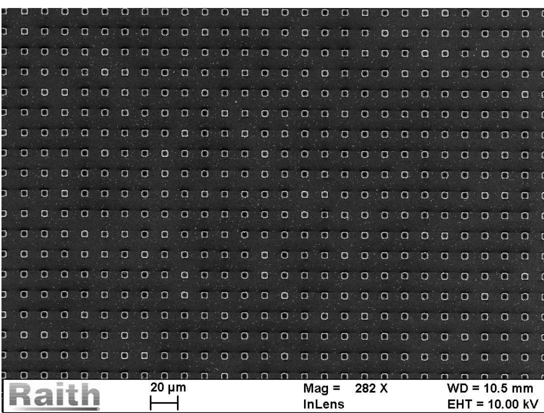

(c) Overview of SU-8 sample with squares of target pitch value 15 µm and side length 5 µm.

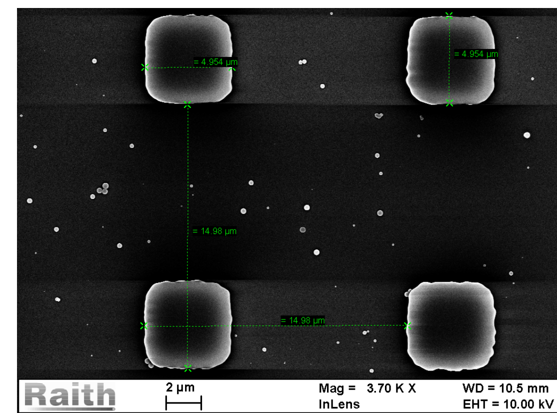

(d) Close-up of SU-8 sample with squares of target pitch value 15 µm and side length 5 µm.

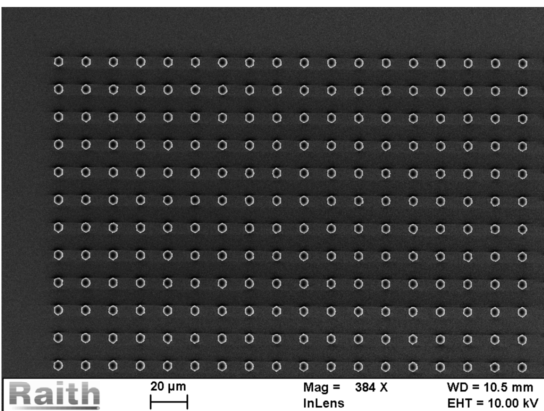

(e) Overview of SU-8 sample with hexagons of target pitch value 15 µm and side length, X = 5 µm.

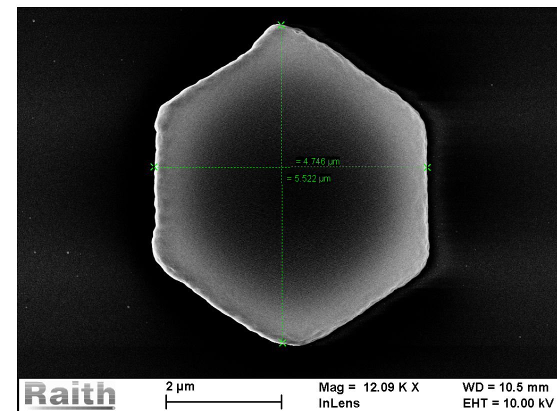

(f) Close-up of SU-8 sample with hexagons of target pitch value 15 µm and side length, X = 5 µm.

Figure 5.16: Overview and close-up of SU-8 exposed with circles, squares and hexagons of target pitch value 15 µm and side length, X = 5 µm. Exposed for 3.0 seconds and developed for a total of 65 seconds.

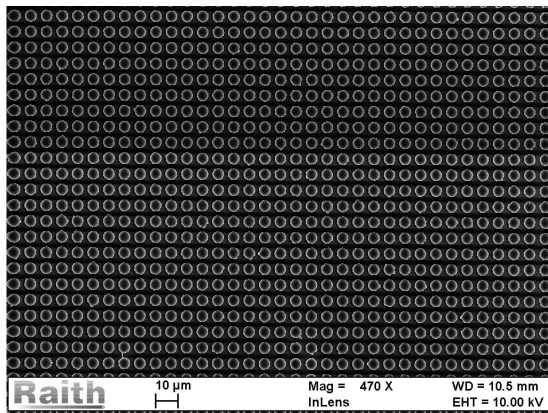

(a) Overview of SU-8 sample with circles of target pitch value 7 µm and side length 5 µm.

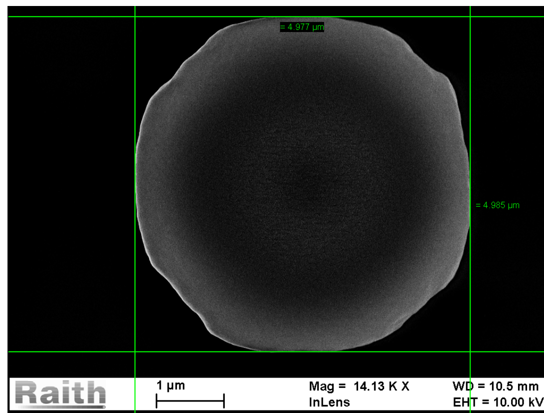

(b) Close-up of SU-8 sample with circles of target pitch value 7 µm and side length 5 µm.

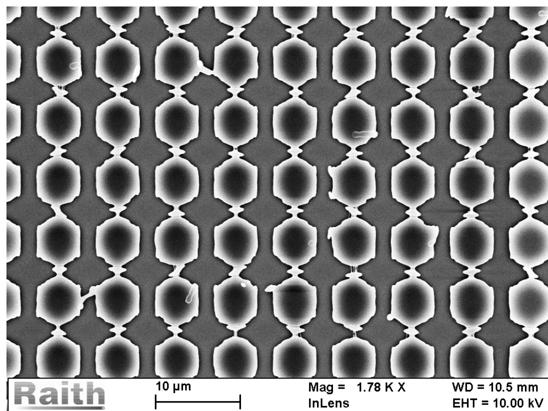

(c) Overview of SU-8 sample with hexagons of target pitch value 7 µm and side length, X = 5 µm.

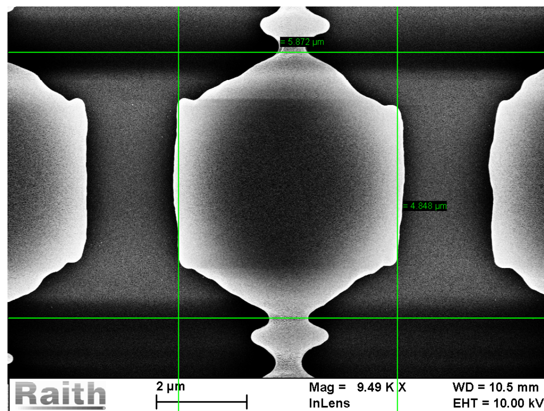

(d) Close-up of SU-8 sample with hexagons of target pitch value 7 µm and side length, X = 5 µm.

Figure 5.17: Overview and close-up of SU-8 exposed with circles and hexagons of target pitch value 7 µm and side length, X = 5 µm. Exposed for 3.0 seconds and developed for a total of 65 seconds.

5.3 Contact Angle Measurements

A characterization of the structured surfaces described in Section 5.2.2 and Section 5.2.3 was conducted using contact angle measurements. The results are reported in the following subsections.

5.3.1 Structured Sapphire

The wetting properties of structured sapphire surfaces produced with solid-state conversion and etching were measured (see Table 5.4). Images of the droplets are given in Figure 5.18. Two samples are presented here, both with pitch = 15 μm. The solid state conversion sample deposited with annealed aluminium structures is given in Figure 5.18a (water in air) and Figure 5.18b (oil in water). The sample selectively etched is given in Figure 5.18c (water in air) and Figure 5.18d (oil in water).

From Table 5.4 it is evident that the measured contact angle for water in air is higher than the flat and expected value for both surfaces. This is believed to be caused by some contamination layer present on the surfaces during measurement, as the samples were not RCA-cleaned after structuring.

The oil in water measurements for etched sapphire were consistent with theory. It is not possible to determine whether the etched sample is in the Cassie-Baxter or the Wenzel state, judging by the static contact angle, and this could be further investigated using contact angle hysteresis measurements. The oil in water contact angles for the annealed sapphire is measured above the expected Wenzel wetting contact angle, and below the Cassie-Baxter. This could be explained by the increased roughness from the microcrystallites observed in Figure 5.10 which would increase R_f and the expected Wenzel contact angle. Another possible explanation is the partial penetration of oil into the water pockets of the Cassie-Baxter state, which is believed to result in a contact angle lower than the expected Cassie-Baxter value, and higher than the expected Wenzel value.

In general these values are not significantly different from those reported in Figure 5.1 for the unstructured sapphire surfaces, but it is believed that the oleophobic properties as a function of time when submerged in water are strongly improved. Work is currently being conducted in our group to investigate how long these structured sapphire substrates are oleophobic when submerged under water as compared to the unstructured ones, but that will not be reported in this thesis.

One could manipulate the aspect ratio of sapphire etch pits by performing deep-etch. Some work is currently being conducted on this in our group. This could be done by deep reactive-ion etching, or manipulating the etching conditions for wet etch such as sulfuric acid to phosphoric acid ratio, etching time and temperature.[80] A more systematic study on the influence of geometrical factors on wetting is investigated in the following subsection.

Table 5.4: Measured contact angle on unstructured RCA-cleaned (Flat) sapphire surfaces (from Figure 5.1) and structured sapphire (Meas), both etched and with annealed aluminium structures for water in air (WiA) and oil in water (OiW), compared to the expected contact angle for Wenzel (W) wetting, hemi-wicking (HW) wetting and Cassie-Baxter (CB) wetting. The expected contact angles were calculated using Equation (2.8) ((2.19c) for OiW), (2.15) and (2.20), respectively, with the flat contact angle as θ. Pitch value is 15 µm for both samples, and R_f and f_{sl} is calculated using 5 µm wide and 0.2 µm tall structures.

	Flat [°]	Meas [°]	f_{sl}	R_f	W [°]	HW [°]	CB [°]
Etched WiA	18 ± 2	33 ± 2	0.913	1.014	15 ± 3	17 ± 2	N/A
Etched OiW	135 ± 2	139 ± 2	0.913	1.014	136 ± 2	N/A	137 ± 2
Annealed WiA	16 ± 2	37 ± 3	0.087	1.014	13 ± 3	5 ± 1	N/A
Annealed OiW	142 ± 2	153 ± 3	0.087	1.014	143 ± 2	N/A	169 ± 1

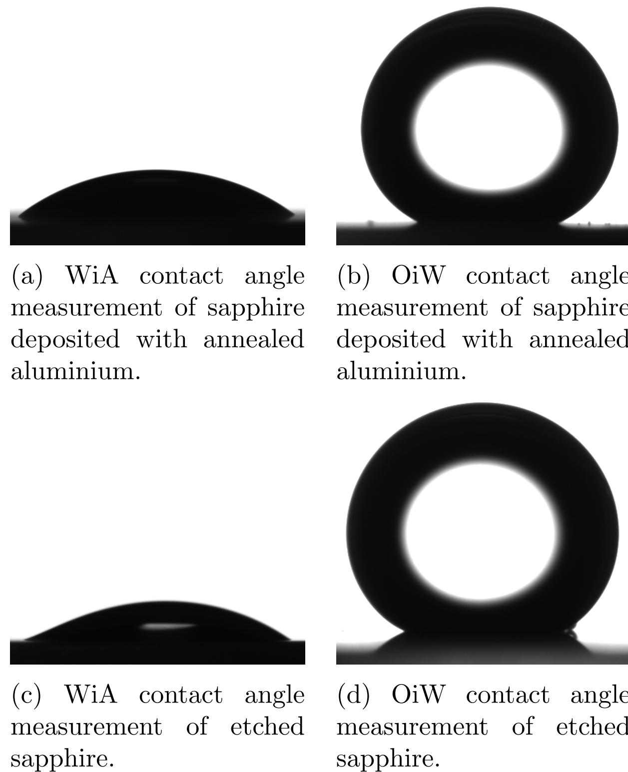

(a) WiA contact angle measurement of sapphire deposited with annealed aluminium.

(b) OiW contact angle measurement of sapphire deposited with annealed aluminium.

(c) WiA contact angle measurement of etched sapphire.

(d) OiW contact angle measurement of etched sapphire.

Figure 5.18: Water in air (WiA) and oil in water (OiW) contact angle measurements of etched and annealed sapphire substrates, described in Section 5.2.2. Both with pitch value 15 µm.

5.3.2 SU-8 Structures of Varying Geometry

Table 5.5 gives the resulting contact angles measured for structured SU-8 on Si with Si_3N_4, and Table 5.6 and 5.7 gives the expected contact angle values for Wenzel and Cassie-Baxter wetting, respectively. The expected values are calculated with the assumption that the contact angle of the unstructured (flat) surface is $88 \pm 2°$ (ref. Table 5.5). Images of the water droplets resting on the structured surfaces are given in Figure 5.19, 5.20 and 5.21.

The samples were coated with AuPd to obtain a conducting layer for SEM imaging. Unlike the regular chromium layer, AuPd is not easily removable. Therefore the contact angles measured are all with a layer of AuPd. This does not mean that one is unable to characterize how the wetting properties change with structuring as one can compare the structured surfaces to the flat contact angle, $88 \pm 2°$ in this case. It is important to note that when calculating the expected CB and Wenzel contact angles the expected size of the structures are used, not those reported in Section 5.2.3.

The structures with 15 μm pitch were very non-wetting at the start of measurements, meaning that the droplet had a higher adhesion to the syringe than the surface, making droplet deposition challenging. It was observed that the structures had contact angle $> 140°$, but that it quickly transitioned to a lower contact angle (the one reported in Table 5.5). This could indicate a transition from the Cassie-Baxter wetting state to some partial penetration state, as was also mentioned in the previous section.

For all three structures we see that the values are closer to the Wenzel wetting state than the Cassie-Baxter wetting state, with the exception of the smallest pitch values (and the 15 μm ones before transitioning) which fits well with the Cassie-Baxter wetting values. The higher pitch values result in a larger spacing between the structures, reducing the probability of having air pockets between the water droplet and the surface, which is why we see a transition from Cassie-Baxter to Wenzel at these parameters. At which angle this transition from CB to Wenzel happens depends on the surface features, as is evident from Equation (2.13), which is why one should have the same surface geometry and size to make it comparable. Judging by the quick transition observed for the pitch = 15 μm structures, it is believed that for structures of 5 μm size and ~ 1.5 μm height one can expect the transition for pitch values close to 15 μm.

There is little difference in contact angles with respect to surface feature geometry, i.e. squares, circles or hexagons, with the only exception found for the 7 μm pitch hexagons (Figure 5.21), where it is believed that the vertical linkage between the hexagons observed in Figure 5.17 can explain this deviation.

From Figure 5.19, 5.20 and 5.21 one can see that the expected CB contact angle is highest for the pitch = 15 μm and pitch = 25 μm structures, with the 15 μm having the peak value. This is due to the surface coverage being low compared to the 7 μm structures, making the ratio of solid-liquid interface area, f_{sl}, low as well; $f_{sl} \approx 0.10$ (average from all geometries) for pitch = 15 μm and $f_{sl} \approx 0.14$ for the pitch = 25 μm, as compared to $f_{sl} \approx 0.45$ for pitch = 7 μm.

The error in the expected values for Cassie-Baxter wetting and Wenzel wetting originates from the error at the contact angle measurement of the flat surface ($88 \pm 2°$). Also one have to keep in mind that for the expected CB contact angles one assumes the surface is flat, other than the structuring. Judging by the AFM images

given in Section 5.1 this is evidently not correct, as there are both cracks and terrace structures which would make $R_f > 1$, which by Equation (2.8) would result in a lower θ^* than what is given in Tables 5.6 and 5.7 as $\cos\theta \geq 0$ (from $\theta = 88 \pm 2°$).

A more systematic study on the influence of structure size, pitch value and surface coverage on the wetting properties still remains to be conducted. This work has already been initiated in the group, but will not be part of the work in this thesis.

Optimizing the photolithographic procedure is a highly time-consuming process as it is sensitive to anything from how the sample is placed in the developer to the humidity of the room in which the deposition is conducted. The necessary mapping of the different variables influencing the result, in combination with the relatively limited time available for a master's project, have limited the characterization conducted in this work. There are many interesting aspects to be investigated in detail on this topic in the future, aspects which will be listed in the following chapter.

Table 5.5: Measured contact angles of water in air for structured SU-8, deposited on Si with Si_3N_4, with varying size and pitch (the latter given in brackets). All samples were deposited with AuPd.

	Size (Pitch) μm			
	Unstructured	10 (25) μm	5 (15) μm	5 (7) μm
Unstructured	$\theta^* = 88 \pm 2°$	N/A	N/A	N/A
Squares	N/A	$\theta^* = 91 \pm 2°$	$\theta^* = 98 \pm 2°$	$\theta^* = 116 \pm 5°$
Circles	N/A	$\theta^* = 93 \pm 2°$	$\theta^* = 101 \pm 2°$	$\theta^* = 120 \pm 5°$
Hexagons (SC)	N/A	$\theta^* = 91 \pm 2°$	$\theta^* = 97 \pm 2°$	$\theta^* = 109 \pm 5°$

Table 5.6: Theoretical contact angles of water in air for structured SU-8 assuming Wenzel wetting, height $H = 1.5$ μm and using 88±2° as contact angle for flat surface (Ref. Table 5.5). Calculated using Equation (2.8).

Wenzel wetting	R_f	**Size (Pitch) μm**		
		10 (25) μm	5 (15) μm	5 (7) μm
Squares	$\frac{P^2+4\cdot X\cdot H}{P^2}$	$R_f = 1.096$ $\theta^*_W = 88 \pm 2°$	$R_f \approx 1.133$ $\theta^*_W = 88 \pm 2°$	$R_f \approx 1.612$ $\theta^*_W = 87 \pm 1°$
Circles	$\frac{P^2+\pi\cdot X\cdot H}{P^2}$	$R_f \approx 1.075$ $\theta^*_W = 88 \pm 2°$	$R_f \approx 1.105$ $\theta^*_W = 88 \pm 2°$	$R_f \approx 1.481$ $\theta^*_W = 87 \pm 1°$
Hexagons (SC)	$\frac{P^2+\sqrt{3}\cdot 2\cdot X\cdot H}{P^2}$	$R_f \approx 1.083$ $\theta^*_W = 88 \pm 2°$	$R_f \approx 1.116$ $\theta^*_W = 88 \pm 2°$	$R_f \approx 1.530$ $\theta^*_W = 87 \pm 1°$

Table 5.7: Theoretical contact angles of water in air for structured SU-8 assuming Cassie-Baxter wetting, height $H = 1.5\,\mu m$, $R_f = 1$, and using 88±2° as contact angle for flat surface (Ref. Table 5.5). Calculated using Equation (2.11).

Cassie-Baxter wetting	f_{sl}	**Size (Pitch) µm**		
		10 (25) µm	5 (15) µm	5 (7) µm
Squares	$\frac{X^2}{P^2}$	$f_{sl} = 0.16$ $\theta^*_{CB} = 147 \pm 1°$	$f_{sl} \approx 0.111$ $\theta^*_{CB} = 152 \pm 1°$	$f_{sl} \approx 0.510$ $\theta^*_{CB} = 118 \pm 1°$
Circles	$\frac{\pi \cdot X^2}{4 \cdot P^2}$	$f_{sl} \approx 0.126$ $\theta^*_{CB} = 150 \pm 1°$	$f_{sl} \approx 0.087$ $\theta^*_{CB} = 155 \pm 1°$	$f_{sl} \approx 0.401$ $\theta^*_{CB} = 126 \pm 1°$
Hexagons (SC)	$\frac{\sqrt{3} \cdot X^2}{2 \cdot P^2}$	$f_{sl} \approx 0.139$ $\theta^*_{CB} = 149 \pm 1°$	$f_{sl} \approx 0.096$ $\theta^*_{CB} = 154 \pm 1°$	$f_{sl} \approx 0.442$ $\theta^*_{CB} = 123 \pm 1°$

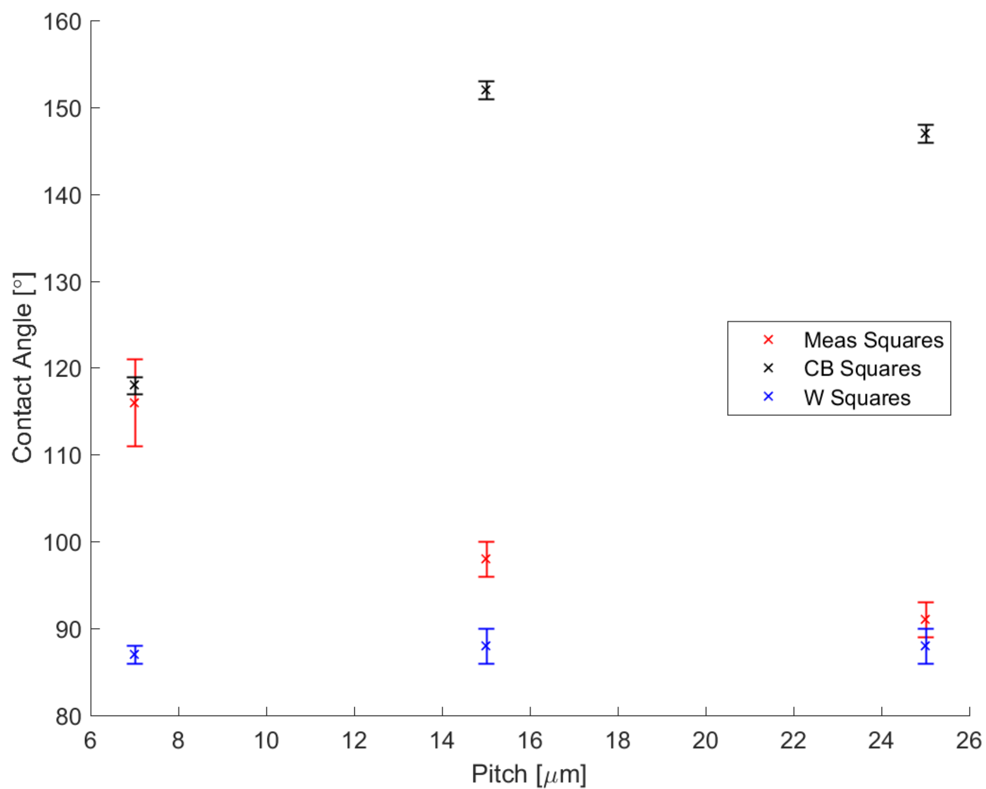

(a) Plot of measured (Meas) contact angle of squares compared to expected values for Cassie-Baxter (CB) and Wenzel (W).

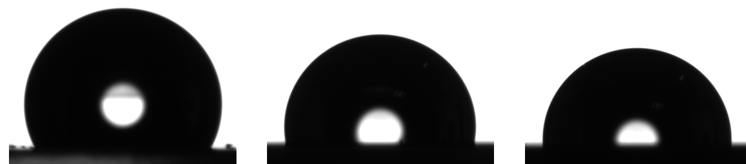

(b) Squares with pitch = 7 µm. (c) Squares with pitch = 15 µm. (d) Squares with pitch = 25 µm.

Figure 5.19: Squares: Graph comparing the measured contact angle of square structures to the expected Cassie-Baxter and Wenzel contact angles with corresponding images showing the water droplet on the structures of (b) pitch = 7 µm, (c) pitch = 15 µm, (d) pitch = 25 µm.

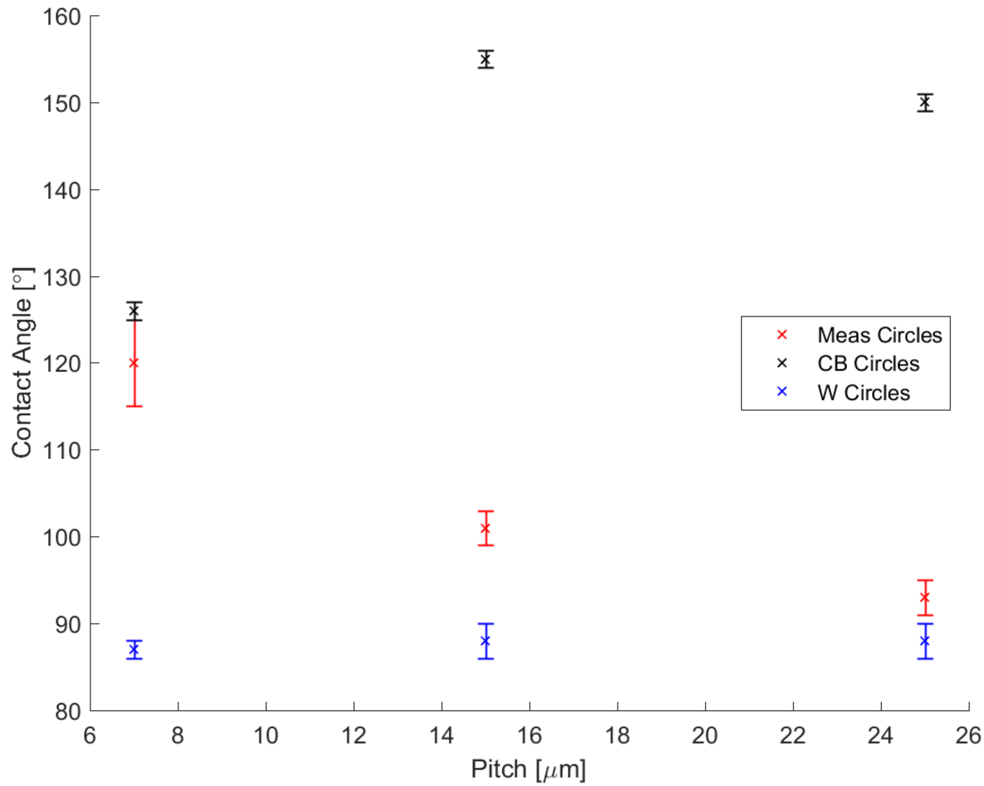

(a) Plot of measured (Meas) contact angle of circles compared to expected values for Cassie-Baxter (CB) and Wenzel (W).

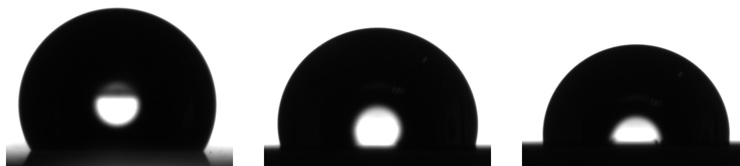

(b) Circles with pitch = 7 µm. (c) Circles with pitch = 15 µm. (d) Circles with pitch = 25 µm.

Figure 5.20: Circles: Graph comparing the measured contact angle of circular structures to the expected Cassie-Baxter and Wenzel contact angles with corresponding images showing the water droplet on the structures of (b) pitch = 7 µm, (c) pitch = 15 µm, (d) pitch = 25 µm.

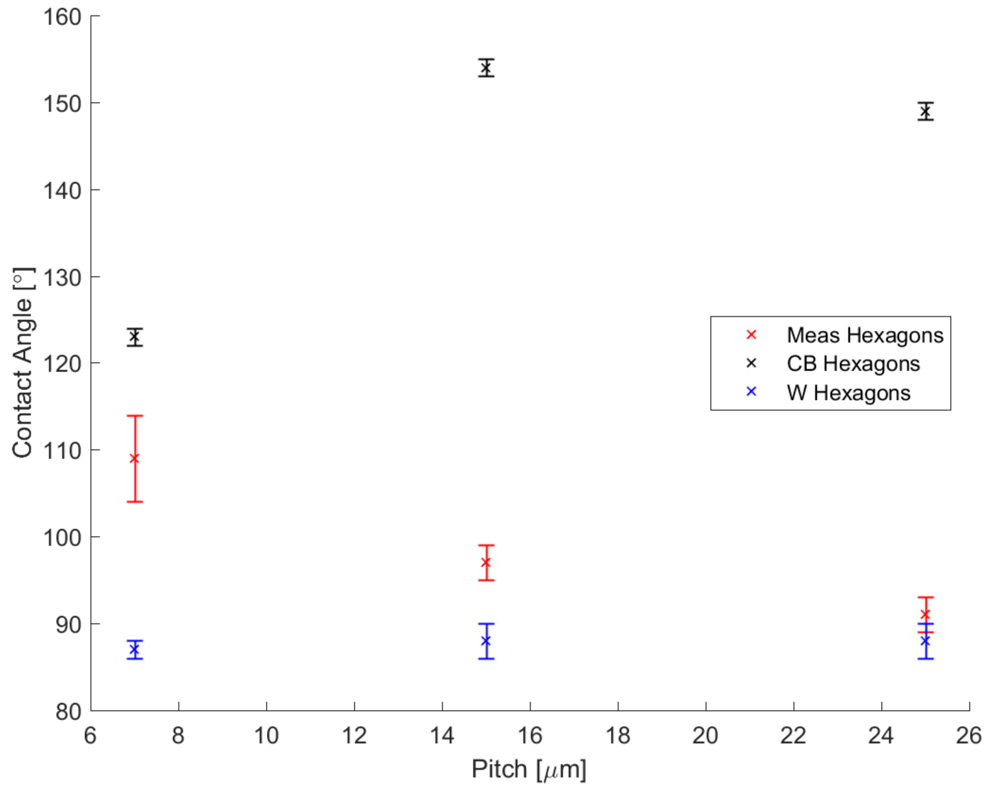

(a) Plot of measured (Meas) contact angle of hexagons compared to expected values for Cassie-Baxter (CB) and Wenzel (W).

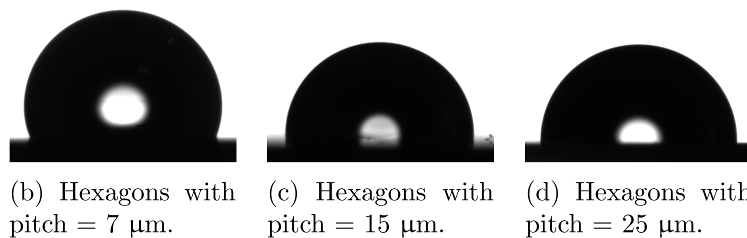

(b) Hexagons with pitch = 7 μm.

(c) Hexagons with pitch = 15 μm.

(d) Hexagons with pitch = 25 μm.

Figure 5.21: Hexagons: Graph comparing the measured contact angle of hexagonal structures to the expected Cassie-Baxter and Wenzel contact angles with corresponding images showing the water droplet on the structures of (b) pitch = 7 μm, (c) pitch = 15 μm, (d) pitch = 25 μm.

Chapter 6

Conclusions and Future Work

The objective of this work has been to design, structure and characterize microstructured sapphire surfaces which could be used in a wide range of applications. Large arrays of squares, circles and hexagons with a size of 5 or 10 μm and a pitch between 7 and 25 μm have been designed. These arrays were then transferred to a light-sensitive photoresist by photolithography. Both positive, i.e. resists that become soluble upon exposure, and negative, i.e. resists that become insoluble upon exposure, were used to create both wells and pillars on the chosen substrate. For the positive resist exposure, the photolithographic setup built in-house at the NanoLab in the Department of Physics and Technology was used. The negative resist exposure was conducted using the MJB4 situated at the Unit for Nano-systems in Biomedicine at the Department of Biomedicine due to limited exposure wavelengths at the setup in the NanoLab. The photolithographic procedure had to be optimized for the structures used here, as the previous work in these nanolabs were using larger structures and thus required lower resolution. AFM imaging was performed at the Zernike Institute in Groningen.

From the optimization procedure it was discovered that the photolithographic procedure is a very delicate procedure sensitive to parameters such as mask-sample contact, sample shape and how the sample is held in developer, to mention some. The most critical parameter for AR-P in this work proved to be the contact between the mask and the resist, as it was more in the soft-contact regime than the hard-contact regime. A way of bringing the mask into hard-contact mode should therefore be investigated for future processing using the same setup, should one desire to create structures of size < 5 μm as the soft-contact proved most challenging at that scale. With the current setup it is very challenging to get a glass-mask into hard contact with the sample. A polyester-based mask could solve this issue, as the setup would allow for this mask to come in vacuum-contact. Some external force on the mask might still be needed to obtain optimal contact.

Following the photolithographic procedure two pathways were followed; for the positive type resist, AR-P 3540, the samples were either deposited with aluminium to generate sapphire through solid-state conversion in an annealing process, or AR-P was used as an etch mask to generate etch pits in the sapphire. Both of which is believed to increase the hydrophilic and thus underwater superoleophobic character of sapphire. Work still remains with regards to the structuring of sapphire as to whether or not the solid-state conversion procedure provides sapphire, and at which annealing conditions hillocking is removed. It was suggested to optimize the heating

and cooling rate of the annealing procedure to better control the diffusion of aluminium which is believed to cause some cavitation in the structures. A systematic study of the annealing parameters should therefore be conducted.

Two structured sapphire samples of 5 µm width and 15 µm pitch were characterized and compared to flat sapphire using contact angle measurements, one with annealed aluminium converted to sapphire and one witch etch pits. The annealed sample had a contact angle of $37 \pm 3°$ for water in air when structured ($16 \pm 2°$ for flat) and the etched sample had a contact angle of $33 \pm 2°$ (flat = $18 \pm 2°$). Both samples had a higher contact angle than expected from theory for water in air. This tendency is believed to be caused by some contamination layer on the surfaces, as they were not cleaned after structuring. When measuring the contact angle of oil submerged in water the contact angles were $153 \pm 3°$ (flat = $142 \pm 2°$) for the annealed sample and $139 \pm 2°$ (flat = $135 \pm 2°$) for the etched sample. The annealed sample showed a contact angle between the expected Wenzel and the Cassie-Baxter. This is likely due to the increased sourface roughness obtained from microcrystallites on the surface features, or the partial penetration of oil into the water pockets of the Cassie-Baxter state. The etched sample showed contact angles as expected from theory, though it was not possible to determine if it was in the Wenzel or Cassie-Baxter wetting state without measuring the contact angle hysteresis. In general structuring the surfaces did not influence the wetting properties of the surfaces significantly as compared to the flat surface, but it is believed that the oleophobic properties as a function of time when submerged in water are strongly improved.

As for the negative type resist, SU-8 2002, the pillars generated were a first step towards manipulating the surface features on sapphire and thus structure it depending on the application, e.g. superhydrophobicity, icephobicity and/or underwater superoleophobicity. In this work a discussion on the optimization procedure is given, discussing what the surface will look like after over- and underexposure. Characterization of the wetting properties was conducted using contact angle measurements. From this characterization it was shown that the surface features with lowest surface coverage (pitch = 15 µm and size = 5 µm) resulted in the most hydrophobic character, but that it quickly transitioned to a state between the Cassie-Baxter and Wenzel state. For the largest structures (pitch = 25 µm and size = 10 µm) the contact angle was measured to be $92 \pm 2°$, as compared to $88 \pm 2°$ for the flat. The medium sized (pitch = 15 µm and size = 5 µm) had an average contact angle of $99 \pm 2°$ after transitioning from the CB-state, and the smallest (pitch = 7 µm and size = 5 µm) had an average contact angle $115 \pm 5°$, consistent with the expected values for the Cassie-Baxter wetting state. It is further suggested that a systematic study of how pitch and aspect ratio influences the wetting properties should be conducted.

A final suggestion for future work would be a simulation of water on the surface. This could be conducted by molecular dynamics simulations of water molecules, similar to the work of Yong and Zhang (2009).[45] Once the water molecules have been simulated and interacts with the surface, it should be possible to vary both structural parameters such as height and width, in addition to pitch values. As was suggested in this thesis one should also try optimizing the surface features' geometry on the sample.

Appendix A

Optimized Parameters for Microstructuring

The following chapter will summarize the parameters optimized in this thesis. It will not list the optimal parameters for solid-state conversion and wet-etch of sapphire, as these parameters are yet to be optimized.

The sample cleaning should be conducted according to what is detailed in Section 4.2.2.

A.1 AR-P 3540

Spin-coating:

- Spin-speed 1: 600 RPM
- Spin-time 1: 10 seconds
- Spin-speed 2: 4000 RPM
- Spin-time 2: 60 seconds

Note: Important to cover the whole wafer with photoresist before spinning, as AR-P is a resist with relatively high viscosity. Placing the centre of the sample on the rotational axis is also advised to ensure homogeneous deposition.

Tempering:

Conducted on hotplate.

- Temperature: 90°C
- Time: 5 minutes

Note: Important to keep hotplate in fumehood. Using 100°C for 1 minute also works.

Exposure:

Conducted using in-house setup in ISO-5 (details on setup in Section 3.1.1). Exposure time varies with structure size.

- Pitch = 25 µm, size = 10 µm: 28 seconds
- Pitch = 15 µm, size = 5 µm: 31.5 seconds
- Pitch = 7 µm, size = 5 µm: 34.5 seconds

Note: Important to ensure hard contact between mask and sample. Additionally it is important to ensure the mask is levelled with the sample. This could be obtained by placing samples of similar thickness in each corner of the mask.

Development:

Developed in an 1:1 solution of AR 300-40 and DI-H_2O. Stop development by submerging sample in DI-H_2O after developing time is over.

- Time in developer: 60 seconds
- Agitation during development: Yes, preferably with magnetic stirrer and the flow hitting backside of sample.
- Time in stopper: 30 seconds

A.2 SU-8 2002

The SU-8 2002 is originally delivered at a 29% concentration. Here we used 27%. This is obtained using the thinner provided by MicroChem.

Spin-coating:

All sapphire samples were kept at the hotplate for 2 minutes at 95°C before spin-coating.

- Spin-speed 1: 500 RPM
- Spin-time 1: 10 seconds
- Spin-speed 2: 5000 RPM
- Spin-time 2: 60 seconds

Tempering:

Tempering is conducted on a hotplate.

- Temperature: 95°C
- Time: 1 minute

Exposure:

Conducted using MJB4 at the Department of Biomedicince. Details on this instrument in Section 4.2.5.

- Contact mode: Hard contact
- Exposure mode: Flood exposure
- Exposure cycles: 1
- Exposure time:

  Pitch = 25 μm, size = 10 μm: 3.0 seconds

  Pitch = 15 μm, size = 5 μm: 3.0 seconds

  Pitch = 7 μm, size = 5 μm: 2.9 seconds

Post-exposure bake:

- PEB temperature 1: 65°C
- PEB time 1: 1 minute
- PEB temperature 2: 95°C
- PEB time 2: 1 minute

Development:

Developer used for SU-8 2002 was the SU-8 Developer produced by MicroChem. The sample is first immersed in the developer, followed by rinsing using the stopper, isopropanol.

- Developer time: 60 seconds
- Stopper time: 30 seconds

Appendix B

Apparent Layering From Interference Effects

In Section 5.2.1 it seems as though the resist is layered for several of the figures (Figure 5.4, 5.5 and 5.8). As was mentioned, this can be attributed to interference effects between the transmitted and reflected light.

This interference effect occurs when there is a mismatch between the refractive index of the photoresist and the substrate (here Si_3N_4). The incident light wave intensity will decrease from the surface of the resist to the substrate as a result of absorption, in addition to being modulated by the reflected wave. As a result, the solubility, i.e. the part of the resist exposed to light, will vary with depth, z, the distance from resist surface to substrate.[90] To describe the interference effects we can assume there is no absorption in the material, and that the incident light has unit amplitude. The electromagnetic wave in the material can then be described by

$$E_1(z) = E_1 \sin(\omega t - kz + \phi) \tag{B.1}$$

where $E_1 = (1 - r^2)^{1/2}$. Here $r = (n-1)/(n+2)$ is the reflection coefficient at the air-film interface, $k = 2\pi n/\lambda$, and n is the real part of the film dielectric constant, $\bar{n} = kn - ik$.[90] The wave reflected by the substrate (here: Si_3N_4), will have the following amplitude assuming the substrate is a perfect reflector, i.e. $r = 1$:

$$E_2(z) = E_1 \sin[\omega t - k(2d - z) + \phi + \pi] \tag{B.2}$$

where a phase change of π is assumed during reflection.[90] The two waves interfering will be equivalent to adding their amplitudes:

$$E_{12}(z) = 2E_1 \sin[k(d - z)] \cos(\omega t - kd + \phi). \tag{B.3}$$

For plane waves the intensity is proportional to E^2, and thus one can write the intensity for the interfering waves as:[90,91]

$$I_{12}(z) = 4I_1 \sin^2[k(d - z)] \tag{B.4}$$

where the I_1 is the incident intensity. Minima (nodes) are obtained when

$$k(d - z) = \frac{2\pi n}{\lambda}(d - z) = \pi N, \qquad N = 1, 2, \ldots \tag{B.5a}$$

$$n(d - z) = \frac{\lambda N}{2}, \qquad N = 1, 2, \ldots \tag{B.5b}$$

Maxima (antinodes) are obtained when

$$\frac{2\pi n}{\lambda}(d-z) = \pi(N+\frac{1}{2}), \qquad N = 0,1,2,\ldots \tag{B.6a}$$

$$n(d-z) = \frac{\lambda(2N+1)}{4}, \qquad N = 0,1,2,\ldots \tag{B.6b}$$

As the substrate in question is nonideal, i.e. $r < 1$, and the phase change is less than π, there will in reality be a node shift and the appearance of finite light at the minima.[90] Other variables such as depth-dependent dose and absorption will also influence the absolute intensity distribution. Yet Equation (B.4), (B.5) and (B.6) illustrates that there is a depth dependence on the intensity. This will result in varying interaction of light with the photosensitive components of the photoresist, which in turn will influence what the developed result looks like. Brodie and Muray (1992) illustrated the edge profile for a normal 1-µm line in AZ1350 positive photoresist developed for 85 seconds in 1:1 AS developer-water by the basis of the above results (see Figure B.1).[90] It is evident that the edge profile of Figure B.1 resembles the edge profile observed in the Figures 5.4, 5.5 and 5.8, meaning that the resist is in fact not layered, but that these observations originate from interference in combination with the absorption of light through the sample.

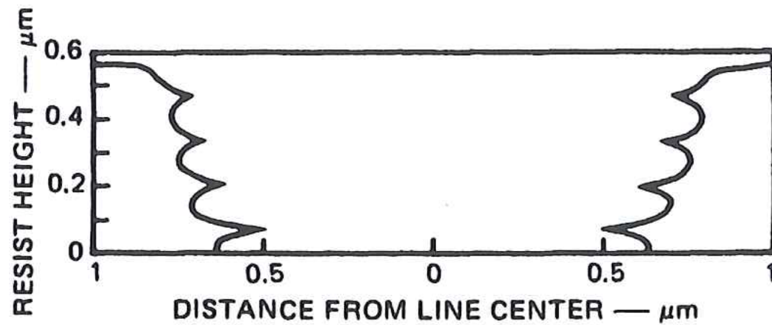

Figure B.1: Edge profile of a positive developed sample. Example is for a normal 1-µm line in AZ1350 photoresist developed for 85 s in 1:1 AS developer-water. Figure from "The Physics of Micro/Nano-Fabrication" by Brodie and Muray.[90]

Bibliography

[1] M. Haruta. “When gold is not noble: Catalysis by nanoparticles”. In: *Chemical Record*, 3 (2) (2003): pp. 75–87.

[2] A. Tuteja et al. “Robust omniphobic surfaces.” In: *Proceedings of the National Academy of Sciences of the United States of America*, 105 (47) (2008): pp. 18200–18205.

[3] J. Chen et al. “Superhydrophobic surfaces cannot reduce ice adhesion”. In: *Applied Physics Letters*, 101 (2012).

[4] Board of Trustees of the Royal Botanic Gardens - Kew. *Nelumbo nucifera (sacred lotus)*. URL: *http://www.kew.org/science-conservation/plants-fungi/nelumbo-nucifera-sacred-lotus* (visited on 05/06/2016).

[5] B. Bhushan, Y. C. Jung, and M. Nosonovsky. *Lotus Effect: Surfaces with Roughness-Induced Superhydrophobicity, Self-Cleaning, and Low Adhesion.* Ed. by Bharat Bhushan. 3rd ed. 2010, pp. 1437–1524.

[6] D. L. Gautier et al. “Gas in the Arctic”. In: *Science*, 324 (2009): pp. 1175–1179.

[7] J. Heidemann, J. Wills, and A. Syed. “Research challenges and applications for underwater sensor networking”. In: *IEEE Wireless Communications and Networking Conference, 2006. WCNC 2006.* 1 (2006): pp. 228–235. URL: *http://ieeexplore.ieee.org/lpdocs/epic03/wrapper.htm?arnumber=1683469*.

[8] P. Frohboese and A. Anders. “Effects of Icing on Wind Turbine Fatigue Loads”. In: *Journal of Physics: Conference Series*, 75 (2007): pp. 1–13.

[9] N. Dalili, a. Edrisy, and R. Carriveau. “A review of surface engineering issues critical to wind turbine performance”. In: *Renewable and Sustainable Energy Reviews*, 13 (2009): pp. 428–438.

[10] B. P. Jelle. “The challenge of removing snow downfall on photovoltaic solar cell roofs in order to maximize solar energy efficiency—Research opportunities for the future”. In: *Energy and Buildings*, 67 (7465) (2013): pp. 334–351. URL: *http://linkinghub.elsevier.com/retrieve/pii/S0378778813005070*.

[11] M. M. Aman et al. “A review of Safety, Health and Environmental (SHE) issues of solar energy system”. In: *Renewable and Sustainable Energy Reviews*, 41 (2015): pp. 1190–1204. URL: *http://linkinghub.elsevier.com/retrieve/pii/S1364032114007734*.

[12] L. Tianyou and L. Juanjuan. “Analysis of icing accident in South China power grids in 2008 and it’s countermeasures”. In: *IET Conference Publications*, (0119) (2009). URL: *http://ieeexplore.ieee.org/stamp/stamp.jsp?tp=&arnumber=5255506*.

[13] L. Jiazheng et al. "Analysis of Hunan Power Grid Ice Disaster Accident in 2008". In: *The International Conference on Electrical Engineering 2009* (2009).

[14] R. Radermacher and K. Kim. "Domestic refrigerators : recent developments". In: *International Journal of Refrigeration*, 19 (1) (1996): pp. 61–69.

[15] L. Huang et al. "Experimental study on frost release on fin-and-tube heat exchangers by use of a novel anti-frosting paint". In: *Experimental Thermal and Fluid Science*, 33 (7) (2009): pp. 1049–1054. URL: *http://linkinghub.elsevier.com/retrieve/pii/S089417770900082X*.

[16] International Maritime Organization. *Anti-fouling systems*. 2016. URL: *http://www.imo.org/en/OurWork/Environment/Anti-foulingSystems/Pages/Default.aspx* (visited on 05/10/2016).

[17] L. Zhang et al. "A self-cleaning underwater superoleophobic mesh for oil-water separation." In: *Scientific Reports*, 3 (2013): p. 2326. URL: *http://www.scopus.com/inward/record.url?eid=2-s2.0-84881353073&partnerID=tZOtx3y1*.

[18] D. W. Kolpin et al. "Pharmaceuticals, Hormones, and Other Organic Wastewater Contaminants in U.S. Streams, 1999-2000: A National Reconnaissance". In: *Environmental Science & Technology*, 36 (6) (2002): pp. 1202–1211.

[19] A. Soares et al. "Nonylphenol in the environment: A critical review on occurrence, fate, toxicity and treatment in wastewaters". In: *Environment International*, 34 (7) (2008): pp. 1033–1049.

[20] J. Lv et al. "Bio-Inspired Strategies for Anti-Icing". In: *ACS Nano*, 8 (4) (2014): pp. 3152–3169.

[21] U. Björnstig, J. Björnstig, and A. Dahlgren. "Slipping on ice and snow - Elderly women and young men are typical victims". In: *Accident Analysis and Prevention*, 29 (2) (1997): pp. 211–215.

[22] W. S. Pike. "Extreme warm frontal icing on 25 February 1994 causes an aircraft accident near Uttoxeter". In: *Meteorological Applications*, 2 (3) (1995): pp. 273–279. URL: *http://dx.doi.org/10.1002/met.5060020310*.

[23] J. Marwitz et al. "Meteorological Conditions Associated with the ATR72 Aircraft Accident near Roselawn, Indiana, on 31 October 1994". In: *Bulletin of the American Meterological Society*, 78 (1) (1997): pp. 41–52.

[24] F. R. Mosher et al. "Analysis of Causes of Icing Conditions which Contributed to the Crash of Continental Flight 3407". In: 2010.

[25] A. Lafuma and D. Quéré. "Superhydrophobic states". In: *Nature Materials*, 2 (7) (2003): pp. 457–460. URL: *http://www.ncbi.nlm.nih.gov/pubmed/12819775*.

[26] M. Farzaneh, C. Volat, and A. Leblond. "Anti-icing and de-icing techniques for Overhead Lines". In: *Springer: Netherlands* (2008): pp. 229–268.

[27] J. Chen et al. "Robust prototypical anti-icing coatings with a self-lubricating liquid water layer between ice and substrate". In: *ACS Applied Materials and Interfaces*, 5 (10) (2013): pp. 4026–4030.

[28] A. J. Meuler et al. "Relationships between water wettability and ice adhesion". In: *ACS Applied Materials and Interfaces*, 2 (11) (2010): pp. 3100–3110. URL: *http://www.ncbi.nlm.nih.gov/pubmed/20949900*.

[29] X. Gao and L. Jiang. "Biophysics: water-repellent legs of water striders." In: *Nature*, 432 (November) (2004): p. 36.

[30] J. C. Bird et al. "Reducing the contact time of a bouncing drop". In: *Nature*, 503 (2013): pp. 385–388. URL: *http://www.nature.com/nature/journal/v503/n7476/pdf/nature12740.pdf*.

[31] A. Pringle et al. "The captured launch of a ballistospore." In: *Mycologia*, 97 (4) (2005): pp. 866–871.

[32] Q. Zhang et al. "Anti-icing surfaces based on enhanced self-propelled jumping of condensed water microdroplets." In: *Chemical Communications*, 49 (40) (2013): pp. 4516–4518. URL: *http://www.ncbi.nlm.nih.gov/pubmed/23575638*.

[33] T.-S. Wong et al. "Bioinspired self-repairing slippery surfaces with pressure-stable omniphobicity". In: *Nature*, 477 (7365) (2011): pp. 443–447. URL: *http://www.nature.com/doifinder/10.1038/nature10447*.

[34] K. Rykaczewski et al. "Mechanism of frost formation on lubricant-impregnated surfaces." In: *Langmuir*, 29 (17) (2013): pp. 5230–5238. URL: *http://www.ncbi.nlm.nih.gov/pubmed/23565857*.

[35] N. Vogel et al. "Transparency and damage tolerance of patternable omniphobic lubricated surfaces based on inverse colloidal monolayers". In: *Nature Communications*, 4 (2013).

[36] T. Ikeda-Fukazawa and K. Kawamura. "Molecular-dynamics studies of surface of ice Ih". In: *The Journal of Chemical Physics*, 120 (3) (2003): p. 1395. URL: *http://scitation.aip.org/content/aip/journal/jcp/120/3/10.1063/1.1634250*.

[37] A. P. Esser-Kahn, V. Trang, and M. B. Francis. "Incorporation of antifreeze proteins into polymer coatings using site-selective bioconjugation." In: *Journal of the American Chemical Society*, 132 (38) (2010): pp. 13264–13269. URL: *http://www.ncbi.nlm.nih.gov/pubmed/20825180*.

[38] M. Nosonovsky and B. Bhushan. "Multiscale effects and capillary interactions in functional biomimetic surfaces for energy conversion and green engineering". In: *Philosophical Transactions of the Royal Society A*, 367 (2009): pp. 1511–1539.

[39] Y. C. Jung and B. Bhushan. "Wetting behavior of water and oil droplets in three-phase interfaces for hydrophobicity/philicity and oleophobicity/philicity". In: *Langmuir*, 25 (24) (2009): pp. 14165–14173.

[40] C. Buzea, I. I. Pacheco, and K. Robbie. "Nanomaterials and nanoparticles: sources and toxicity". In: *Biointerphases*, 2 (2007) (2007): MR17–R71. arXiv: *0801.3280*.

[41] J. R. Lien and G. Løvhøiden. *Generell fysikk for universiteter og høgskoler: Bind 1 Mekanikk*. 3rd. Universitetsforlaget AS, 2010, pp. 251–256. ISBN: 978-82-15-00005-3.

[42] L. E. Helseth. *PHYS111 - Mechanics 1 Compendium*. Department of Physics and Technology, University of Bergen, 2014, pp. 174–182.

[43] T. S. Chow. "Wetting of Rough Surfaces". In: *Journal of Physics: Condensed Matter*, 10 (27) (1998): pp. L445–L451.

[44] J. N. Israelachvili. *Intermolecular and Surface Forces*. 3rd ed. Elsevier Inc., 2011, pp. 415–468. ISBN: 978-0-12-391927-4.

[45] X. Yong and L. T. Zhang. "Nanoscale wetting on groove-patterned surfaces". In: *Langmuir*, 25 (9) (2009): pp. 5045–5053.

[46] A. B. D. Cassie and S. Baxter. "Wettability of Porous Surfaces". In: *Transactions of the Faraday Society*, 40 (1944): pp. 546–551.

[47] C Ishino, K Okumura, and D Quéré. "Wetting transitions on rough surfaces". In: *Europhysics Letters*, 68 (3) (2007): pp. 419–425.

[48] S. Herminghaus. "Roughness-induced non-wetting". In: *Europhysics Letters*, 2 (52) (2000): pp. 165–170.

[49] J. Bico, U. Thiele, and D. Quéré. "Wetting of textured surfaces". In: *Colloids and Surfaces A*, 206 (2002): pp. 41–46.

[50] B. Krasovitski and A. Marmur. "Drops down the hill: Theoretical study of limiting contact angles and the hysteresis range on a tilted plate". In: *Langmuir*, 21 (9) (2005): pp. 3881–3885.

[51] M. Nosonovsky and B. Bhushan. *Multiscale Dissipative Mechanisms and Hierarchical Surfaces.Friction, Superhydrophobicity, and Biomimetics*. 2008, pp. 64–178. ISBN: 9783540784241.

[52] M. Jin et al. "Underwater superoleophilicity to superoleophobicity: role of trapped air". In: *Chemical Communications* (2012): pp. 11745–11747.

[53] L. Gao and T. J. McCarthy. "Teflon is hydrophilic. Comments on definitions of hydrophobic, shear versus tensile hydrophobicity, and wettability characterization". In: *Langmuir*, 24 (17) (2008): pp. 9183–9188.

[54] L. Gao and T. J. McCarthy. "Wetting 101". In: *Langmuir*, 25 (24) (2009): pp. 14105–14115.

[55] University of Bergen. *Wiki for UiB's NanoStructures Laboratory*. 2015. URL: *https://wiki.uib.no/nanolab/index.php/Main_Page* (visited on 04/16/2016).

[56] Technical Committee ISO/TC 209. *ISO 14644-1:1999*. 1999.

[57] AllResist GmbH. "Positive Photoresists AR-P 3500 / 3500 T". In: *Product Information* (2014): pp. 22–25.

[58] AllResist GmbH. *FAQs Photoresists*. 2015. URL: *http://www.allresist.com/category/faqs-photoresists/* (visited on 11/11/2015).

[59] A. del Campo and C. Greiner. "SU-8: a photoresist for high-aspect-ratio and 3D submicron lithography". In: *Journal of Micromechanics and Microengineering*, 17 (6) (2007): R81–R95.

[60] H. Lorenz et al. "SU-8: a low-cost negative resist for MEMS". In: *Journal of Micromechanics and Microengineering*, 7 (1997): pp. 121–124.

[61] Microchem. "Product Information: SU-8 2000 Permanent Epoxy Negative Photoresist". In: *Processing Guidelines* (2015). URL: *www.microchem.com*.

[62] T. M. Bolstad. “Fabrication of Nanostructured Fresnel Zone Plates for Atom Optics Using Electron Beam Lithography”. M.Sc. Thesis. University of Bergen, 2012.

[63] BOC Edwards. *Systems Documentation for FC- and BJD-2000 Deposition Systems*. 2004.

[64] Plasma Etch Inc. *What is Reactive Ion Etching?* 2016. URL: *http://www.plasmaetch.com/reactive-ion-etching-systems-rie.php* (visited on 04/09/2016).

[65] M. M. Greve. “Nanostructures for the manipulation of electromagnetic waves”. PhD Thesis. University of Bergen, 2013, pp. 17–28.

[66] D. B. Hall, P. Underhill, and J. M. Torkelson. “Spin Coating of Thin and Ultrathin Polymer Films”. In: *Polymer Engineering and Science*, 38 (12) (1998): pp. 2039–2045.

[67] Chemat Technology Inc. *Spin Coater KW-4A Owner’s Manual*. 2010.

[68] University of Bergen. *Nano Lab*. 2013. URL: *http://www.uib.no/en/rg/cellnet/65946/nano-lab* (visited on 12/02/2015).

[69] Süss MicroTec AG. “MJB4 Manual Mask Aligner”. In: *Product Information* (2013).

[70] E. R. Dobrovinskaya, L. A. Lytvynov, and V. Pishchik. *Sapphire: Material, Manufacturing, Applications*. 2009, pp. 55–176. ISBN: 978-0-387-85695-7. URL: *http://link.springer.com/10.1007/978-0-387-85695-7_1*.

[71] N. Akhtar et al. “Underwater Superoleophobic Sapphire (0001) Surfaces”. In: *Journal of Physical Chemistry C*, 119 (27) (2015): pp. 15333–15338.

[72] D. Zhang, Y. Wang, and Y. Gan. “Characterization of critically cleaned sapphire single-crystal substrates by atomic force microscopy, XPS and contact angle measurements”. In: *Applied Surface Science*, 274 (2013): pp. 405–417. URL: *http://dx.doi.org/10.1016/j.apsusc.2012.12.143*.

[73] W. W. Flack et al. “A mathematical model for spin coating of polymer resists”. In: *Journal of Applied Physics*, 56 (4) (1984): pp. 1199–1206.

[74] Brewer Science. *Spin Coating Theory*. 2016. URL: *http://www.brewerscience.com/research/processing-theory/spin-coating-theory#process-theory* (visited on 03/30/2016).

[75] Brewer Science. *Overcoming spin-coating challenges for square substrates*. 2011. URL: *http://info.brewerscience.com/Blog/bid/79975/Overcoming-spin-coating-challenges-for-square-substrates* (visited on 03/31/2016).

[76] H. Park, H. M. Chan, and R. P. Vinci. “Patterning of sapphire substrates via a solid state conversion process”. In: *Journal of Materials Research*, 20 (2) (2004): pp. 417–423. URL: *http://www.lehigh.edu/matsci/faculty/chan/docs/Park-Nanpatterning-JMaterRes-2005.pdf*.

[77] J. Biser. “Fabrication of Nanodot Decorated Sapphire Substrates for Abbreviated Growth Mode Deposition of Gallium Nitride”. PhD Thesis. Lehigh University, 2013.

[78] D. S. Wuu et al. “Fabrication of Pyramidal Patterned Sapphire Substrates for High-Efficiency InGaN-Based Light Emitting Diodes”. In: *Journal of The Electrochemical Society*, 153 (8) (2006): G765–G770.

[79] S. X. Jiang et al. “Study on the morphology and shape control of volcano-shaped patterned sapphire substrates fabricated by imprinting and wet etching”. In: *CrystEngComm*, 17 (16) (2015): pp. 3070–3075. URL: *http://xlink.rsc.org/?DOI=C4CE02452D*.

[80] N. Aota et al. “Fabrication Mechanism for Patterned Sapphire Substrates by Wet Etching”. In: *ECS Journal of Solid State Science and Technology*, 3 (5) (2014): N69–N74. URL: *http://jss.ecsdl.org/cgi/doi/10.1149/2.005405jss*.

[81] R. Martinez-Duarte and M. J. Madou. “SU-8 Photolithography and Its Impact on Microfluidics”. In: *Microfluidics and Nanofluidics Handbook*, (2006) (2011): pp. 231–268. URL: *http://dx.doi.org/10.1201/b11188-11*.

[82] C.-H. Lin et al. “A new fabrication process for ultra-thick microfluidic microstructures utilizing SU-8 photoresist”. In: *Journal of Micromechanics and Microengineering*, 12 (5) (2002): pp. 590–597.

[83] J. Zhang et al. “Polymerization optimization of SU-8 photoresist and its applications in microfluidic systems and MEMS”. In: *Journal of Micromechanics and Microengineering*, 11 (1) (2000): pp. 20–26.

[84] A. Utz et al. “Degradation and relaxation effects of Ni patterned anodes in H2–H2O atmosphere”. In: *Journal of the Electrochemical Society*, 157 (6) (2010): B920–B930.

[85] T. Reisinger and B. Holst. “Neutral atom and molecule focusing using a Fresnel zone plate”. In: *Journal of Vacuum Science & Technology B*, 26 (6) (2008): pp. 2374–2379.

[86] D. Brandon and W. D. Kaplan. *Microstructural Characterization of Materials*. 2nd. John Wiley & Sons, Ltd, 2008. ISBN: 978-0-470-02785-1.

[87] J. I. Goldstein et al. *Scanning Electron Microscopy and X-Ray Microanalysis*. 3rd ed. Springer Science + Business Media, LLC, 2003, pp. 132–133. ISBN: 978-0-306-47292-3.

[88] Y. Cheng et al. “Wall profile of thick photoresist generated via contact printing”. In: *Journal of Microelectromechanical Systems*, 8 (1) (1999): pp. 18–26.

[89] A. Rai et al. “Understanding the mechanism of aluminium nanoparticle oxidation”. In: *Combustion Theory and Modelling*, 10 (5) (2006): pp. 843–859.

[90] I. Brodie and J. J. Muray. *The Physics of Micro/Nano-Fabrication*. New York and London: Plenum Press, 1992, pp. 464–473. ISBN: 0-306-44146-2.

[91] D. J. Griffiths. *Introduction to Electrodynamics*. 4th. Pearson Education Limited, 2014, pp. 406–410. ISBN: 978-1-292-02142-3.